UNIVERSITY OF CALIFORNIA SAN DIEGO

Designing microfluidic devices for the study of cardiovascular diseases

A dissertation submitted in partial satisfaction of the

requirements for the degree

Doctor of Philosophy

in

Engineering Sciences

(Mechanical Engineering)

by

Antoni Garcia de Herreros

Committee in charge:

Professor Juan Carlos Del Alamo, Co-Chair
Professor Padmini Rangamani, Co-Chair
Professor Velia Fowler
Professor Antonio L. Sanchez
Professor David Saintillan
Professor Yingxiao Wang

2022

The dissertation of Antoni Garcia de Herreros is approved, and it is acceptable in quality and form for publication on microfilm and electronically.

University of California San Diego

2022

EPIGRAPH

El caminant, quan entra en aquest lloc,

comença a caminar-hi poc a poc.

~ Joan Maragall i Gorina

TABLE OF CONTENTS

LIST OF FIGURES

LIST OF TABLES

ACKNOWLEDGEMENTS

There are so many individuals I would like to thank for their key contributions to the success of my Ph.D. that I would probably need a separate document to be minimally fair to them. I am grateful to say that, after all the difficulties and obstacles encountered in this period of my life, it has been such an amazing experience mostly due to the amount of extraordinary people that I have encountered during this ride.

I would first like to mention Professor Juan Carlos del Álamo, who got me into San Diego for the first time to perform my bachelor's thesis. He introduced me into research and have guided me all these years through my Ph.D. with his passion, intelligence, and perseverance. He has made me a better version of myself not just by guiding me when I had doubts but allowing me room to explore new ideas and concepts.

I would like to acknowledge Professor Juan C. Lasheras who unfortunately passed away in February 2021. I will always be grateful for his guidance and advice. What I admired the most about him was his ability to constantly find interesting research topics or collaborations where he could apply his extensive skillset and from where his students could obtain a wider view of research.

I would also like to thank to all my lab mates who I coincided with: Lorenzo, Josh, Shun, Ernesto, Marissa, Ricardo, María, Stephanie, Amy, Cathleen, Adithan, Alex, Stephen, Yi-Ting and Ruedi. I'm thankful for the many things you have taught me as well as for the environment that you have created in the lab. You make coming to work fun and inspiring.

To all my friends who have supported and encouraged me during hard times; Andreu, Uri, Fran, Bru, Naza, Pons, Petit, Lluri, Gil, Gerard and everyone else- thank you for being there, you never failed to put a smile on my face.

Thanks to all the members of my doctoral committee and the rest of Professors in the Biomechanics area for their support, for their suggestions and for their time. They all were always a big inspiration to me and academic figures to look up to.

I would like to thank the EMT Snail group at IMIM Barcelona for allowing me to conduct my research there when I got stuck in Spain during the pandemic of Covid 19. I would like to thank all the members; Guillem, Marina, Hector, Laura, Bea, Raul and Jepi for their helpful insights and suggestions.

I would like to thank my family. Thanks to my parents, Antonio and Mireia and my sister Marta. Thank you for being an example of sacrifice and hard work for our family. Their lives are an example of love and dedication. I can only aspire to make them proud and become like them in the future.

And finally, I would like to thank Anna for being the best partner one could ask for. Although we had been separated by the distance most of these years, this endeavor has been made possible thanks to her support and ability to emit peace and calm. She knows best when to listen, when to crack a joke, and when it's time to be sincere. Your love is an infinite source of strength and happiness that has undoubtedly helped me through my Ph.D. and for that, my work is dedicated to you.

Chapter 2, in part, has been published in the journal Advanced Science 2022, 2201481. Garcia-Herreros, Antoni; Yeh, Yi-Ting; Peng, Zhangli; del Álamo, Juan C. The dissertation author was the primary author of this paper.

Chapter 3, in part is currently being prepared for publication of the material.; Garcia-Herreros, Antoni; Yeh, Yi-Ting; del Alamo, Juan C. Criado-Hidalgo, Ernesto. The dissertation author was the primary investigator and author of this material.

VITA

2017	Grau Superior en Enginyeria Industrial (B.S.) Universitat Politècnica de Catalunya (Spain)
2018	Master of Science, University of California San Diego
2018-2021	Graduate Student Researcher, University of California San Diego
2021	Teaching Assistant, University of California San Diego
2022	Doctor of Philosophy, University of California San Diego

PUBLICATIONS

Zhu T, Chiacchia S, Kameny RJ, Garcia-Herreros A, Gong W, Raff GW, Boehme JB, Maltepe E, Lasheras JC, Black S, Datar SA, Fineman JR. “Mechanical forces alter endothelin-1 signaling: comparative ovine models of congenital heart disease”. Pulmonary circulation, 10, (2020).

Yeh, Y. T., Skinner, D. E., Criado-Hidalgo, E., Chen, N. S., Garcia-Herreros, A., El-Sakkary, N., Liu, L., Zhang, S., Kandasamy, A., Chien, S., Lasheras, JC., del Álamo, JC., Caffrey, C. R. Biomechanical interactions of Schistosoma mansoni eggs with vascular endothelial cells facilitate egg extravasation. PLoS pathogens, 18(3), (2022).

Garcia-Herreros, A., Yeh, Y. T., Peng, Z., & del Álamo, J. C. Cyclic mechanical stresses alter erythrocyte membrane composition and microstructure and trigger macrophage phagocytosis. Advanced Science, 2201481, (2022)

Garcia-Herreros, A., Yeh, Y.T., del Alamo, JC., Criado-Hidalgo, E. Tunable photoinitiated hydrogel microspheres for cellular force quantification in complex three-dimensional environments. (In preparation)

ABSTRACT OF THE DISSERTATION

Designing microfluidic devices for the study of cardiovascular diseases

by

Antoni Garcia de Herreros

Doctor of Philosophy in Engineering Sciences (Mechanical Engineering)

University of California San Diego, 2022

Professor Juan Carlos Del Alamo, Chair

Professor Padmini Rangamani, Co-Chair

Microfluidic devices are an extremely useful tool to explore *in vitro* the pathophysiology of many different cardiovascular diseases. In this work, we designed two microfabricated platforms, one for the study of RBCs transmigration through the spleen and another one to characterize three dimensional forces exerted by cells.

Red blood cells (RBCs) are cleared from the circulation by macrophages when they become damaged or display aging signals. This process occurs mainly in the spleen, where blood flows through submicrometric constrictions called inter-endothelial slits (IES), subjecting RBCs

to large-amplitude deformations. In this work, RBCs are circulated through microfluidic devices containing microchannels that replicate the IES. The cyclic mechanical stresses experienced by the cells affect their biophysical properties and molecular composition, accelerating cell aging. Specifically, RBCs quickly transition to a more spherical, less deformable phenotype that hinders microchannel passage, causing hemolysis. This transition is associated with the release of membrane vesicles, which self-extinguishes as the spacing between membrane-cytoskeleton linkers becomes tighter. Proteomics analysis of the mechanically aged RBCs reveals significant losses of essential proteins involved in antioxidant protection, gas transport, and cell metabolism. Finally, it is shown that these changes make mechanically-aged RBCs more susceptible to macrophage phagocytosis. These results provide a comprehensive model explaining how physical stress induces RBC clearance in the spleen. The data also characterize new biomarkers of early "hemodamage" and inflammation preceding hemolysis in RBCs subjected to mechanical stress.

Force exertion is an integral part of cellular phenotype regulating important cell functions and fate. In order to quantify mechanical forces at the cellular scale, traction force microscopy has traditionally been considered a standard for the quantification of forces at the cell-substrate interface. However, quantification of compressive and shear stresses in three dimensions have been elusive due to the lack of experimental and computational techniques appropriate for this sizable challenge. This dissertation presents a novel methodology to produce photo-initiated elastic round microgels that can be functionalized and embedded in three dimensional tissues for force quantification.

Chapter 1. Introduction

Human vasculature is extremely complex, ranging from big arteries like the aorta to capillaries with just a few microns in diameter. Blood vessels are composed of a single layer of endothelial cells (ECs) who mediate nutrient exchange, are the contact site for circulating immune cells during inflammation and respond to different factors to maintain blood homeostasis[1,2]. ECs in arteries and arterioles are surrounded by vascular smooth muscle cells which act both as structural support and also serve as a pressure regulator through contraction and relaxation[3].

The overall function of the cardiovascular system is to transport nutrients and recover cell waste throughout the body. Blood is an extremely complex fluid made of a large variety of components that carry independent functions. A few examples of blood components are small proteins and hormones secreted by the endocrine system and circulated to distant tissues and organs, immune cells that target pathogens and can extravasate through the vascular endothelium to carry out immune reactions at inflammatory sites, and platelets that contribute to the formation of blood cloths preventing an excess of blood loss during lesions. However, the most important blood function is oxygen delivery. Even though a small percentage of oxygen can be transported by direct diffusion into blood in the alveolus, the vast majority is combined with hemoglobin (Hb) inside the red blood cells (RBCs) [4].

RBCs are the most abundant cell type in blood, making almost 45% of its volume. Human RBCs are anucleated and have a discoidal shape with a diameter of 8 μm and a thickness that varies from 1 μm to 2.2 μm in the widest region [5,6] . RBCs have evolved over time to maximize Hb capacity and in mammals these have translated to the absence of nuclei [7]. During erythropoiesis, highly deformable RBCs are differentiated from erythroblasts in the bone marrow

and released into circulation, although a minor proportion of undifferentiated cells, called reticulocytes, that still contain RNA traces, are also released. The process of RBCs egress from the bone marrow into the circulation is still not very well understood, although it has been seen that RBCs mush flow through small pores (0.2-0.4 μm) in the hematopoietic space [8]. After approximately 120 days of circulating through the vasculature, exposed to large deformation in the capillaries and numerous oxygenation/deoxygenation processes, RBCs are removed by macrophages in the spleen and liver[9].

There are a lot of diseases that affect the cardiovascular system: atherosclerosis, hypertension, diabetes and arrythmias are some of the most widespread health concerns in our society. A few of these cardiovascular diseases (CVDs) directly affect RBCs. In some cases, the oxygen carrying efficiency is impaired like in iron-deficient anemias; in others, cell deformability is strongly flawed like in hereditary spherocytosis or malaria. Despite all the efforts, some of the molecular mechanisms that underlie the biochemical response of cardiovascular cells to mechanical forces are still largely elusive.

Since the early 1990 different studies have been performed to replicate *in vitro* the physiological conditions of the human vasculature to investigate cell-cell interactions, measure exerted forces or study cell dynamics. The introduction of microfabrication techniques, especially related to the fabrication of microfluidic devices revolutionized this area, as they offer a large number of advantages over conventional macroscale studies; an infinite number of different geometries can be easily made to adapt and replicate the desired physiology. On the other hand, the use of smaller sample sizes and reagent volumes reduces the experimental time (preparation, reaction, …) and reagent cost. Due to its reduced dimensions, multiple experiments can be performed simultaneously in the same laboratory, providing high-throughput results.

Microfluidics devices have been used to study many different cardiovascular processes involving RBCs. These studies include, how RBCs cross *in vitro* capillaries when infected by malaria parasites [10,11], mechanical alterations in sickle RBCs [12] or even platforms for the screening and early diagnosis of sickle cell patients [13]. Over time, some of these microplatforms have been improved to allow the study of multiple cell types and their interaction, resembling even more the human physiology [14]. Moreover, microfluidic devices have been used to study different cardiovascular topics besides RBCs, such as the transendothelial migration of leukocytes during inflammatory response [15,16] or to isolate circulating tumor cells from blood [17,18].

Microfabricated platforms are also of remarkable importance when studying forces generated by cells in the cardiovascular system. Mechanical forces are critical regulators of cell adhesion, signaling and function, and are essential drivers in mechanotransduction, where mechanical cues are converted into biochemical signals by activation of intracellular cascades [19]. Different approaches have been made to measure the forces applied by cells in the vascular system. Planar, two-dimensional, elastic gels with fiduciary markers have been used to measure the forces exerted by leukocytes and endothelial cells during diapedesis [20]. A similar way of measuring mechanical cues produced by cells have been accomplished using micropillar-based devices. Cells are cultured on top of an array of coated micropillars that when deflected provide a measure of the intracellular forces [21,22]. However, there are limited platforms to study three dimensional forces in different cellular environments. Most of these platforms are based on the study of the deformations of biocompatible polymers by cells. In some cases the cells are embedded in a 3D gel [23]; however, in other cases, spheric hydrogels are placed in between the tissue [24-26].

The focus of this work has been to design and use microfabricated platforms to study, *in vitro*, different cardiovascular problems. The first chapter will cover the process of the fabrication

of a microfluidic device that replicates the inter-endothelial slits in the spleen and was used to study RBCs dynamics and the effect of successive passage in cell aging. The second chapter describes and innovative method using a flow focusing microfluidic device to fabricate spheric elastic hydrogels to measure three dimensional forces exerted by cells.

Chapter 2. Cyclic mechanical stresses alter erythrocyte membrane composition and microstructure and trigger macrophage phagocytosis

2.1 Introduction

Blood flow must be maintained continuously to deliver oxygen from the respiratory system to the rest of tissues in the human body in a steady manner. An interrupted blood flow and oxygen supply may cause tissues inside the human body to be damaged and malfunction. This important function is performed by RBCs which carry large amounts of Hb, a protein capable of binding oxygen. Hemoglobin is an iron containing protein with a quaternary structure characteristic of many multi-subunit globular proteins that allows it to become saturated with oxygen molecules (oxyhemoglobin). Oxyhemoglobin is formed in the transition of RBCs through alveoli during physiological respiration when oxygen binds to the heme group.

During all their lifetime, these cells must deform multiple times through small capillaries in the systemic and pulmonary circulation. The microcirculation is responsible for 80% of the pressure drop between the aorta and the vena cava [27], therefore large mechanical loads are exerted on RBCs during this stage. However, the most severe deformation that RBCs must overcome during a body cycle occurs in the spleen, where cells must squeeze through gaps in between endothelial cell fibers called inter endothelial slits (IES) [28,29] . This process is of

extreme relevance, as certain conditions such as iron deficiency anemias, hemolytic diseases or even malaria impair the ability of RBCs to deform adequately [30,31]. Hence, large amounts of RBCs are damaged, retained or even removed in the spleen, generating a deficiency in oxygen transport from the lungs to the rest of organs, causing endless life threatening symptoms and diseases. Diseases affecting RBCs deformability can also result in splenomegaly or enlargement of the spleen, which is usually treated by splenectomy although this treatment presents a fair share of side effects[32]. Despite all efforts, spleen physiology is still poorly understood and remains of vital importance for doctors and physicians.

The spleen along with the liver oversee the removing of old and diseased RBCs from the circulation. Blood flow coming into the spleen from the splenic artery the spleen is differentiated in two branches[28]. The vast majority of blood, around 90%, bypasses the organ and goes directly into the venules. However, the remaining 10% goes through the open circulation reaching the red pulp of the spleen (Figure 2.1). This region comprises 70–80% of splenic volume and is rich in immune cells such as T cells, lymphocytes and resident macrophages[33]. In the red pulp the majority of pathogens, antigens and defective RBCs are removed from the circulation. Finally, in order for RBCs to return into the vasculature, they have to deform in between IES. These narrow constrictions of about 0.5-2μm in with, ~8 times smaller than RBCs [28,34], are a challenge that only young and deformable cells can overcome, whereas old or diseased cells are stuck and eventually removed by macrophages.

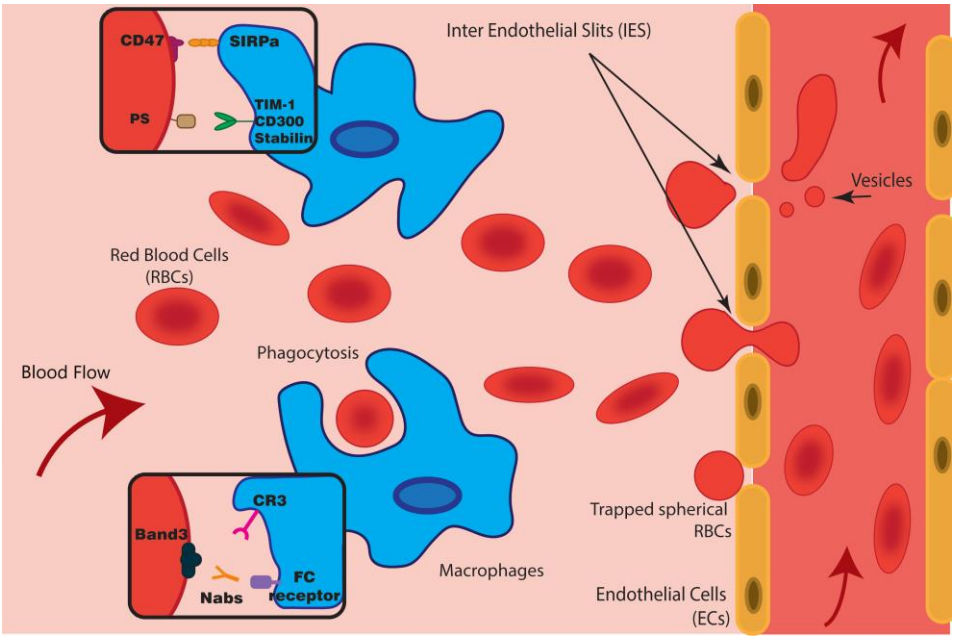

Figure 2.1: Scheme representing a section of the spleen's red pulp. Old or damaged Red Blood Cells (RBCs) are recognized and phagocytized by tissue resident macrophages via a ligand receptor interaction that is still unknown[9,35]. Deformable RBCs are able to squeeze through inter-endothelial slits (IES) and return into the circulation. The transition of RBCs through IES has been hypothesized before to cause the release of membrane vesicles [36].

Even though RBC aging is of crucial importance for hematologic disorders and blood stored for transfusion is still a matter of investigation. As RBCs age, their shape transitions from biconcave-discoidal to serrated or spherical, and their intracellular density increases[37,38]. These changes, often attributed to membrane loss, are associated with decreased deformability, leading to failure to squeeze through the IES [39]. Additionally, aged RBCs exhibit significant biochemical changes affecting cell volume, deformability, and metabolic activity, such as ATP depletion [40] and increased cytoskeleton oxidation [41]. In particular, oxidation promotes the denaturing of hemoglobin and the aggregation of band3 [42-44] a membrane protein required for CO2 transport that also regulates RBC stiffness by anchoring the lipid bilayer to the cytoskeleton.

How macrophages identify and remove RBCs from the circulation is still poorly understood. This specific macrophage attack is associated with the presence of distinctive age-related signals in the RBC membrane. Some studies have reported an increase in

phosphatidylserine (PS) in the outer leaflet of the membrane as RBCs age[45]. PS is a phospholipid usually located in the inner leaflet of the membrane; however, when exposed in the outer leaflet, it acts as a phagocytosis signal [46]. Additionally, the expression of CD47, a membrane protein that inhibits macrophage attacks, declines as RBCs age [47]. Finally, band3 clustering promoted by age-induced oxidation facilitates autoantibody binding and could mediate RBC recognition by macrophages[35].

Increased intracellular density is the primary experimental marker of RBC aging because it correlates with other hallmarks of RBC functional decline. Recent data suggest that RBCs exposed to cyclic stretch exhibit significant changes in shape and mechanical properties (i.e., mechanical fatigue) [48,49]. This evidence led us to hypothesize that RBC deformations cause biophysical and biochemical changes equivalent to aging, which can be accelerated significantly *in vitro*. The main goals of the present study were to test these hypotheses and to investigate the underlying mechanisms for mechanically induced RBC aging.

In vivo experiments in the spleen are rarely conducted because of two main reasons, first and foremost, the high invasiveness of the studies coupled with remarkably structural differences between different species. Computational simulations have been successfully used in the past to study this process [36,50], however, there is still a lack of experimental data to validate the different models. Overall, there is a need of robust *in vitro* tools that are easy to use or manufacture and comprise the main functionalities of the spleen. To this end, we fabricated PDMS-based microfluidic devices to model the passage of RBCs through IES in the spleen. We analyzed the biophysical and biochemical changes undergone by RBCs as a function of the number of repetitive passages through these microchannels, finding significant metabolic, proteomic, and biomechanical alterations. Specifically, we demonstrated that RBCs undergo cellular vesiculation

and cell rounding accompanied by key biological hallmarks of RBC aging like decreased intracellular ATP and enhanced oxidation, all associated with a higher susceptibility to macrophagic attack. In addition to providing insights into the biomechanical underpinnings of RBC aging, this work offers a proof of principle of using microfluidic devices to systematically and reproducibly accelerate RBC aging *in vitro*.

2.2 Materials and Methods

2.2.1 Microfluidic device fabrication and characterization.

Microfabrication

A series of polydimethylsiloxane (PDMS) microfluidic devices with multiple constrictions of customizable geometry were designed and manufactured in the San Diego Nanotechnology Facility of UC San Diego. A two-step photolithography process combining both positive and negative photoresist was used to fabricate the mold of the device, resulting in a two-layer device. The thicker layer (25μm), used for the inlet and outlet regions, was made with negative photoresist to allow for minimized flow resistance and RBC deformation outside of the constrictions. The central part of the device containing the constrictions required higher resolution which was obtained leveraging the thinner layer (5 μm) of positive photoresist.

The process started by cleaning a 4-inch silicon wafer (University Wafer, MA, USA) in a sonic bath of acetone for 5 min; then it was rinsed in methanol, isopropanol and finally water. Subsequently, the wafer was dehydrated at 180° C for 10 min and its surface activated using a plasma treatment (PVA TePla PS100, Germany) for 5 min. A coat of MCC Primer 80/20 (Microchemicals, MA, USA) was applied to improve the attachment of the photoresist to the

wafer. After a short (2 min) bake at 110° C, the first layer of SU8 2050 negative photoresist (Microchemicals) was applied by spin coating at 3000 rpm for 30 sec. After 6 min of soft bake at 95°C, the inlet and outlet regions of the device were exposed using a MLA150 (Heidelberg Instruments Mikrotechnik GmbH, Germany) under a laser with 375 nm wavelength and a dose of 3000 mJ/cm^2. The post exposure bake was carried at 95° C for 5 min and then the wafer was developed using SU8 developer (Microchemicals). The second part of the process started by applying again a coat of MCC Primer and then spin coating AZ12XT-20PL-05 (Microchemicals) for 30 sec at 800 rpm. After soft baking the sample for 2 min at 110° C, the whole device, including inlet/outlet and central region was exposed using a dose of 200 mJ/cm^2. Afterwards, the post exposure bake was carried on for 1 min at 90° C and the wafer was developed using AZ300 MIF (Microchemicals). The heights of the channel were verified using a Dektak 150 surface profilometer (Veeco Instruments Inc. Plainview, NY, USA) and the wafer was passivated with tridecafluoro-1,1,2,2-tetra-hydrooctyl-1–trichlorosilane e (Gelest, Morrisville, PA, USA) for 15 min inside a vacuum chamber to prevent PDMS adhesion to the wafer.

PDMS replicas of the device were made by casting a previously degassed mixture of the PDMS oligomer and crosslinking agent (Sylgard®184, Dow Corning Inc, Midland, MI, USA) in a 10:1 (w/w) proportion on the passivated silicon wafer. The sample was then cured at 65° C overnight. The next day the master was peeled off from the wafer, cut into several single devices and the inlet and outlet holes were punched (2.5 mm) with a biopsy puncher (Miltex, Integra Lifesciences, Plainsboro Township, NJ, USA). Finally, we activated the surface of both coverslip (Corning, 24x60 mm and thickness 1.5 mm) and PDMS chip under a UV ozone lamp (Model 30, Jelight Co., CA, USA) for 4 min with an oxygen inflow of 0.2 l/min and bonded them together at 65° C for a minimum of 4 h before they were ready to be used.

Flow Characterization

A solution of PBS containing fluorescent nanotracers (0.2 μm in diameter) was flown through the microfluidic device using the same flow rate as in the experiments. High frame rate fluorescent images were acquired using a DMI 6000B inverted phase contrast microscope (Leica Camera, Wetzlar, Germany) equipped with a camera (Zyla3-Tap Enclosed C-mount 16 bit, Andor Technology, Belfast, UK). Using an in-house ensemble μ-PIV method, the velocity profile at the constriction entry was obtained. This data was used afterward as input for a COMSOL simulation (COMSOL Multiphysics, Stockholm, Sweden) from where the pressure drop and the maximum shear stress were extracted.

2.2.2 Cell culture

Red Blood Cell isolation

Human blood from healthy donors was obtained in Heparin treated BD Vacutainer tubes (Becton, Dickinson and Company, Franklin Lakes, NJ, USA) from the San Diego Blood Bank. Upon reception, Red Blood Cells (RBCs) were isolated using a density gradient technique[51]. First, a 15 ml centrifuge tube (Falcon tube, Thermo Fisher Scientific, Waltham, MA, USA) was filled with 3 ml of Histopaque 1119 (Sigma-Aldrich, St. Louis, MO, USA); then, a 3 ml layer of Histopaque 1077 (Sigma-Aldrich) was added on top and finally 6 ml of whole blood were carefully added to prevent the three layers from mixing. The tube was centrifuged at 700 g for 30 min at room temperature; the top layers containing plasma, mononuclear cells, and granulocytes were discarded and the RBCs were resuspended in PBS (Dulbecco's Phosphate Buffered Saline, Sigma Aldrich). The tube was centrifuged again at 200 g for 10 min at room temperature and the supernatant cells were removed to discard platelets and damaged RBCs. Finally, RBCs were resuspended in AS-3 media[39,52] (dextrose, sodium chloride, adenine, citric acid, sodium citrate

and sodium phosphate were all bought from Thermo Fisher Scientific) in a 5% hematocrit concentration and stored at 4° C until used. All the experiments were conducted within one week of RBC isolation.

Separation of denser and lighter RBCs was performed by a discontinuous gradient of Histopaque. A layer of RBCs was carefully added on top and centrifuged for 15 minutes at 700 g. Layers were aspirated carefully and only bottom(denser) and top (lighter) cells were kept.

RBCs recirculation and crossing time determination.

Flow was driven through the device at a fix flow rate (100µl/h) using a peristaltic pump (IPC, ISMATEC, Switzerland) (Figure 2.1); wider channels (5 µm) were added at both sides of the microchannel array to ensure that microchannel clogging by stuck RBCs did not significantly affect the pressure difference across the array. The maximum number of constrictions crossed by the RBCs was estimated based on the flowrate and the volume of fluid inside the circuit. Therefore, *Nc* represents the maximum number of constrictions that RBCs could have undergone for a period of time. RBCs were recirculated at room temperature.

To measure the crossing time RBCs were washed multiple times in PBS and resuspended at 1% hematocrit in AS-3. The device was left running for 15 min before the image acquisition started to allow the flow to stabilize. The passage of RBCs through misconstructions was imaged in a bright field phase contrast microscope (Leica Camera, Wetzlar, Germany) at a frame rate of 100 fps. The crossing time was manually calculated as the difference between the first and last frame where the RBCs contacted the constriction.

Flow Cytometry

Flow Cytometry was used to measure the vesicles released by RBCs. Briefly, after finishing every experiment, RBC samples were resuspended at 10^6 cells/ml in PBS (Dulbecco's

Phosphate Buffered Saline, Sigma Aldrich, St. Louis, MO, USA) and analyzed using an Accury C6 (BD Biosciences, USA). Blank samples, containing only PBS, were used to set the forward and side scattering thresholds to limit noise measurements, that would reflect in an incorrect reading in the number of vesicles. Manual gating for the RBCs and samples was performed using a user made MATLAB (The Math Works Inc., Natick, MA, USA) code.

Phosphatidylserine exposure on the outer leaflet of RBCs was measured using the Annexin V Alexa Fluor™ kit (V13241, Thermo Fisher Scientific, Waltham, MA, USA). RBCs were resuspended at a concentration of 10^6 cells/ml in the Annexin V binding buffer. Then, 5 µL of Alexa Fluor® 488 annexin V and 1 µL of Propidium Iodide were added into 100 µL of cell suspension and incubated for 30 min. Finally, cells were centrifuged and resuspended in the binding buffer for analysis using the flow cytometer. Negative controls were used to set up the threshold for the detection of positive cells.

To measure the expression levels of CD47 we incubated the cells with anti-CD47 (Clone B6H12, BD Biosciences) and 2% BSA (Thermo Fisher Scientific) for 1 h at room temperature. We then washed thrice in PBS and incubated the cells with the secondary antibody (Goat anti-Mouse IgG Alexa Fluor 488, Thermo Fisher). Shortly after, the samples were analyzed using the flow cytometer. Appropriate negative controls were prepared to differentiate positive cells.

To measure the percentage of opsonized RBCs we first treated cells with 2% BSA for 1 h, washed with PBS multiple times and incubated with plasma from the same blood sample for 1 h. Finally, RBCs were incubated with anti-Human IgG Alexa Fluor 488 (Thermo Fisher) for 2 h, fixed with 4% PFA (ThermoFisher) and analyzed using the flow cytometer. Negative controls were used to establish a fluorescent threshold.

Hemolysis

The content of hemoglobin in the supernatant was used to measure the percentage of RBCs lysis. Hemoglobin concentration was measured analyzing absorbance at 415 nm in a UV-Visible spectrophotometer (Biomate 3s, Thermo Fisher, Waltham, MA, USA). Before starting the different experiments, a sample containing the same concentration of RBCs was used to later calibrate the absolute hemolysis lysing the cells with 1% SDS (Sigma Aldrich, St. Louis, MO, USA). After finishing every experiment RBCs were pelleted down by centrifuging at 1000 rpm for 2 min (5415C, Eppendorf, Germany) and the supernatant absorbance was assessed and normalized using the maximum hemolysis value.

RBC oxidation

RBCs oxidation was assessed by measuring the intracellular content of Methemoglobin (MetHb) as previously described[53]. RBCs obtained from the different samples were washed multiple times with PBS (Dulbecco's Phosphate Buffered Saline, Sigma Aldrich, St. Louis, MO, USA) to remove any extracellular hemoglobin from lysed cells. Then, RBCs were resuspended in PBS at a final concentration of 10^7 cells/ml, lysed with 1% SDS (Sigma Aldrich) and the absorbance at 645 nm was measured using a UV-Visible spectrophotometer (Biomate 3s, Thermo Fisher, Waltham, MA, USA). The solution was then treated with potassium hexacyanoferrate ($K_3[Fe(CN)_6]$, Thermo Fisher) to completely oxidize Hb into MetHb and the absorbance was measured again. Finally, the percentage of MetHb was obtained by normalizing the two measurements at 645 nm.

ATP concentration

The intracellular ATP concentration was measured using the Luciferin technique (ATP Determination Kit; Thermo Fisher, Waltham, MA, USA). Briefly, 10^5 cells were extracted from

each sample and washed with PBS multiple times to remove any cell remaining in the supernatant. The standard reaction solution containing luciferase and luciferin was prepared according to the manufacturer guidelines and introduced in a black with clear bottom 96-well plate (Corning, Corning, NY, USA). To prevent any possible ATP degradation, RBCs samples were lysed with DI water and quickly added to each well. When ATP reacted with the standard solution, light was emitted with a wavelength of 560 nm and captured with a luminometer (Tecan infinite M1000 Pro, Switzerland). A standard reference curve was made from different ATP concentration from an ATP vial provided with the kit. This curve was used to measure the ATP concentration for each sample. Finally, to obtain the intracellular ATP concentration, the average measured concentration was normalized by the total number of cells lysed and the mean volume obtained in previous experiments. ATP measured concentrations were similar to previous studies[54].

Proteomics analysis

Control RBCs and cells transited through 200 constrictions were collected and washed multiple times with PBS (Dulbecco's Phosphate Buffered Saline, Sigma Aldrich, St. Louis, MO, USA). Then, cells were lysed with DI water and centrifuged at 14000 g for 10 min to collect the cell membranes. The pellet was resuspended in DI water and washed multiple times to remove as much hemoglobin as possible. The total protein concentration was measured using a Micro BCA Protein Assay Kit (Thermo Fisher, Waltham, MA, USA) and resuspended at a final concentration of 120 µg/ml for all samples. Samples were submitted to the Biomolecular and Proteomics Mass Spectrometry Facility (BPMSF, S10 OD016234) at UCSD and analyzed using a label free quantification. The Benjamini-Hochberg correction method[55] was used to adjust the p-values. Protein set enrichment analysis was performed using Metascape on the KEGG, Canonical pathways, Gene Ontology, Reactome, and CORUM databases[56].

Phagocytosis assay

Monocytic THP-1 cells were cultured in Roswell Park Memorial Institute medium (RPMI, Thermo Fisher Scientific, Waltham, MA, USA) supplemented with 10% FBS (Millipore, Sigma Aldrich, St. Louis, MO, USA), 100 U/mL penicillin, and 100 µg/mL streptomycin (Sigma Aldrich) and maintained at 37°C in a humidified atmosphere with 5% CO2.

M-1 macrophages were differentiated from THP-1 cells based on[57]. Briefly, $5x10^5$ THP-1 cells/ml were treated with 25 $\boldsymbol{\eta}$g/ml phorbol myristate acetate (PMA, Thermo Fisher Scientific) in RPMI 1640 with 10% FBS. After 72 h, the media was renewed and a rest period of 72 h was performed before cytokine activation. To polarize macrophages into M1 phenotype, cells were treated with 50 $\boldsymbol{\eta}$g/ml of IFNγ (eBiosciences, San Diego, CA, USA) and 200 ng/ml of LPS (eBiosciences) for 72 h. At this point cells were already activated and ready to interact with RBCs.

RBCs from control or cells transited through 60 or 200 constrictions were collected washed three times with PBS (Dulbecco's Phosphate Buffered Saline, Sigma Aldrich) and resuspended at a concentration of 10^6 cells/ml. Following, RBCs were stained with CellTracker Deep Red CMFDA Dye (Invitrogen, Waltham, MA, USA) for 30 min at 37ºC and washed multiples times with PBS (Sigma Aldrich). Finally, RBCs were opsonized with plasma from the same blood samples for 30 min, cocultured with macrophages in RPMI +10% FBS for 48 h and fixed afterwards for imaging using 4% paraformaldehyde (PFA, Thermo Fisher Scientific). Macrophages were considered active if the measure of its fluorescence was above a certain threshold. To measure the mean fluorescence of each macrophage, cells were manually gated and the mean intensity of inner pixels was calculated.

2.2.3 Microscopy and Imaging

Phase contrast microscopy

A Leica DMI 6000B inverted phase contrast microscope (Leica Camera, Wetzlar,Germany) controlled by a dedicated workstation running the open source µ-Manager software (Vale lab, UCSF, USA) was used for image acquisition. The microscope was equipped with a Zyla3-Tap Enclosed C-mount 16 bit camera (Andor Technology, Belfast, UK) and a MercuryShort-Arc Discharge Lamp with Reflector with emission filters to generate excitation light in the common DAPI, FITC, TRITC, and CY5 wavelengths. For bright field experiments, timelapse sequences were acquired with a frequency of 100 Hz under a 63x oil lens with 10 ms exposure time. A Primovert Inverted Microscope (Carl Zeiss AG, Oberkochen, Germany) was used to examine unstained cells in phase contrast under 10x, 20x and 40x objectives.

Stimulated emission depletion (STED) microscopy

RBCs samples were bonded to Nº 1.5 glass coverslips (Thermo Fisher Scientific, Waltham, MA, USA) treated with 100 ηg/ml Poly-L-Lysine (Sigma Aldrich, St. Louis, MO, USA) for 1 h. Cells were fixed using 4% PFA (Thermo Fisher Scientific) for 15 min, washed multiple times in PBS (Dulbecco's Phosphate Buffered Saline, Sigma Aldrich) and permeabilized with 0.1% Triton-X (Sigma-Aldrich) for 10 min. Non-specific antibody binding was prevented by incubating with 2% BSA (Thermo Fisher Scientific) for 2 h. Cells were incubated with the respective primary antibody (rabbit anti human, anti-ANK1 or anti-EPB41, Sigma Aldrich) overnight. Finally, a secondary antibody (goat anti-rabbit IgG, Thermo Fisher Scientific) was added for 1h and samples were fixed using ProLong Diamond (Thermo Fisher Scientific) for at least 24 h. Samples were imaged in the Microscope Core Facility at UCSD (NS047101) using a Leica SP8 confocal with STED and lightning deconvolution (Leica, Wetzlar, Germany). Post

processing of the images and data analysis was performed with an in-house designed MATLAB (The Math Works Inc., Natick, MA, USA) script. Briefly, the autocorrelation of the images was obtained and the distance between the two higher peaks was used to calculate the distance in between protein complexes.

Scanning Electron Microscopy

Scanning Electron Microscopy was used to assess the geometrical dimensions of the constrictions obtained in the device as well as to observe morphological changes in RBCs. Organic samples were first bonded to glass coverslips (Nº 1.5, Thermo Fisher Scientific, Waltham, MA, USA) treated with 100 $\boldsymbol{\eta}$g/ml Poly-L-Lysine (Sigma Aldrich, St. Louis, MO, USA) for 1 h. Then cells were fixed using a fixative buffer composed of 4% Paraformaldehyde (Thermo Fisher Scientific) supplemented with 2.5% of Glutaraldehyde (Sigma Aldrich) in PBS (Dulbecco's Phosphate Buffered Saline, Sigma Aldrich). After overnight fixation at 4 °C, we aspirated and stored the PFA solution and cover the samples with PBS prior to serial dehydration. For dehydration of our samples, we treated them for 15 minutes with different ethanol concentrations in DI water (50%, 60%, 70%, 80%, 90% and 100% in this order). The samples were then dehydrated and ready for drying. To prevent collapse of biological samples due to surface tension, Critical Point Drying 15 (CPD) was performed on all samples using a Tousimis AutoSamdri 815A critical point dryer (Tousimis, Rockville, MD, USA).

After CPD, the sample was ready for sputter coating, a process performed for organic and inorganic samples, on a K575X Iridium Sputter Coater (Emitech, France). Basically the samples were introduced inside the sputtering chamber, vacuum was applied until the pressure reached 100 mbar and the system was run at 85mA for 8 seconds yielding samples coated with a thin layer of iridium and ready for SEM imaging. Imaging was thereafter performed using a Zeiss Sigma 500.

RBC morphological determinations.

To calculate the volume and the surface of RBCs we used a method based on Fluorescence exclusion as previously described[58,59]. Briefly, RBCs were suspended at a concentration of 10^4 cells/ml in the AS-3 media supplemented with 1 mg/ml of FITC-Dextran (Sigma-Aldrich, St. Louis, MO, USA). The solution containing the cells was introduced into one of the microfluidic devices described previously and imaged. Chambers' heights [4.5-5 μm] were rigorously characterized using a profilometer (Dektak 150 Surface Profiler, Veeco Instruments Inc. Plainview, NY, USA). In the fluorescent field, RBCs and PDMS pillars appeared dark whereas the rest of the chamber, where the Dextran was present, resulted in brighter regions. Image analysis was performed using a in house MATLAB (The Math Works Inc., Natick, MA, USA) script. For each image, a calibration using PDMS pillars was used to obtain the relationship between fluorescence intensity and chamber height as described previously[58]. The linear relationship between the height of the object and the intensity is described by: $IB = \alpha \cdot h + IP$, where IB and IP are the background and PDMS pillar fluorescence respectively and h the height of the chamber. To measure single cell volume, a region of interest was automatically defined around each cell where the background was calculated; then α was obtained and finally the heights of the pixels conforming the cell were obtained. The shape of the RBCs was reconstructed from pixel height data assuming equatorial symmetry. Specifically, for each RBC pixel, a pair of points were defined at distance from the symmetry plane in each direction equal to half the pixel height. From the resulting 3D point cloud, an envelope was recomputed by using the smallest curvature radius that completely enclosed the cloud using the MATLAB built in function *alphaShape*. From each cell's envelope, the surface area and the volume were calculated. To verify the algorithm, a cell reconstruction was considered valid if the difference between the volume computed from the

envelope and the volume calculated by integrating the pixel height (i.e., as proposed in [58]) was smaller than a small threshold (10%) Echinocytes were discarded from surface calculation due to the limitations of the equatorial symmetry assumption.

Determination of RBCs 'effective' bending modulus and membrane tension.

To measure the mechanical properties of RBCs we used thermal flickering spectrometry as described in [60]. Using this technique, we captured the contributions from both the lipid bilayer and the cytoskeleton. RBCs were diluted into culture medium at 10^4 cells/ml and seeded into a thin coverslip (Corning, NY, USA). Bright field microscopy with a small region of interest and low exposure time (3ms) was used for high speed (300 fps) image acquisition. Imaging was performed in a controlled environment at 37 °C by using the setup described above. A MATLAB (The Math Works Inc., Natick, MA, USA) code was written to analyze the images and obtain the mechanical properties of the cells. First, the RBC contour at the cell equator was detected for each frame using the method previously described [61]. Then, the power spectrum of mean square mode amplitudes was obtained by applying the Fourier transform and, from these data, the 'effective' bending modulus (κ) and tension (σ) were fitted using the following equation:

$$\langle |h(q_x, y=0)|^2 \rangle = \frac{1}{P}\frac{k_B T}{2\sigma}\left(\frac{1}{q_x} - \frac{1}{\sqrt{\frac{\sigma}{\kappa}+{q_x}^2}}\right),$$

where k_B is the Boltzmann constant, T is the absolute temperature, and P is the mean perimeter of the RBC contour. This equation was derived from the energy of deforming a flat sheet[62] and describes shape fluctuations of the cell's equator in only a limited range of modes. On one hand, smaller modes are excluded because they are affected by the geometry of the surface and an important deviation from the spherical harmonics expression. On the other hand, high modes, with smaller wavelengths, are affected by noise and their fluctuations lie outside the spatial

and temporal resolution of the experiment. For this reason, we use modes 6 to 18 for fitting the equation above.

2.3 Results

2.3.1 Microfluidic devices mimic crossing of splenic inter-endothelial slits by RBCs

We developed a family of microfluidic devices to model the crossing of RBCs through splenic inter-endothelial slits (IES) using a two-step photolithography process (see Materials and Methods and Figure 2.2 a-b). The devices test section contains an array with 100 parallel microchannels of tunable width (Figure 2.2 c). Microchannels with widths < 1 μm were achieved as measured by scanning electron microscopy (Figure 2.2 d). Previously, sub-micron microchannels were only achievable using microfabrication techniques not commonly available in biological laboratories, such as wet etching [63].

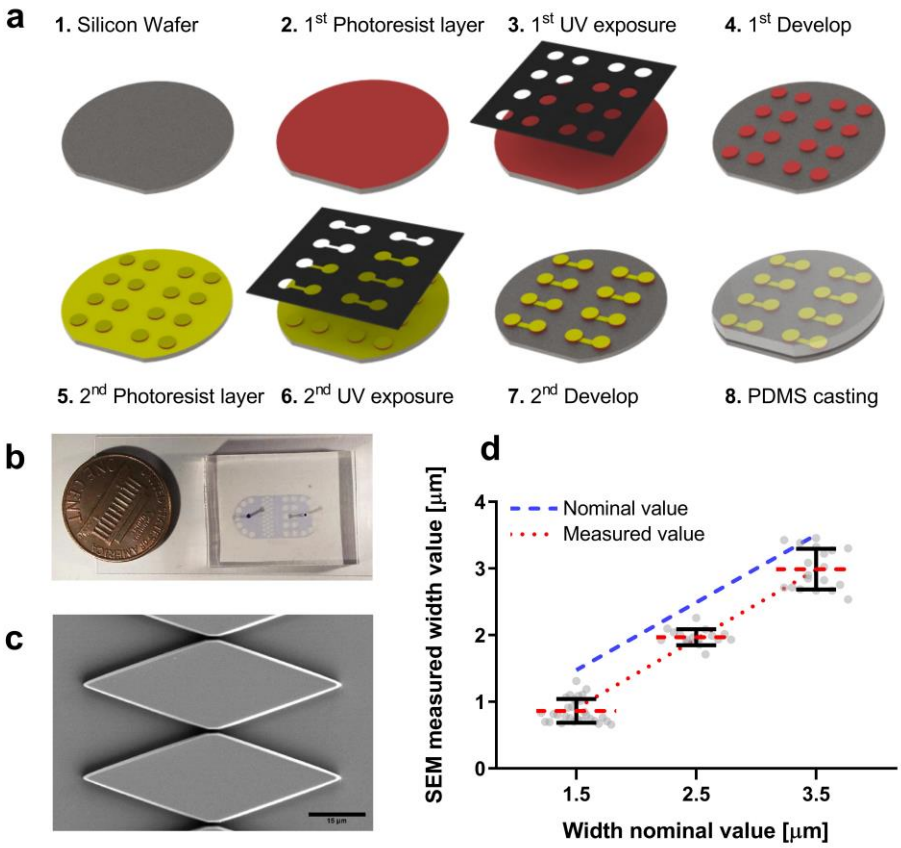

Figure 2.2: Fabrication and characterization of microfluidic devices to model the passage of RBCs through inter-endothelial slits. a) Scheme of the key steps used in the two-step photolithography process used in the fabrication of the devices. See details in the Materials and Methods section. b) Actual device next to 1-cent coin for scale. c) Scanning Electron Microscopy (SEM) image showing a close-up of the micro-constriction array. Constrictions' widths were measured using an SEM (d), although dimensions were smaller than the stipulated in the original design, the dimension were robust and the fabrication error was consistent.

The small height of the device's test section forced the RBCs to orient their discoidal plane parallel to the top and bottom walls, subjecting the cells to large-amplitude deformations when crossing the microchannels. Two types of crossing motion were observed. Most often, the RBCs folded like a "taco tortilla" (Figure 2.3 a and Suppl Video 1), a behavior previously reported in microchannels[64] and capillaries[65]. Less frequently, the RBCs twisted to progressively align their discoidal plane parallel to the microchannel sidewalls (Figure 2.3 b and Suppl Video 2). This "twisting" motion was observed to be slightly faster than "folding" as it can be seen in Figure 2.6

a. A small percentage of cells failed to cross, got trapped in the microchannel, and eventually burst. By varying microchannel geometry within a physiologically representative range[29], we found that the frequency of twisting increased with microchannel width (Figure 2.3 c). On the other hand, microchannel length did not affect the type of RBC crossing motion (Figure 2.3 d).

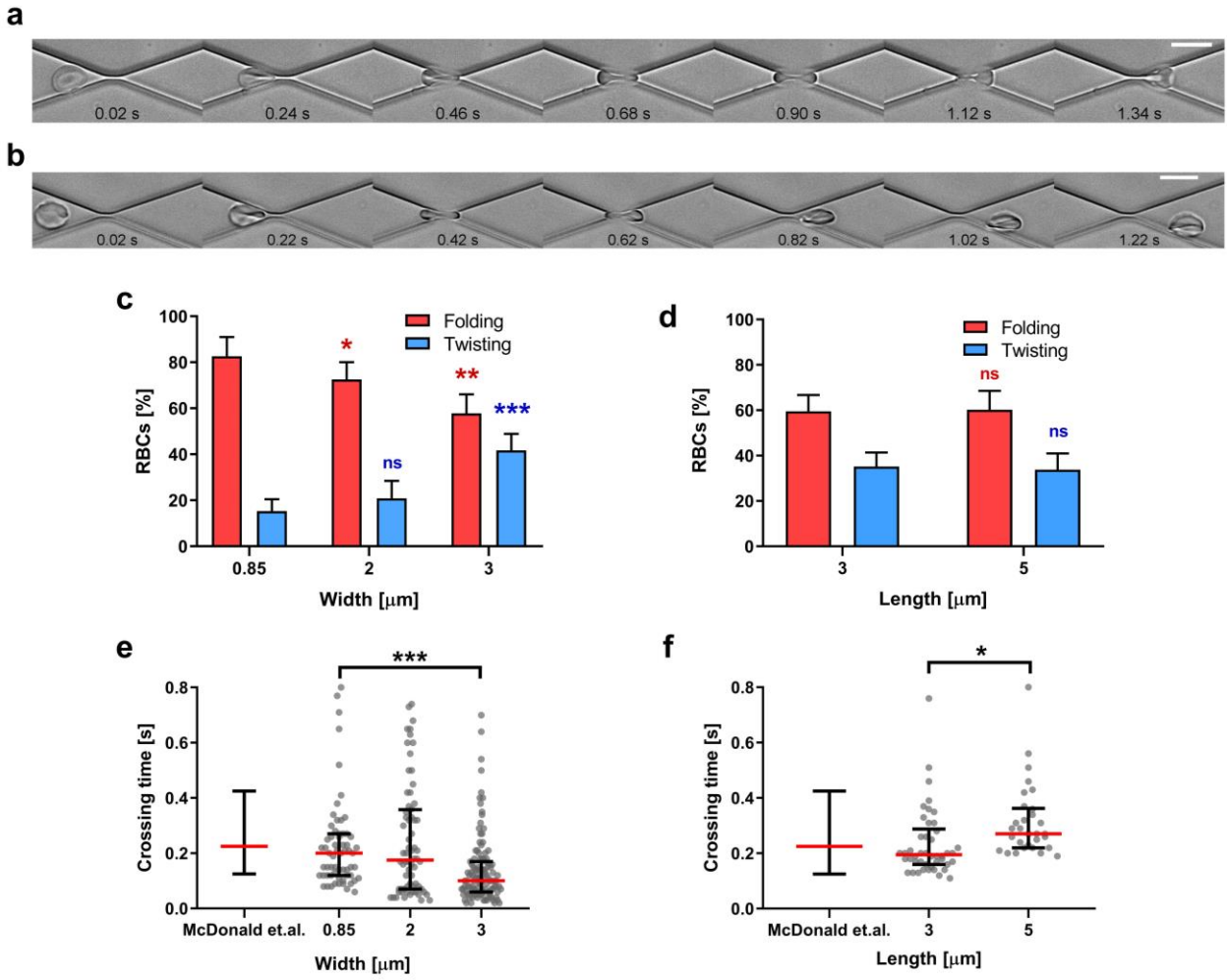

Figure 2.3: RBCs dynamics through microchannels resembling IES. Time-lapse sequences of RBC passage reveal two characteristic types of motion: folding (a) and twisting (b). See Suppl. Videos 1 and 2 for a high-time-resolution depiction of these two motions. Bars correspond to 10 μm. Type of RBCs motion was measured as a function of slit width (c) or length (d). RBCs crossing times were measured with respect to slit width (e) and length (f) and compared with in vivo data previously calculated by other authors[66]. Each cell is represented as a circle; error bars represent median and interquartile range. Statistically significant differences, as determined using an unpaired t test with Welch's correction, are indicated (*, $p< 0.05$; **, $p<0.01$, ***, $p< 0.001$).

We determined the RBC crossing time through the microchannels, a parameter strongly

related to cell deformability[67], for different configurations (Figure 2.3 e-f) showing that W = 0.85 μm yielded crossing times most consistent with available *in vivo* data[66]. Furthermore, we measured the flow profile at the inlet of the slits using particle image velocimetry (PIV) and used this profile as inflow condition for a computational fluid dynamics (CFD) simulation of the flow through the slit by the COMSOL software package. We then determined the pressure drop across the slit and the slit wall shear stress from the CFD results (Figure 2.4). Using this approach, we found that the pressure drop for W = 0.85 μm (~1800 Pa) was also consistent with physiological values measured in human spleens [68]. The final microchannel width (W = 0.85 μm), length (L = 3 μm), and height (H = 5 μm) chosen for our experiments compared well with the physiological dimensions of splenic slits reported by Deplaine *et al.[29]* (range W = [0.25-1.2 μm], L = [0.9-3.2 μm] and H = [2-5 μm]). The maximum wall shear stress was ~130 Pa (Figure 2.4 f).

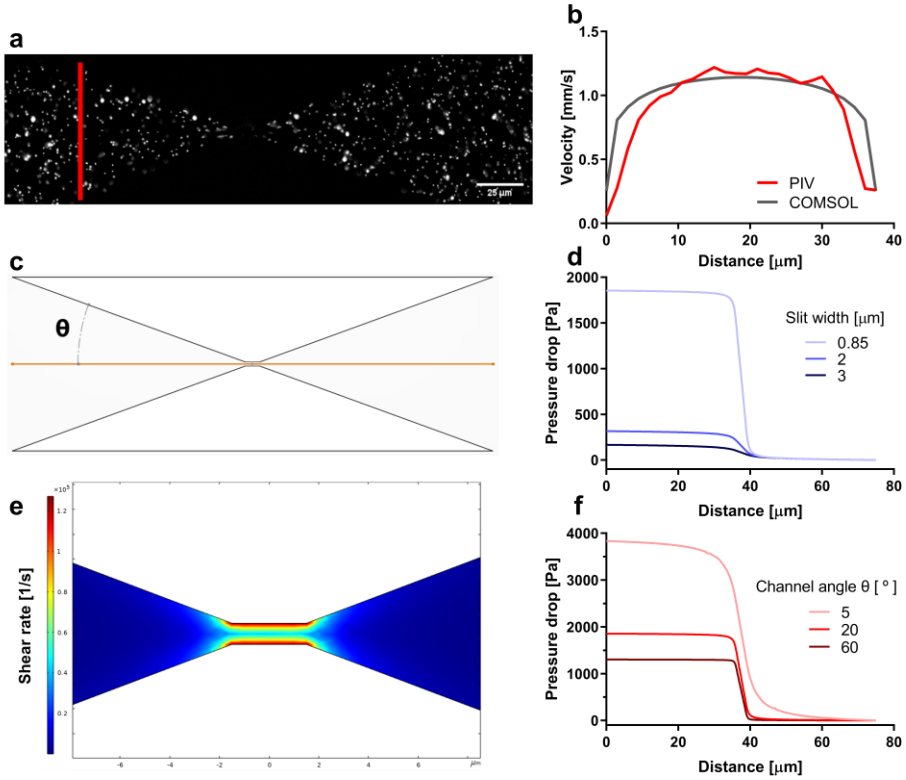

Figure 2.4: Flow characterization in the device. **a**, The flow through the device was characterized using Particle Image Velocimetry(PIV) at a high frame rate (100fps). Fluorescent nanotracers 0.1 µm were dissolved in PBS and flown through the device using the same flowrate as in the experiments. The velocity profile at the entry of the constriction (red line in panel a) was obtained using an in-house developed PIV code[69] with a window size of 3.2 µm. Scale bar represents 25 µm. The experimental velocity profile and the constriction geometry (W=0.85 µm, L=3 µm, H=5 µm) were used as an input for a COMSOL simulation using the MUMPS solver with 1.542.427 elements (**b,c**). The pressure across the orange line in (c) was calculated for slits with varying widths(**d**). Shear rate (**e**) values were calculated and yielded a maximum shear stress of 120Pa. Finally, the effect of the constriction converging angle on the pressure drop was simulated (**f**).

2.3.2 Successive crossing of microchannels promotes RBC aging

In humans, RBCs recirculate through the IES in the spleen approximately every 200 minutes leading to 400 crossings over a cell's half-life[70]. To decouple the effects of mechanical deformation from other time-dependent processes, RBCs were recirculated through our microfluidic device to cross the microchannel array approximately every 10 minutes using the set up described in Figure 2.5. Overall, we recirculated the cells up to 480 times over 3 days through

3x0.85x5-µm (length, width, height) channels. In the control experiments, RBCs were recirculated through a sham microfluidic device without microchannels.

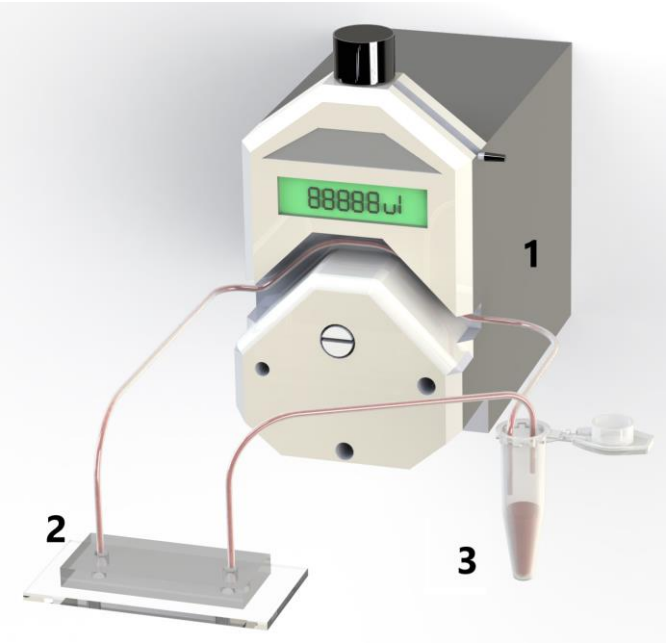

Figure 2.5: Set up used to recirculate cells through the device multiple times. A peristaltic pump (1) is used to control the flowrate through the device (2) before returning to the reservoir (3).

RBC dynamics were significantly affected as the cumulative number of microchannel crossings (Nc) increased. The crossing time grew significantly with Nc (Figure 2.6 a) implying a direct decrease in cell deformability. Compelling, the percentage of cells undergoing each motion was also modified, the ratio of folding vs. twisting significantly increased with the number Nc (Figure 2.6 b). Accordingly with a decrease in deformability, the number of cells trapped inside the microchannels (Figure 2.6 c) and RBC lysis also increased with Nc (Figure 2.6 d). Furthermore, successive microchannel crossing precipitated RBC aging hallmarks such as oxidation (assessed by RBC methemoglobin content (Figure 2.7 a) and intracellular ATP decline (Figure 2.7 b). Altogether, these data demonstrate that cyclic large-amplitude loading promotes an aged phenotype in RBCs.

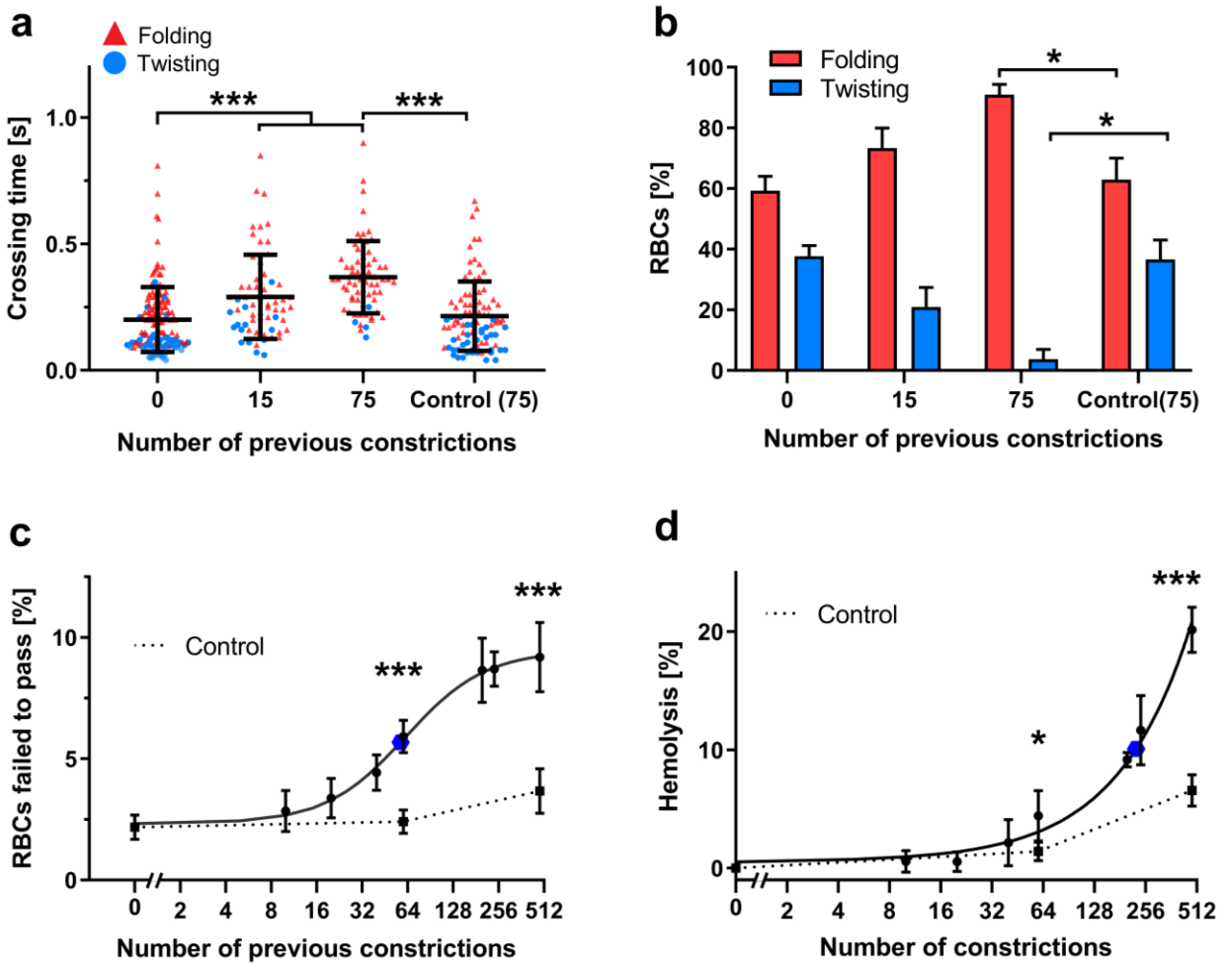

Figure 2.6: Successive crossing of microchannels simulates the effects of RBC aging. a) Crossing time was measured, as indicated in methods, in RBCs that had previously gone through 0, 15, or 75 microchannels (0.85µm width and 3µm length) by recirculating in the microfluidic circuit. Each cell is represented as a triangle or circle depending on whether it underwent folding or twisting, respectively. The control corresponds to cells that have gone to the indicated number of previous passages through a sham microfluidic device containing no constrictions. b) Percentage of cells displaying folding vs. twisting motion after previous passage through 0, 15, or 75 microchannels. c) Represents the percentage of RBCs that failed to pass through a micro-constriction vs. number of previous microchannels they have passed through. Data was modeled using the Hill dose-response equation [71,72]. d) Percentage of RBC lysis vs. number of previous microchannels RBCs have passed through. Data was modeled using a double exponential decay equation. In c-d (-●-,dots, continuous line) represent cells that have gone through devices with constrictions and (-■-, squares, discontinuous line) represent flown through a mock microfluidic device containing no constrictions. In panels a-d, the data come from at least 20 determinations of 3 independent experiments. All datapoints are represented as mean ± SD. In all the graphs the blue dot (⬣) represents the point with the 50% change. Statistically significant differences, as determined using an unpaired t test with Welch's correction, are indicated (*, $p < 0.05$; ***, $p < 0.001$).

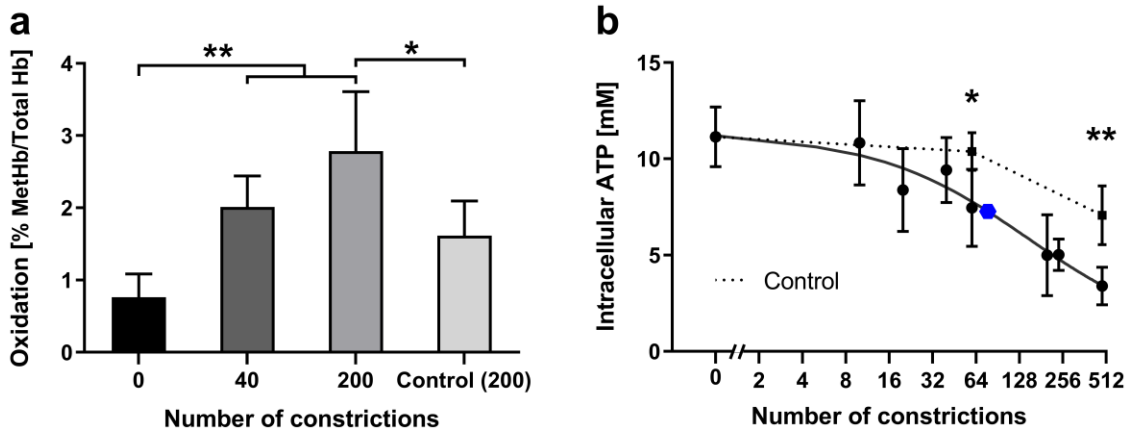

Figure 2.7:The rise of RBCs aging factors is accelerated by repetitive microchannel crossings. a) RBC oxidation was measured and plotted vs. number of constrictions the cells have previously passed. b) Intracellular ATP concentration vs. number of previous microchannels (●,dots, continuous line) and vs. number of previous passages through a mock microfluidic device containing no constrictions (■, squares, discontinuous line). Data was modeled using the Hill dose-response equation. In panels a-b, the data come from the evaluation of 5 independent experiments. All datapoints are represented as mean ± SD. In b) the blue dot (⬣) represents the point with the 50% change. Statistically significant differences, as determined using an unpaired t test with Welch's correction, are indicated (*, p< 0.05; **, p< 0.01).

2.3.3 Microchannel crossing results in RBC volume loss and vesiculation

Since RBC aging is associated with changes in cell volume and sphericity[38,73], we investigated how the cumulative crossing of microchannels affected these parameters. The sphericity index was defined as $SI = \pi^{1/3}6^{2/3}V^{2/3}/S$, where V and S are cell volume and surface area measured by fluorescence exclusion[74] (see Materials and Methods). Volume and Surface to Volume ratio measurements of control RBCs were in agreement with previous published data (Figure 2.8).

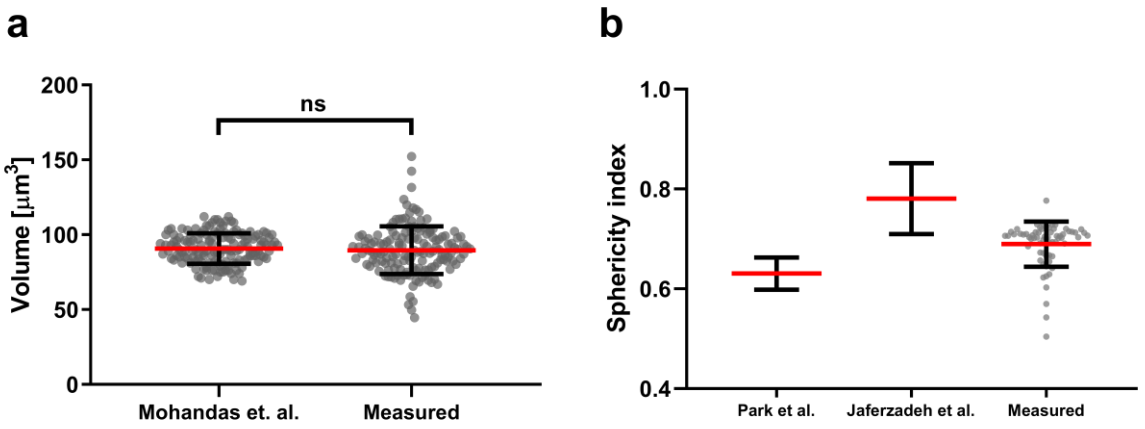

Figure 2.8: Comparison of measured cellular morphological parameters with previous determinations. Single cell volume (a) and surface to volume ratio (b) were measured using fluorescence exclusion and compared with previous studies [37,75,76]. Statistically non-significant differences were observed using an unpaired t test with Welch's correction

Then, we separated RBCs based on their density by centrifugation to independently study lighter (presumably younger) and denser (older) cells. Our measurements revealed that cells lost volume and became more spherical as *Nc* increased (Figure 2.9 a-b). These changes were more significant in lighter cells than in denser ones. In contrast, control cells circulated for an equivalent time through the sham circuit were significantly less affected. After passing through $N_c \approx 60$ microchannels, the statistical differences between light and dense cells became non-significant, implying that the young, mechanically-aged RBCs became similar to the old RBCs extracted from the circulation, providing some assurance that the mechanically-aged phenotype should be observable *in vivo*. Of note, the RBCs needed to loop in the microfluidic circuit for only 10 hours to achieve the aged phenotype. Microchannel crossing time directly correlated with cell sphericity (Figure 2.9 c) and a significant proportion of cells with $SI \gtrsim 0.9$ got stuck inside the microchannels. Consequently, the rate of microchannel RBC retention increased with the *Nc* (Figure 2.9 d). Although initially the retention percentage of denser RBCs was higher, after $N_c \approx 60$ both groups became comparable, this point coincided with the time where volume of light

RBCs become comparable with the denser ones. A different behavior was observed in the hemolysis levels (Figure 2.9 e). For a small number of microchannel crossings, the rates of hemolysis remained comparable for both groups and low overall, but eventually the lysis of denser RBCs became more pronounced than for lighter cells.

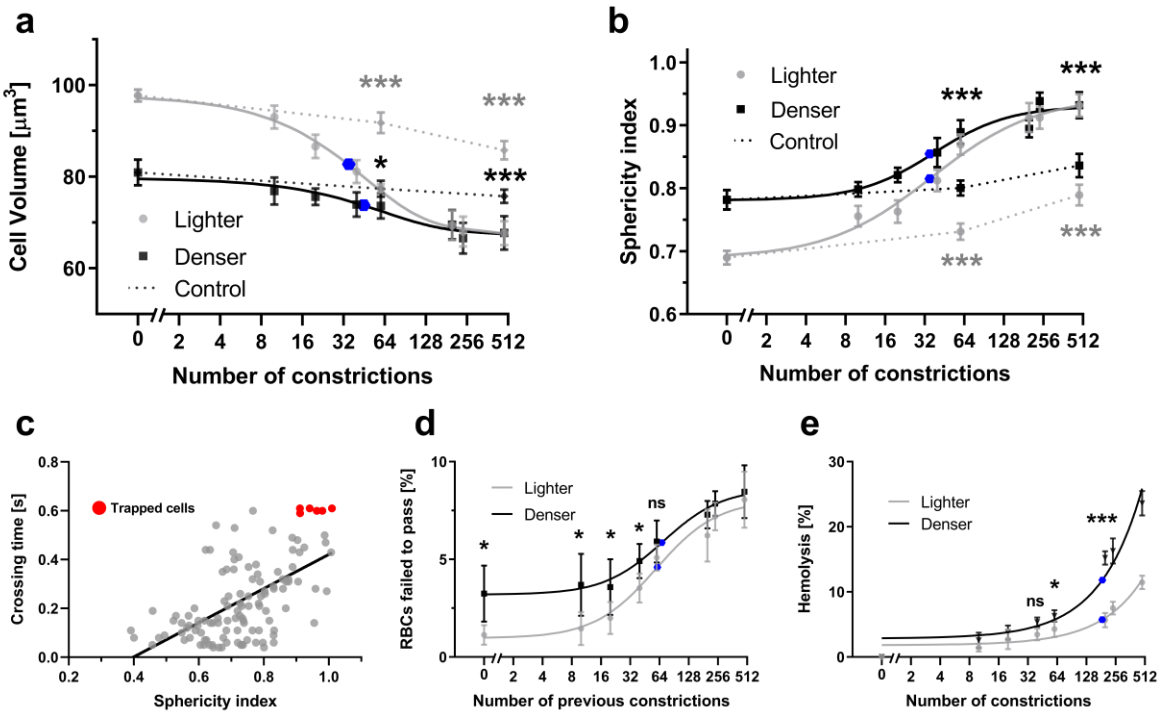

Figure 2.9: Microchannel crossings result in volume loss and increased sphericity inducing a decrease in RBCs deformability. a-b), Two subpopulations of RBCs were separated based on density and circulated multiple times through our microfluidic circuit (constrictions' dimensions: 0.85μm width and 3μm length). Cell volume (a) and sphericity index (b) were plotted vs. number of microchannels previously passed by RBCs of low-density (grey dots, ●) or high-density (black squares, ■) and compared with RBCs recirculated for an equivalent time through a mock microfluidic device containing no constrictions (control, discontinuous line; grey diamonds, ◆, low-density cells; black diamonds, ◆, high-density cells). The data are represented as mean and 95% confidence interval. c) Scatter plot of micro-constriction crossing time vs. sphericity index where each point represents a single cell. Retention rate (d) and hemolysis (e) for both denser and lighter RBC subpopulations with respect to previous or total passages is shown. Error bars represent mean ± SD. Data was modeled using the Hill-dose-response equation (a-d) or a double exponential (e). The blue dot corresponds to the point with 50% change. Statistically significant differences of at least 20 determinations of 3 independent experiments, as determined using an unpaired t test with Welch's correction, are indicated (*, $p < 0.05$; ***, $p < 0.001$).

We used membrane flickering spectrometry to assess the RBC membrane (lipid bilayer + membrane skeleton) effective tension and bending modulus. For control RBCs ($N_c = 0$), our

measurements compare well with recent membrane flickering spectrometry data [60] (Figure 2.10 a-b) and previous reports using a diversity of techniques [77-80]. As *Nc* increased, we observed that the bending modulus increased significantly (Figure 2.10 c) while tension experienced a modest, non-significant increase (Figure 2.10 d).

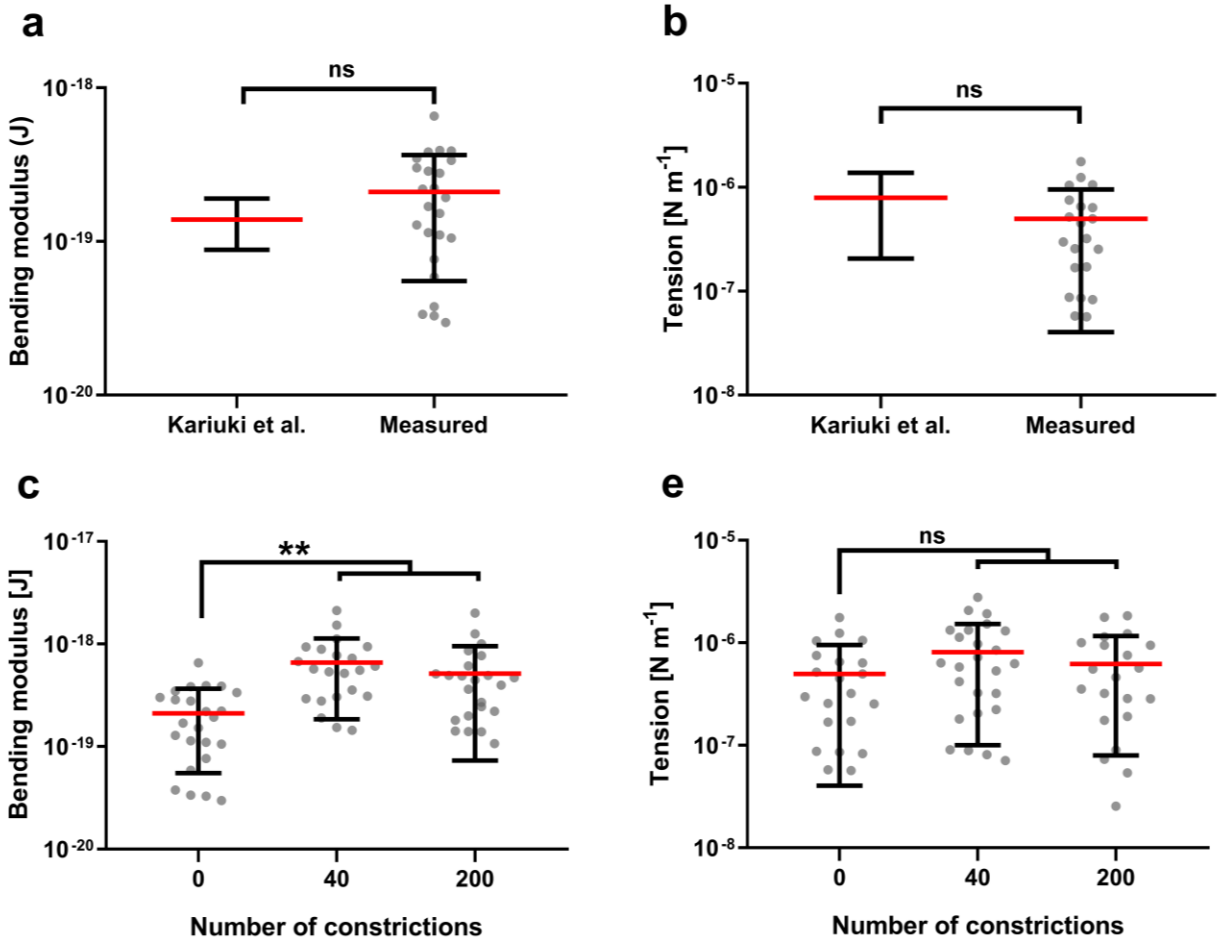

Figure 2.10: Successive microchannel crossing is associated with changes in the RBCs mechanical properties. Membrane flickering spectrometry was used to quantify membrane tension (a) and bending modulus (b); measurements were in agreement with previous studies[60]. c-d), 'effective' bending elastic modulus (c) and cortical tension (d) were assessed in at least 20 cells after they passed through the indicated number of constrictions. Each point represents a cell and the error bars indicate mean ± SD (**, $p<0.01$; Wilcoxon test).

RBC densification and volume loss have been attributed to vesiculation before[81]. Therefore, we studied whether cyclic microchannel crossing caused RBC vesiculation. Vesicle

generation was assessed by flow cytometry, which was calibrated using microbeads (Figure 2.11 a-c). Based on this analysis, RBCs generated vesicles with diameters between 0.1 and 0.5 μm, although the release of smaller vesicles undetectable by the flow cytometer cannot be discarded. RBCs subjected to cyclic microchannel crossing released significantly more vesicles than control RBCs kept in stationary conditions ($Nc = 0$) or circulated through the sham device (Figure 2.11 d). The total number of vesicles increased with *Nc* and plateaued around $N_c \approx 60$, which coincides with the value of *Nc* beyond which RBC volume ceased to decrease (see Figure 2.9 a). Thus, we concluded that volume loss was caused by vesiculation.

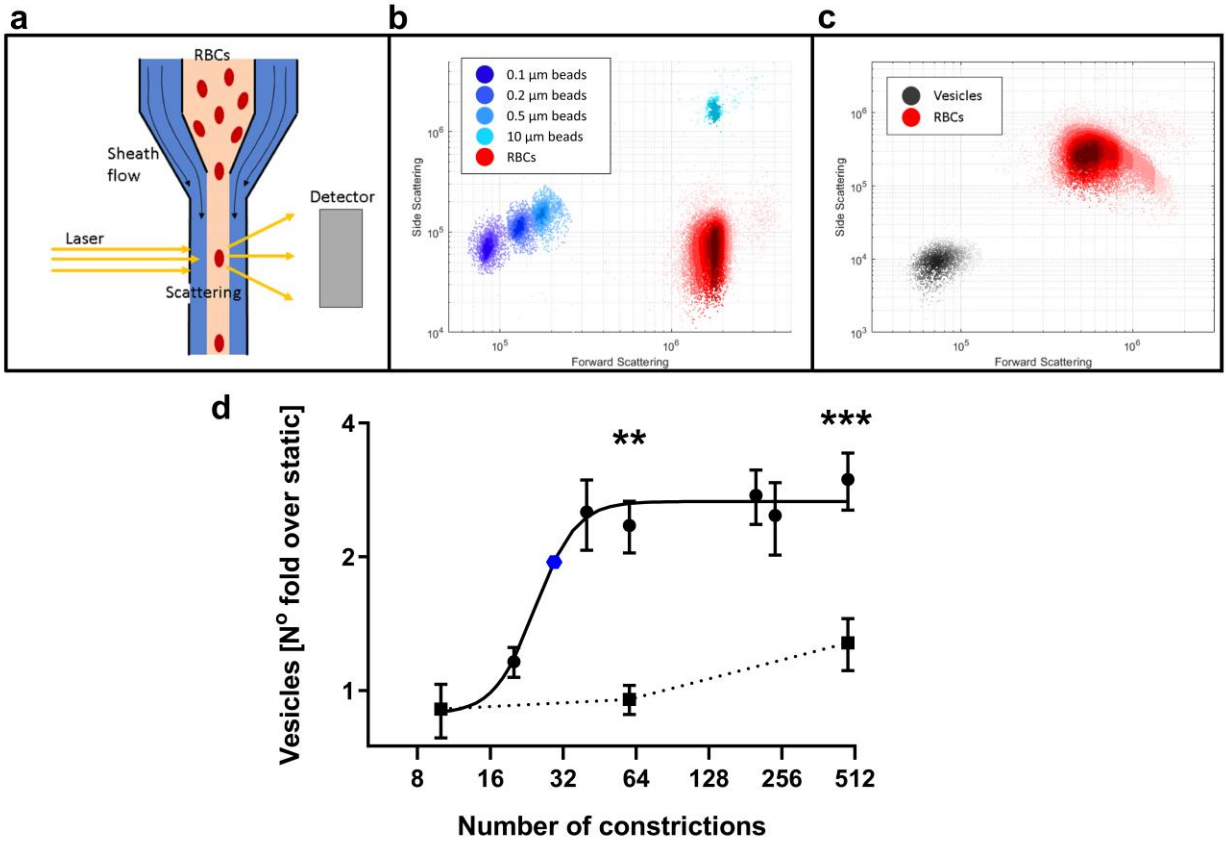

Figure 2.11: RBCs volume loss is associated with vesiculation. a) Flow cytometry was used to quantify vesiculation. Forward and side scattering were used to differentiate the vesicles from the cells. The set up was calibrated using beads of know sizes (0.1-10 µm) and compared with RBCs (b). Samples collected from the device were analyzed and a population of vesicles, comparable to beads between 0.1 -0.5 µm in diameter, was obtained (c). d) Vesicle release was determined as fold change relative to static controls. Dotted line corresponds to cells recirculated for an equivalent time through a device without constrictions. The means ± SEM of 5 independent experiments are shown. Data was modeled using the Hill dose-response equation. The blue dot (⬣) represents the point with the 50% change.

2.3.4 Successive microchannel crossings alter RBC membrane composition and cytoskeletal organization.

Our observation that cyclic mechanical loading triggered an aged RBC phenotype motivated a more comprehensive analysis of RBC composition and structure. We used mass spectrometry to analyze the protein content of RBC membranes after 200 microchannel crossings

(Figure 2.12 a, complete list in Suppl Table 1). RBCs kept in stationary conditions (*Nc = 0*) were used as controls. The volcano plot for these proteomics data was asymmetric, with few proteins substantially decreased and many others increased albeit to a lower, not significant extent (Figure 2.12 b). The list of proteins experiencing statistically significant losses with p-value < 0.01 was analyzed using Metascape [56] to investigate the most likely affected pathways (Figure 2.12 c). Protein clustering analysis revealed three affected groups. One group (Log_{10} p-value = -6.2) consisted of proteins involved in cell metabolism like ATP synthase, suggesting a reduction in overall RBC function. This group was tightly linked to a second group (Log_{10} p-value = -5.1) of proteins involved in gas transport and exchange, such as bisphosphoglycerate mutase (BPGM) and carbonic anhydrases. The third group (Log_{10} p-value = -4.6) comprised proteins involved in protection from oxidation such as catalase and peroxiredoxins, congruent with our finding that RBC oxidation increased with *Nc* (Figure 2.7). Although less significant (Log_{10} p-value = -2.8), we also found losses in structural proteins such F-actin, filamin-B, dynactin, or the ankyrin repeat domain. The quantity of other structural proteins like spectrin, band3, band4.1, or ankyrin1 remained unaltered.

a

Protein name	Log_2 Fold change	$-Log_{10}$ p-value
Bisphosphoglycerate mutase	-5.124	5.003
Catalase	-4.199	4.500
Selenium-binding protein 1	-3.665	4.257
Carbonic anhydrase 1	-2.816	4.163
Carbonic anhydrase 2	-1.323	4.133
Retinal dehydrogenase 1	-3.736	3.643
ATP synthase	-1.983	3.513
Peroxiredoxin-1	-2.302	3.504
Ankyrin repeat domain	0.294	3.475
Dynactin	-1.142	3.276
Calmodulin	-2.599	2.988
Filamin-B	2.807	2.885
Peroxiredoxin-2	-3.202	2.884
F-actin	-1.568	2.818
CD47	2.016	1.447
Glycophorin-C	3.368	1.089
Ankyrin-1	2.423	1.084
Band 3	1.989	1.050
Protein 4.1	3.043	0.988

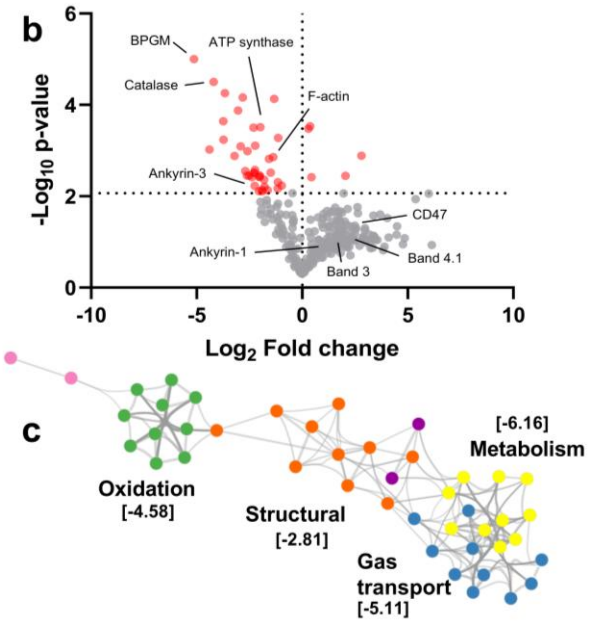

Figure 2.12: Repetitive microchannel crossings modify RBC protein composition. RBCs were subjected to 200 microchannel crossings (0.85µm width and 3µm length), membranes were isolated, and proteins were extracted and analyzed by mass spectrometry. The differences in protein content between Nc=200 RBCs and static controls are presented. Values correspond to mean of three independent analysis. a) a list of proteins significantly modified (log fold change < -2 or > 2 and a P-value >0.05) and proteins important in membrane cytoskeleton connectivity were classified by its main function. Proteins were classified based on its function, gas transport (blue), metabolism (yellow), structural (orange) and protection from oxidation (green). b) Volcano plot of all the proteins measured. Statistically significant changes were obtained by performing the Benjamini-Hochberg correction method[55]. c) Protein clustering analysis revealed that diminished proteins were mostly localized in two clusters: oxidation, gas transport and metabolism. Statistical differences in c) are indicated as [Log_{10} p-value].

The proteins connecting the RBC lipid bilayer and cytoskeleton, e.g., ankyrin1 or band4.1, form a network with a relatively regular hexagonal pattern[6,67]. Since successive microchannel crossings did not significantly affect the amounts of these proteins, we hypothesized that their inter-protein spacing in the network shortens as RBC vesiculation reduces the available plasma membrane (Figure 2.13 a). Using stimulated emission depletion microscopy (STED) and image correlation analysis (Figure 2.13 b), we quantified the inter-protein distance of ankyrin1 and band4.1 in RBCs that had transited $N_c \approx 200$ microchannels and static controls (Figure 2.13 c). Our control measurements were in agreement with previous data[82]. Moreover, we observed a significant decrease in inter-protein spacing of ankyrin1 and band4.1 for $N_c \approx 200$. Overall, these

results suggest that vesiculation depletes specific proteins essential to RBC function, while most other proteins become slightly enriched as cells become denser. In particular, the network of bilayer-cytoskeleton linkers becomes tighter, consistent with the observed increase in effective bending modulus with N_c (Figure 2.10 c).

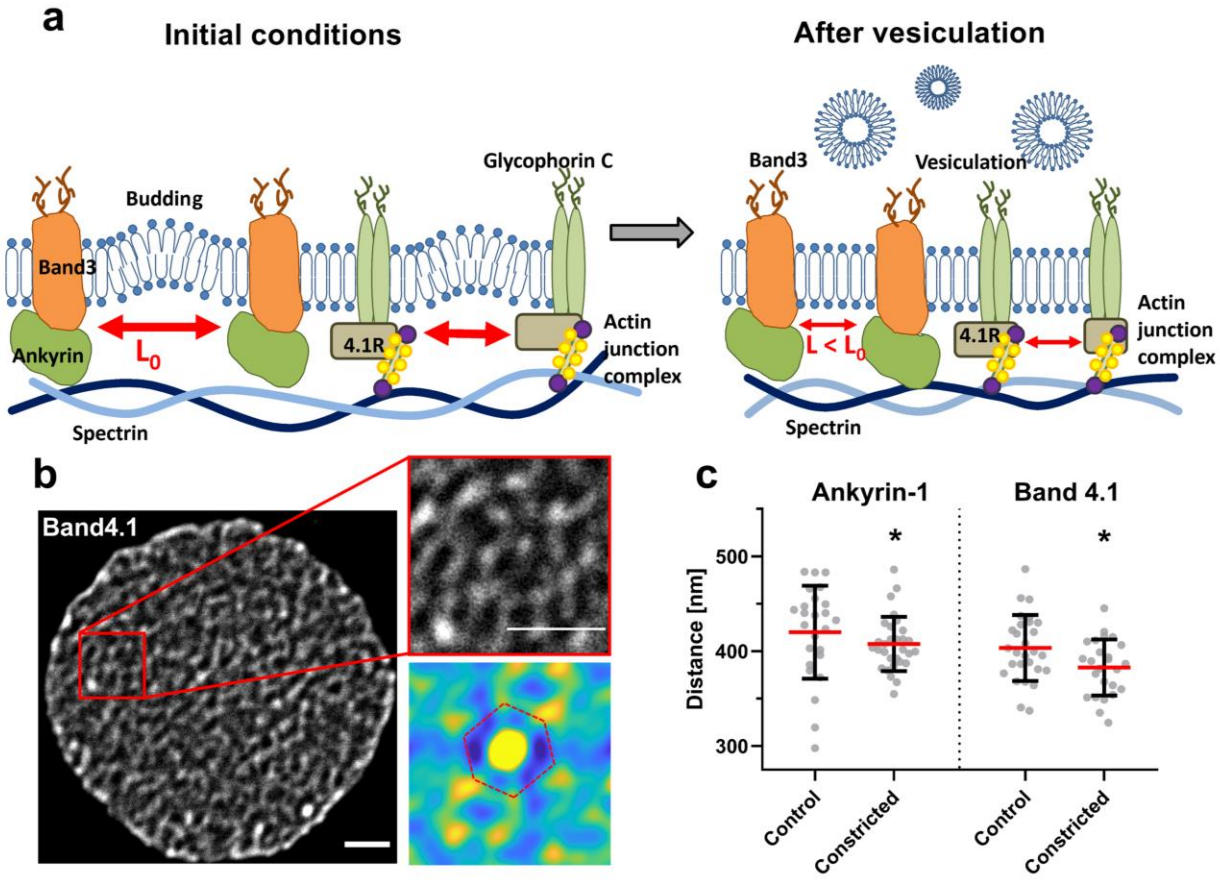

Figure 2.13: Passage through micro-constrictions increases the density of cytoskeleton-membrane anchoring complexes. a) A scheme explaining how vesiculation and membrane loss decreases the distance between the anchoring complexes that connect the membrane and the cytoskeleton . (b, c) STED microscopy was used to assess the distance between proteins that connect the membrane and the cytoskeleton (Ankyrin-1 and Band4.1) as indicated in Materials and Methods in static vs RBCs that crossed 200 microchannels (0.85µm width and 3µm length). In b), a representative image of a RBC labeled with an anti-Band4.1 antibody (scale bare 1 µm). The auto correlation matrix used to calculate the distance between two proteins is showed at the bottom. Red dashed line used to emphasize the hexagonal structure of the protein network observed in the autocorrelation image. Circles in c) represent single cell measurments and bars indicate mean ± SD of at least 25 determinations. Statistically significant differences were measured using an unpaired t test with Welch's correction and are indicated (*, $p<0.05$).

2.3.5 Cytoskeletal integrity modulates RBC aging caused by microchannel crossing

To investigate the role of cytoskeletal integrity in mechanically induced RBC aging, we treated RBCs with drugs targeting different cytoskeleton components: Blebbistatin (Blebb) and Y27632 to inhibit myosin activity, and Latrunculin A (LatA) and Cytochalasin D (CytoD) to affect actin polymerization. These treatments increased cell deformability leading to shorter crossing times (Figure 2.14 a) and lower membrane bending modulus (Figure 2.14 b), with LatA producing the most significant effects. Besides, Y27632 and especially Blebb significantly reduced membrane tension (Figure 2.14 c).

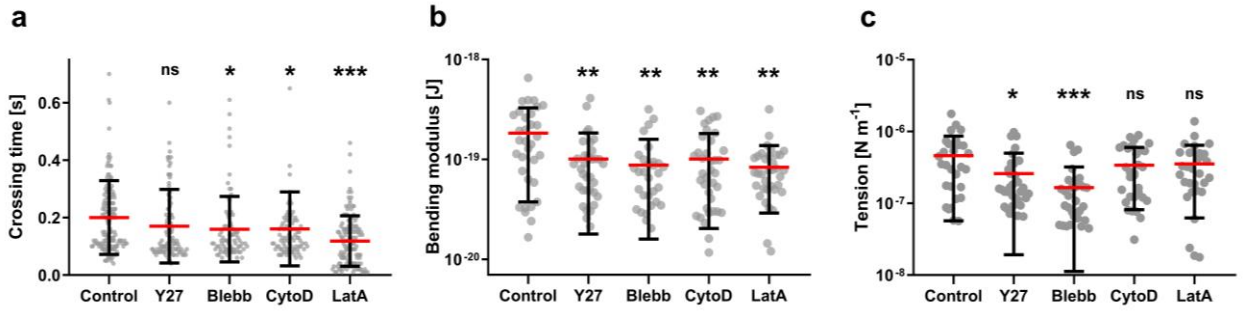

Figure 2.14: Cytoskeleton targeting drugs increase RBC deformability and reduce its bending. a) The crossing time of RBCs treated with Y27632 (Y27), Blebbistatin (Blebb), Cytochalasin D (CytoD) or Latrunculin A (LatA) (in all cases 2 µM for 30 min), and control vehicle-treated cells was measured in microchannel (0.85µm width and 3µm length). Circles represent single cell measurements and bars indicate mean ± SD of at least 25 determinations in 3 independent experiments. Statistically significant differences, as determined using an unpaired t test with Welch's correction, are indicated (*, $p< 0.05$; ***, $p< 0.001$). 'Effective' bending elastic modulus (b) or cortex tension (c) of the cells treated in the same conditions as panel a). Circles represent single cell measurements and bars indicate mean ± SD of at least 10 determinations of 3 independent experiments. Statistically significant differences, as determined using a paired Wilcoxon test, are indicated (*, $p< 0.05$; **, $p<0.01$; ***, $p< 0.001$).

Given its more potent effects, we analyzed LatA treatment in more detail. As expected, LatA induced marked changes in RBC morphology as determined by electron microscopy (Figure

2.15 a-b). Although tension was not affected, increasing LatA concentration accentuated both the decrease in RBC effective bending modulus and the number of released vesicles (Figure 2.15 c-e). Consequently, cell volume loss with cumulative microchannel crossing was amplified by LatA treatment in a dose-dependent manner (Figure 2.15 f). Despite being initially more deformable and experiencing shorter crossing times than previously reported[83], LatA-treated cells displayed increased crossing times and hemolysis (Figure 2.15 g-h) for high *Nc*, likely due to LatA-induced, accelerated mechanical aging.

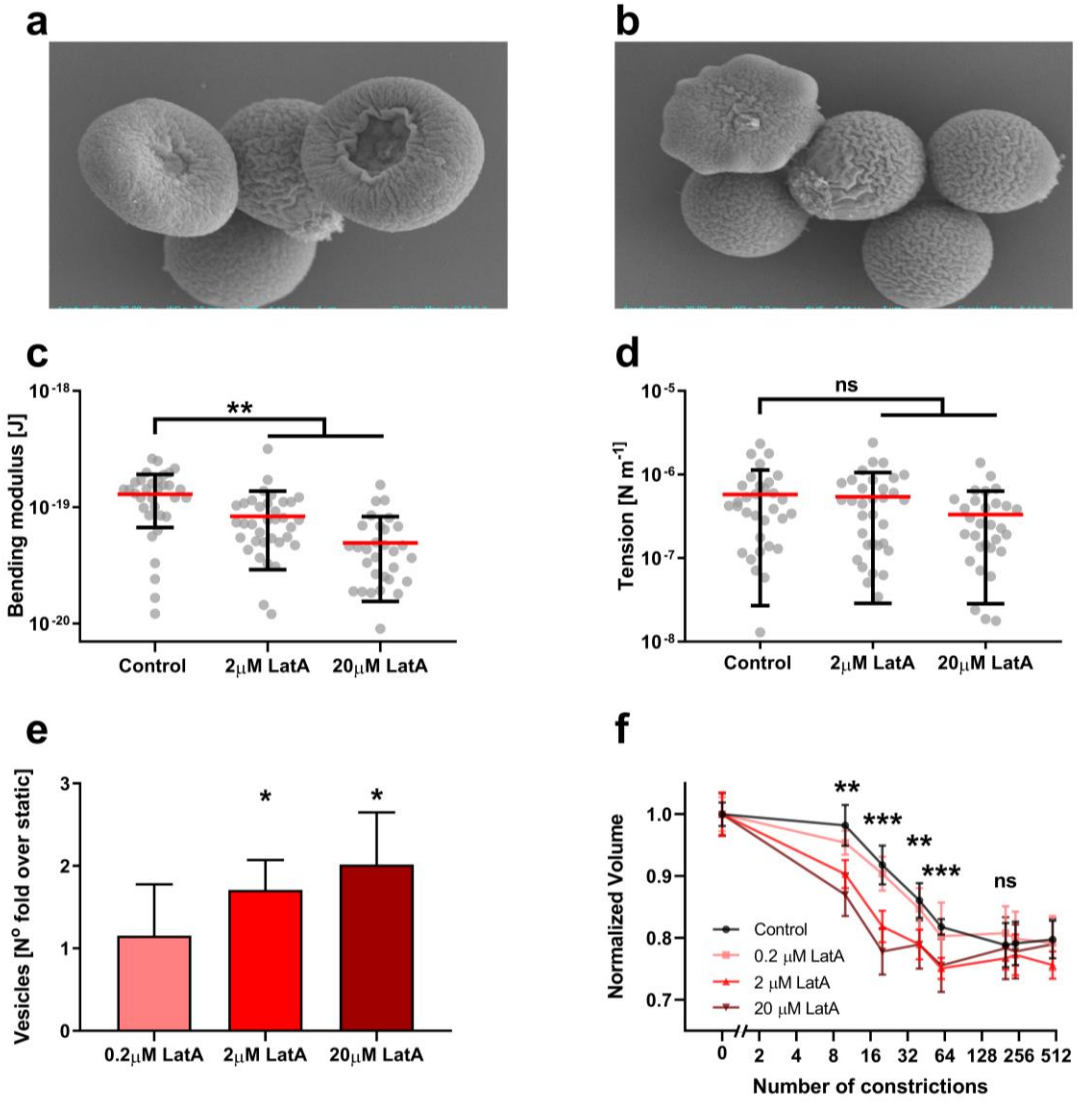

Figure 2.15: Latrunculin A treatment demonstrate a relationship between vesiculation and cytoskeletal integrity. Pictographs taken with scanning electron microscopy of control (a) and Latrunculin A (LatA) treated (b) RBCs. "Effective" bending modulus (c) and tension (d) of the cortex was measured in RBCs treated with increasing concentrations of LatA (0, 2, 20 μM). Circles represent single cell measurements and bars indicate mean ± SD of at least 10 determinations of 3 independent experiments. Statistically significant differences, as determined using a paired Wilcoxon test, are indicated (**, $p<0.01$) e) Vesiculation caused by passing through a single micro-constriction by RBC treated with different LatA concentrations. Bars indicate mean ± SD of 4 independent experiments, p values were calculated using an unpaired t test with Welch's correction and are indicated as (*, $p< 0.05$). f) Normalized cell volume vs. number of microchannels previously passed by RBCs after different doses of LatA treatment. Bars indicate mean ± SD of at least 20 determinations in 3 independent experiments.

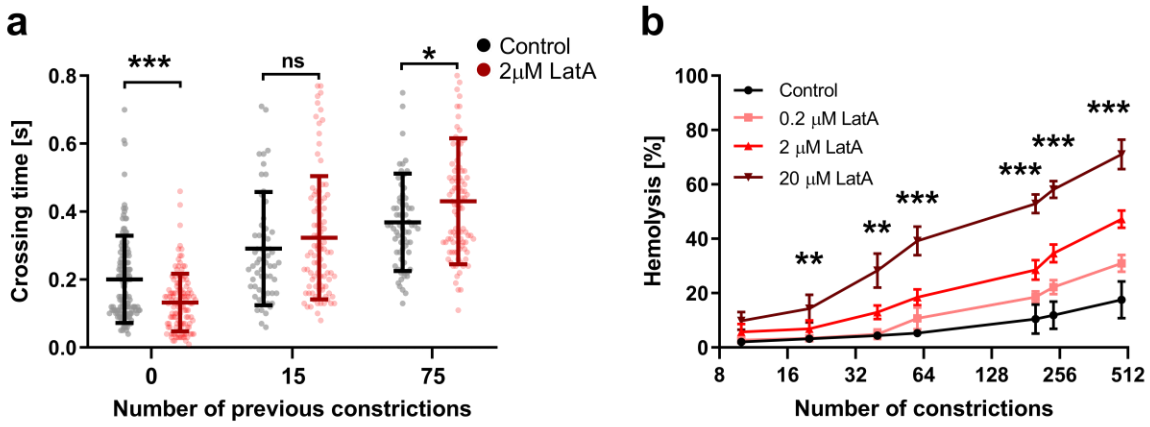

Figure 2.16: Latrunculin A treatment increases cell deformability but accelerates RBC aging. a) Micro-constriction crossing time after previous passage through 0, 15, or 75 microchannels in RBCs treated with 2 μM Latrunculin A and vehicle-control-treated RBCs. Circles represent single cell measurements and bars indicate mean ± SD of at least 20 determinations in 3 independent experiments. b) Hemolysis vs. number of microchannels previously passed by RBCs treated with different doses of LatA. Bars indicate mean ± SD of 6 independent experiments. For a-b statistically significant differences were measured between control and 2 μM LatA using an unpaired t test with Welch's correction and are indicated (*, $p < 0.05$; **, $p<0.01$; ***, $p < 0.001$).

RBC oxidation is associated with changes in cytoskeletal integrity and cell deformability[84]. Accordingly, RBCs treated with H_2O_2 exhibited increased bending effective moduli and longer crossing times (Figure 2.17), indicating a rigidized cytoskeleton. These results confirm that actin cytoskeleton integrity controls IES transit via RBC deformability. Moreover, impaired cytoskeletal integrity accelerates vesiculation, cell spherification, and other RBC aging hallmarks like hemolysis.

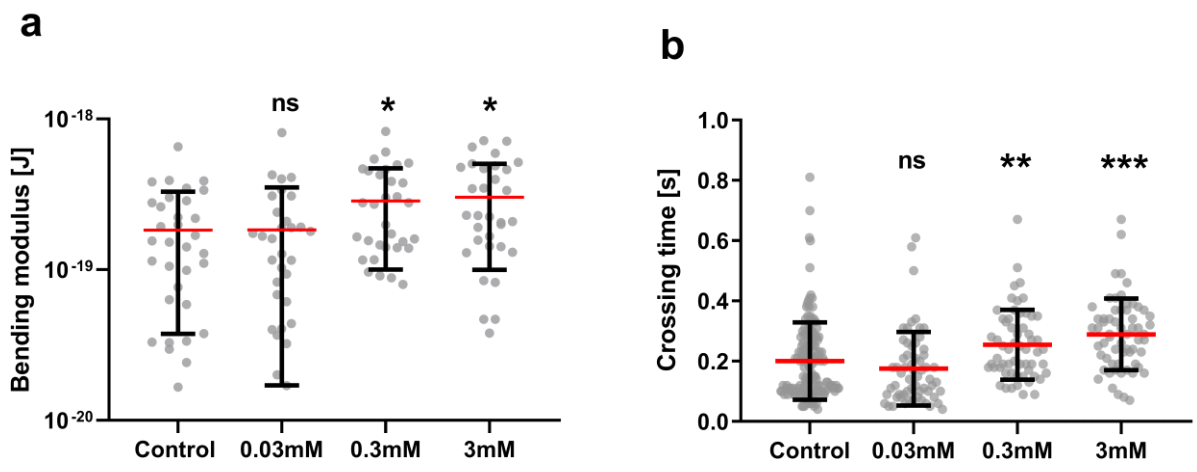

Figure 2.17: Oxidation modifies RBC physical properties. a) 'Effective' bending modulus measured with membrane flickering spectrometry of cells treated for 30 min with different concentration of H2O2. b) RBCs crossing time was assessed for different concentrations of H2O2. Statistically significant differences determined using an unpaired t test with Welch's correction, are indicated (*, $p< 0.05$; **, $p< 0.01$; ***, $p< 0.001$). Single cell measurements are represented as circles; error bars represent mean ± SD.

2.3.6 RBC aging caused by microchannel crossing facilitates macrophage attack

To address whether mechanically induced RBC aging stimulates macrophages to target RBCs, we co-cultured THP-1-derived macrophages with RBCs after Nc = 60 or 200 microchannel crossings. The RBCs were fluorescently labeled to tag macrophages that internalized RBCs (Figure 2.18 a). This experiment revealed that the number of labeled THP-1 cells and their average fluorescent intensity (Figure 2.18 b-c) increased significantly when they were co-cultured with mechanically-aged RBCs as compared to static RBCs (Nc = 0). Since target stiffness plays an important role in macrophage phagocytosis[85,86], we treated RBCs with LatA or H2O2 to respectively promote or reduce their deformability. RBC treatment with H2O2 increased phagocytosis whereas LatA decreased it (Figure 2.18 b-c).

Next, we investigated whether cyclic microchannel crossing generated molecular “eat-me” signals in the RBC membrane. We measured phosphatidylserine (PS) exposure in the outer membrane leaflet[46], finding a shallow increase in PS exposure that was statistically significant for Nc = 512 (Figure 2.18 d) but not for lower values of Nc. Thus, since we observed an increased RBC phagocytosis by macrophages for Nc = 60 (Figure 2.18 b-c), PS exposure alone does not explain increased macrophage targeting of mechanically aged RBCs. We also measured the expression of the transmembrane protein CD47, whose decline with RBC age is associated with RBC clearance[47,87]. However, we did not find any significant decrease in CD47 expression in RBCs that had crossed Nc = 40 or 200 microchannels as compared with static controls (Figure 2.18 e), consistent with our proteomic data (Figure 2.12).

Macrophage attack has also been associated with the recognition, via the Fc receptor, of cells opsonized with autoimmune antibodies (IgGs)[85,86,88]. In RBCs, clustering of specific membrane proteins like band3[43] has been shown to increase IgG binding, which could be active in mechanically aged RBCs based on our STED data (Figure 2.13). This targeting modality relies on the binding of autoimmune antibodies and their posterior recognition by macrophages via the Fc receptor[85,89]. We opsonized static and Nc = 60 and Nc = 200 RBCs with plasma from the same blood sample and measured the percentage of RBCs that bound immunoglobulin G (IgG). As shown in Figure 2.18 f, mechanically aged RBCs exhibited a significantly higher level of IgG binding than controls. Thus, we concluded that mechanical RBC aging enhances macrophage attack by a combination of increased cellular rigidity and a higher association of autoantibody opsonization, with a possible contribution from increased PS exposure at later stages of the process.

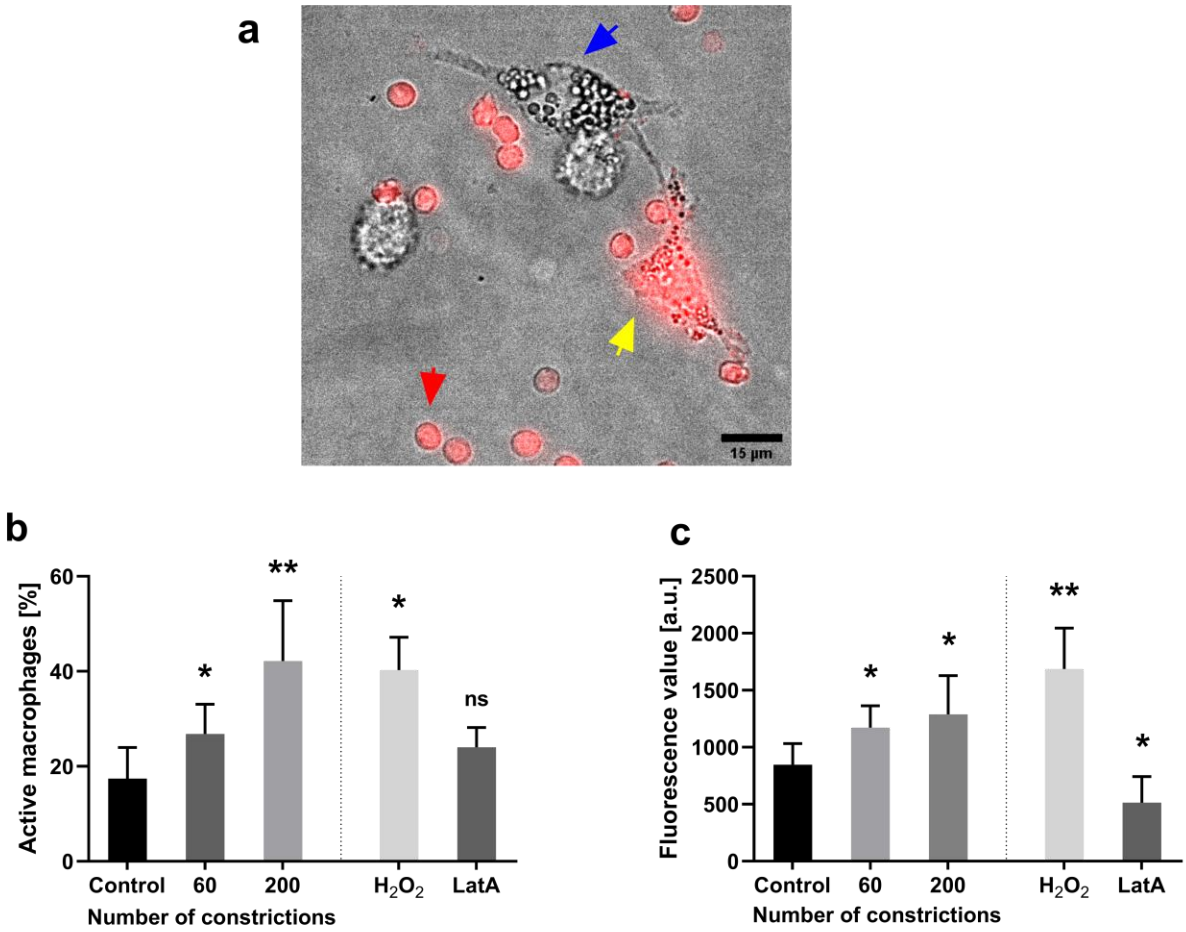

Figure 2.18: RBC passage through microchannels facilitates macrophage attack.THP-1 derived macrophages (blue arrow) were cultured with fluorescently-labeled RBCs (red arrow); an example of a macrophage that have incorporated fluorescence is shown (yellow arrow). b) Percentage of labelled macrophages detected after co-culture with fluorescent RBCs either static, after 60 or 200 microchannel crossings (0.85µm width and 3µm length) or treated with H2O2 (0.3 mM) or LatA (2 µM). c) Average fluorescence intensity of macrophages cultured with labelled RBCs treated as in panel b). In b) and c), the bars represent mean ± SD of 4 independent experiments (*, $p<0.05$; **, $p<0.01$, using an unpaired t test with Welch's correction).

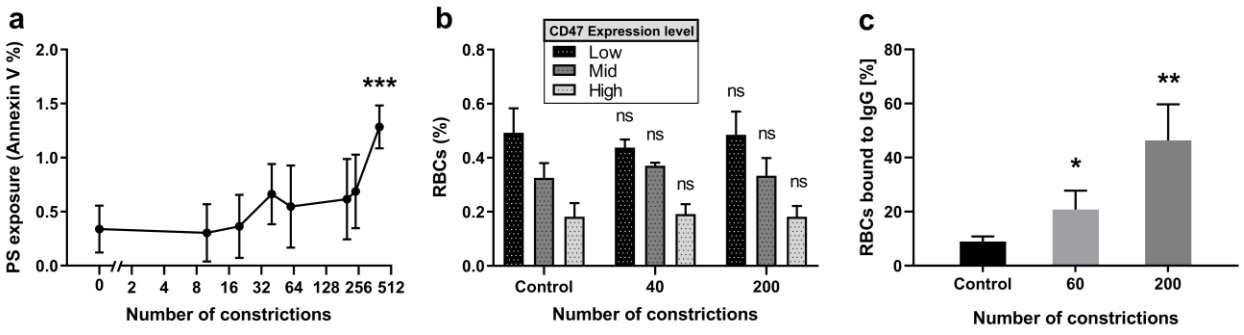

Figure 2.19: Macrophage attack is triggered by and increase opsonization of auto-immune antibodies. a) Exposure of phosphatidylserine (PS) on the outer plasma membrane of RBCs as determined by flow cytometry. A statistically significant difference was found between Nc = 0 and Nc = 480 as determined using an unpaired t test with Welch's correction, and is indicated by (***, $p< 0.001$). Note also that the Y-axis only reaches 2%. b) Expression of transmembrane protein CD47 as determined by flow cytometry. No statistically significant differences were found as determined using an unpaired t test with Welch's correction. c) The percentage of opsonized RBCs, static vs Nc= 60 or 200, that bound autoantibodies was assessed by flow cytometry. A statistically significant difference was found as determined using an unpaired t test with Welch's correction, and is indicated by (*, $p<0.05$; **, $p< 0.01$). Means ± SD of 5 independent experiments are shown in d-f.

2.4 Discussion

Red blood cells (RBCs) undergo large-amplitude deformations every time they are filtered through the inter-endothelial slits (IES) of the spleen, leading to cyclic mechanical loading. Microfluidic platforms have enabled researchers to model this process *in vitro* [63,64,80,90], demonstrating that cyclic loading lowers RBC deformability and causes structural fatigue [48,49] , two attributes frequently associated with RBC aging [29,31]. Nevertheless, much less is known about how RBCs respond biologically to cumulative large-amplitude deformations. In this work, we show that cyclic passage through narrow slits accentuates biological aging hallmarks like oxidation, ATP depletion, or hemolysis and, notably, degrades the cells' oxygen-carrying efficiency. We investigate the molecular and structural origins of these phenomena and provide a nexus between cyclic loading and RBC targeting by macrophages, which is essential to remove

aged RBCs from the circulation.

The largest deformations experienced by RBCs in vivo occur as they are filtered through the inter-endothelial slits (IES) of the spleen. Thus, we circulated RBCs through microfluidic devices that forced the cells to squeeze through narrow (< 1 μm) microchannels, causing large-amplitude deformations. The flow rate and microchannel dimensions were tuned to match in vivo measurements of IES morphology and crossing dynamics imply that RBCs can experience a wide range of mechanical stimuli when crossing the spleen [29,66]. In this work, we tuned the flow rate and microchannel dimensions to match the average IES conditions. Our device obviated other aspects that may affect RBC clearance *in vivo*, such as microenvironment elasticity, RBC adhesiveness mediated by plasma proteins like fibrinogen, platelet-RBC interactions, contact with endothelial cells including their glycocalyx forest, and naturally occurring antibody binding [64,91-93]. To extricate cyclic loading from other senescence-inducing processes like, e.g., continuous exposure to reactive oxygen species (ROS)[84], we recirculated RBCs in our devices every 10 min, an interval 20 times shorter than the period between successive splenic passages in vivo. As RBCs were recirculated, their cumulative crossing of microchannels caused a cascade of biomechanical events that accelerated cell aging.

As RBCs were recirculated through our device, the cumulative crossing of microchannels caused a cascade of biomechanical events that accelerated cell aging. The earliest signs of RBC mechanical aging were detected after 15 load cycles and involved alterations in microchannel crossing dynamics (prolonged crossing time and more frequent cell folding vs. twisting motion). These changes were accompanied by a rise in cell oxidation and a decline in intracellular ATP. Concurrently, cell volume decreased, cell sphericity increased, and the bilayer-cytoskeleton complex stiffened, rendering the cells unable to transit the microchannels and causing hemolysis.

The alterations became significant after 60 microchannel crossings, a comparable albeit smaller figure than the number of loading cycles that elicited mechanical RBC fatigue in previous *in vitro* studies[48,49]. However, those studies had slower loading timescales (~4 s [48] vs. 0.2 s) or wider microchannels (3 μm[49] vs. < 1 μm) than splenic IES filtration[29,66], the process modeled in our microfluidic devices.

The observed changes were associated with the release of sub-micrometric vesicles. Vesiculation is observed in RBCs aging in vivo or stored for transfusion[94]. Mechanical deformation can trigger vesiculation by loading the linkages between the lipid bilayer and the cytoskeleton beyond their rupture strength. Simulations suggest these conditions are met at the trailing edge of RBCs passing through < 1-μm-wide microchannels[95], and vesiculation has been reported in RBCs subjected to cyclic flow shear *in vitro*[96]. Besides, passage through constrictions elicits Ca2+ influxes[97], an ion regulating RBC bilayer – cytoskeleton anchorage and implicated in vesiculation[98]. Our proteomics experiment indicates that calmodulin, a protein involved in Ca2+ regulation, is lost in mechanically aged RBCs, suggesting these cells have impaired Ca2+ activity, which could exacerbate vesiculation.

After 60 microchannel crossings, the RBCs stopped vesiculating and reached minimum volume and maximum sphericity, supporting the theory that vesiculation shuts off as the cells exhaust their available plasma membrane[96]. Our data suggest a mechanism for vesiculation tapering based on the density of bilayer-cytoskeleton linkages. We posit that the distance between linkages gradually decreases as vesicles are released, restricting bilayer fluctuations[99]. Consonantly, we observed that the distance between ankyrin1 and band4.1, two key bilayer-cytoskeleton crosslinkers, decreases significantly in mechanically aged RBCs. Moreover, the effective bending modulus of the bilayer-cytoskeleton complex increased with cyclic mechanical

loading.

RBC aging and vesiculation have been linked to cellular oxidation, which is recognized to impair RBC deformability[100,101]. Our data suggest that the interplays between these processes are more complex than previously appreciated because mechanical loading, in turn, also weakens the RBC antioxidant defenses. Circulating RBCs are constantly exposed to ROS released by exogenous (macrophages, endothelial cells) and endogenous sources. When not neutralized by the RBC antioxidant system, these ROS alter the RBC bilayer-cytoskeleton complex to increase cell stiffness. Our proteomic analysis revealed that mechanically aged RBCs lose a significant amount of antioxidant enzymes (e.g., catalase, peroxiredoxin-1, and peroxiredoxin-2). These results imply a novel positive feedback amplification loop between mechanical and oxidative damage.

Large-amplitude mechanical deformation promotes alterations that could favor the removal of RBCs from the circulation. First, as aged RBCs become less deformable, their microchannel crossing time increases significantly. In vivo, a prolonged IES crossing time would facilitate interactions between RBCs and macrophages in the spleen. Second, membrane composition changes in mechanically aged RBCs, discussed above, could modulate phagocytic signals recognized by macrophages. We found that THP-1-derived M1 macrophages displayed higher phagocytosis of mechanically aged RBCs compared to controls. Traditionally, PS[46,89,102], CD47[47,87], and band3[35,42,89] are considered as removal signals in senescent RBCs. However, our proteomics and flow cytometry measurements did not reveal marked changes in CD47 or band3 content in the membranes of RBCs that had squeezed through microchannels. Likewise, we only detected increased PS exposure after an extremely large number of deformation cycles. Thus, we concluded that cyclic loading may elicit non-traditional “eat-me” signals. Since target stiffness is known to affect phagocytosis efficiency[85], we hypothesized that increased

oxidation of membrane proteins in mechanically aged RBCs and its associated cell stiffening facilitate macrophage attack. Consistent with this hypothesis, we observed that H2O2 treatment increases RBCs stiffness and promotes phagocytosis. In addition, mechanically aged RBCs had higher opsonization efficiency, which can contribute to RBC phagocytosis via the Fc receptor in macrophages. Autoantibody binding has been related to band3 oxidation[89]. Therefore, we surmise that the increased phagocytosis of mechanically aged RBCs arises from the combination of auto-antibody opsonization and increased cell rigidity and oxidation.

Vesiculation allows RBCs to shed membrane fragments containing pro-phagocytic molecules like PS or denatured band3[103]. In this regard, vesiculation is believed to protect RBCs until it progressively shuts off with cell age. We tested whether treating RBCs with LatA, a drug that drives F-actin depolymerization, would prolong vesiculation, preserve the cells' deformability, and prevent the aging effects induced by cyclic loading. However, while it initially increased cell deformability and protected the cells from macrophage attacks, LatA treatment also accelerated vesiculation shut off and the adoption of a fragile spherical phenotype. Overall, our results imply that vesiculation introduces a clock in RBC functional decline, winding up with impaired cell deformability, reduced antioxidant protection, decreased gas transport and exchange, and increased macrophage phagocytosis. Notably, we have shown that this clock can be hastened by cyclic mechanical loading.

2.5 Acknowledgments

Chapter 2, in part, has been published in the journal Advanced Science 2022. Garcia-Herreros, Antoni; Yeh, Yi-Ting; Peng, Zhangli; del Álamo, Juan C. The dissertation author was the primary investigator and author of this material.

Chapter 3. Tunable photoinitiated hydrogel microspheres for cellular force quantification in complex three-dimensional environments

3.1 Introduction

Mechanical forces play crucial roles in regulating physiological functions including organ development and tissue homeostasis. Cells constantly sense and respond to mechanical cues from their surroundings by exerting forces. In the past two decades, it has become clear that mechanical forces influence embryonic development[104], cancer progression[105], or stem cell differentiation[106]. However, the physical and molecular mechanisms by which these forces, applied to specific adhesion receptors[107] or non-specifically, trigger gene expression and affect cellular function are far from being completely understood. In particular, there is a need for interrogating cellular forces in vivo or in physiologically relevant *in vitro* models with increasing similarity to living tissues.

The usage of linearly elastic flat substrates seeded with fluorescent beads transformed the field of cell biomechanics by allowing researchers to measure the 2D[108-110] and 3D [69,111,112] traction forces exerted by cells and the intracellular stresses inside thin, continuous cell monolayers adhering to these substrates[113,114]. Traction force microscopy and monolayer stress microscopy have become widespread methods in cell biology with relatively well

standardized protocols and analysis techniques. Progress in modeling the non-linear mechanics of fibrillar extracellular matrices has made it possible to reconstruct the forces generated by cells in these complex environments[108,109]. These approaches have in common that they rely on constitutive laws, whether known a priori, modeled, or inferred, that relate strain and stress in the extracellular environment. However, it is challenging to determine the constitutive laws of three-dimensional environments formed by other actively contracting that constantly remodel, which are critical properties of living tissues.

An effective strategy to measure mechanical forces in complex multicellular cultures and living tissues consists of fabricating calibrated microscopic (~10-100 μm) probes and intercalating them into the experimental region of interest. This approach obviates the problem of obtaining the complex strain-stress relationship of the tissue. One of the first systems to report forces in living tissues used fluorocarbon oil droplets[115,116], whose physical properties are well characterized. By tracking droplet shape deformations, the anisotropic component of the tissue normal stresses were determined via the Young-Laplace's equation. While droplets do not detect shear stresses or isotropic normal stresses (i.e., pressure), due to their fluid, incompressible nature, they have become widely used due to their easy implementation and non-toxic nature for in vivo experiments. Liquid droplets can be directly injected into the tissue but require a precise control of the surface chemistry to prevent surrounding tissues from interacting with the highly deformable interface to the point of rupture and posterior internalization of the surfactant or oil.

On the other hand, hydrogel micro-spheres offer an alternative to microdroplets for measuring shear and pressure[117,118]. These micro-spheres can be fabricated in great quantity by generating a suspension of aqueous droplets in oil, where the aqueous phase contains a gel

precursor solution. Vortexing the oil and aqueous phases is a simple method to produce droplet suspensions if obtaining a monodisperse size distribution is not crucial [25,119]. On the other hand, flow focusing microfluidic devices[120-122] yield monodisperse droplet distributions and are becoming increasingly available. Most recent techniques are based on the polymerization of acrylamide, but several studies have utilized other materials, like alginate or gelatin [24,123], whose stiffness is harder to control and/or varies within a relatively narrow range, limiting their usability. However, while polyacrylamide microspheres with adjustable stiffness and size can be fabricated, obtaining monodisperse distributions of these properties involves complicated microfabrication setups depending on highly specialized equipment[124] and very careful tuning of the hydrogel polymerization process[125].

We present a new approach to generate polyacrylamide (PAAm) micro-spheres with monodisperse, tunable mechanical properties and custom surface chemistry. We use in-house manufactured microfluidic devices to produce droplets of a polyacrylamide precursor solution containing the biocompatible, water-soluble photoinitiator Lithium phenyl-2,4,6-trimethylbenzoylphosphinate (LAP). Compared to other commonly used initiators, LAP can be activated sharply in response to ultraviolet light and has low solubility in the oil phase, providing precise control over the polymerization process. Our microfluidic device is designed to generate droplets of adjustable size in real time by varying the flow rates between the two liquid phases, without modifying device geometry or restarting the experiment. Finally, the precursor microdroplets contain fluorescent nanoparticles to track micro-sphere deformations through three-dimensional image correlation techniques. Overall, we demonstrate the high-throughput production of cellular force microscopy probes of highly tunable, reproducible properties without

highly specialized equipment or involved processes in a high throughput manner.

3.2 Materials and methods

3.2.1 Microfluidic devices design and fabrication

A series of in-house designed and manufactured polydimethylsiloxane (PDMS) microfluidic devices were used to manufacture and collect the hydrogel microdroplets. Microfluidic devices were manufactured using soft lithography. The master device for the microchannel microfluidic device was fabricated in a sequential manner initiated by applying a coating of MCC Primer 80/20 (Microchemicals, Westborough, MA) spin coated at 3000rpm, accelerating at 1000rpm/s and with a duration of 30 seconds into a 4 inch single side polished silicon wafer (University Wafer, South Boston, MA). Shortly after, a first layer of positive photoresist AZ-12XT-20PL-10 (Microchemicals, Westborough, MA) was also spin coated on top of the primed silicon wafer at 500rpm accelerating at 100rpm/s for 10 seconds. After a short soft bake at 110ºC for 2 min, we exposed (250mJ/cm2) the sample under a 375 nm laser using a MLA150 mask-less aligner (Heidelberg Instruments Mikrotechnik GmbH, Germany) fed with the drawings of our device. A post-exposure bake of 1 min at 90ºC was performed and the features were obtained by developing the sample for 2 min using AZ-300MIF (Microchemicals, Westborough, MAs). Two 1 min rinses with deionized water were performed to clear the sample from residues. Profilometry measurements using a Dektak 150 surface profiler (Veeco Instruments Inc. Plainview, NY) confirmed the expected thickness of 20_m. Afterwards, the wafer was passivated with tridecafluoro-1,1,2,2-tetra-hydrooctyl-1–1trichlorosilane (Gelest, Morrisville, PA) for 15 min inside a vacuum chamber to prevent PDMS adhesion to the wafer in the casting phase of the manufacturing process.

PDMS replica of the device was made by carefully casting a previously degassed (during 30 min) mixture of the PDMS oligomer and crosslinking agent (Sylgard® 184, Dow Corning Inc. Midland, MI) in a 10:1 (w/w) proportion on the passivated silicon wafer. The sample was then cured at 65ºC overnight. The next day the master was peeled off the wafer, cut into several single devices and the inlet and outlet holes were punched (2.5 mm) with a biopsy puncher (Miltex, Integra Lifesciences, Plainsboro Township, NJ). Finally, we activated the surface of both the bottom coverslip (Corning, 24x60 mm and thickness 1.5 mm) and PDMS chip under a UV ozone lamp (Model 30, Jelight Co. Irvine, CA) for 4 min with an oxygen inflow of 0.2 lpm and bonded them together at 65ºC (to facilitate thermal bonding) for a minimum of 4 hours before they were ready to be used.

3.2.2 Functional polyacrylamide microspheres generation

Polyacrylamide microdroplet generation

The pre-gel solution was prepared by mixing 25 µL of 40 % Acrylamide (Millipore-Sigma,Burlington, MA), 30 µL of 2% Bis-Acrylamide (MilliporeSigma,Burlington, MA), 3µL of 2% 0.2 µm carboxilated FluoSpheres (Invitrogen, Carlsbad, CA), 20 µL of 20mM Lithium phenyl-2,4,6-trimethylbenzoylphosphinate (LAP, Sigma-Aldrich, St. Louis, MO) and 122 µL of deionized water to a total volume of 200 µL that yielded gels of ~9kPa. According to the desired hydrogel stiffness the proportion of Acrylamide to Bis-Acrylamide can be re-adjusted[126]. Afterwards, the solution was kept always cold (4ºC) inside an amber UV-protected 1.5 mL microcentrifuge tube (Eppendorf®, Hauppauge, NY), and prior to the experiment it was degassed for one hour inside a vacuum chamber to prevent gelation inside the syringe while running the experiment.

The oil phase was prepared by mixing the surfactant oil Krytox® 157 FSH (DuPont, Midland, MI) (10% w), a functionalized version of the DuPont series of Krytox® fluorinated oils

that acts as a surfactant, into HFE 7500 Novec Engineered Fluid (3M, Maplewood, MN). Afterwards, both pre-gel and oil solutions were added to different 1 mL syringes and connected to their respective inlets in the microfluidic device using PTFE tubing (1/32”ID and 3/32”OD). Flows inside the device were controlled using two syringe pumps (NE-300 and NE-4000, New Era Syringe Pump). Flow rates were adjusted according to devices dimensions, desired droplet size and droplet generation frequency. For a typical droplet size of ~35 µm, we used a channel width of 30 µm and flowrates of 60/20 (Oil/Pre-gel) µL/h.

The steady state was typically achieved after 15 min and the device was left running for a minimum of 3 hours while droplets were being collected in a 1.5 mL microcentrifuge tube (Eppendorf®, Hauppauge, NY).

Droplet collection and polymerization

The device was left running for 3 hours to generate a sufficient amount of droplets that were collected directly from the outlet of the microfluidic device inside an amber UV-protected 1.5 mL microcentrifuge tube (Eppendorf®, Hauppauge, NY). The solution containing the droplets was transferred into a regular transparent microcentrifuge tube and polymerized them by exposing the tube to UV (302nm) light with a benchtop transilluminator (UVP, Analytik Jena US LLC, Upland CA) for 15 minutes. Once polymerization was completed, PBS was mixed with oil and microspheres solution and centrifuged at 3500 rpm (Sorvall Legend RT, Beckman Coulter Inc. Indianapolis, IN). After centrifugation, the oil phase remained at the bottom of the vial and it was carefully removed with a pipette tip. The centrifugation-resuspension process was repeated multiple times to extract all the oil and ensure that there was no surfactant left.

Surface activation and coating with protein of interest

Surface activation of hydrogel beads for protein conjugation was done following the

standard procedure for planar polyacrylamide gels[126]. First beads were pelleted by centrifugation at 3500 rpm and then 1 mL of 0.2mg/ml Sulfo SANPAH (Thermo Fisher Scientific, Waltham, MA), a heterobifunctional protein cross-linker used to covalently bind proteins to polyacrylamide substrates, was added to the microcentrifuge tube. The sample was then exposed under UV light (254nm) for 7 minutes followed by a centrifugation step and posterior wash with PBS 1X. This process was repeated twice. The N-hydroxysuccinimide ester in sulfo-SANPAH can then react with the primary amines of proteins to complete the attachment of proteins to the surface of the gel. To bind the desired protein (FN-FITC, ICAM-1) with the activated polyacrylamide beads, we incubated the beads in a solution containing 50 µg/mL of the protein conjugate in PBS at 37 °C for a minimum of 3 hours. After this step, the beads were cell-compatible and ready to use.

Fabrication of polyacrylamide microbeads by inverse emulsification via vortex mixing

Inverse emulsification of the PAAm pre-gel solution was performed dissolving 50 µL of the pre-gel solution in 500 µL of HFE 7500 Novec Engineer Fluid (3M, Maplewood, MN) containing (10% w) of the surfactant Krytox® 157 FSH (DuPont, Midland, MI) inside a 1.5 mL Eppendorf tube. After that, the mixture was vacuumed for 15 min and subsequently vortexed for 1 min at maximum speed using a vortexer[25]. Right after, the Eppendorf tube was directly exposed to UV (302nm) light with a benchtop transilluminator (UVP) during 15 minutes to allow polymerization. Once polymerization was completed, PBS was added and mixed thoroughly in the vial just before the solution was centrifuged for 1 min at 3500 rpm (Sorvall Legend RT, Beckman Coulter Inc. Indianapolis, IN). Then the oil phase was carefully removed and the beads were resuspended in PBS and stored at 4C. The centrifugation-resuspension step was repeated 3 times

for improved purity of the resulting beads solution in PBS. The subsequent surface activation and coating with protein of interest were performed in the same manner as described in previous sections.

Planar polyacrylamide Gels Fabrication

Collagen-coated PAAm gels of ~20 μm thickness and 12 mm in diameter were prepared as cellular substrates as previously described [20,111]. Basically, squared 25 mm coverlsips were initially prepared by activating them inside a UV ozone lamp (Model 30, Jelight Co. Irvine, CA) for 10 min and then coating them with a 1M solution of NaOH in deionized (DI) water for 5 min. After this step, the NaOH solution was washed, the coverslip rinsed with DI water twice and completely dried using a vacuum line. Afterwards, the surface of the coverslip was covered with a solution of 3% (v/v) (3-Aminopropyl)triethoxysilane (APTES, Sigma-Aldrich, St. Louis, MO) in ethanol for 20 min at room temperature. After this step, the surface of the coverslip was washed with pure ethanol and the coverslip was soft baked for 5 min at 37 °C. The amino-silanated coverslips remained usable for a 48 hours period. In case a stronger bond between the coverslip and the PAAm gel is required, this can be achieved by including an extra step consisting of covering the amino-silanated coverslips with 0.5% (v/v) Glutaraldehyde (Sigma-Aldrich, St. Louis, MO) in Phosphate Buffered Saline (PBS) for 30 min at room temperature. This mild and relatively fast reaction (Schiff base reaction) between compounds containing aldehydes (or ketones) and amino groups, result in covalent, and hence stronger, imine groups (Schiff base) that will bind the PolyAcrylamide gel in a stronger manner[126]. Once the coverslips were ready, the pre-gel solution was prepared by mixing the components to a final concentration of 5% Acrylamide and 0.3% Bisacrylamide (8.7 kPa,[126]) and seeded them with 0.03% carboxilated FluoSpheres (Invitrogen, Carlsbad, CA). Then, 1% (v/v) of 10% (w/v) Ammonium Persulfate

(APS, Sigma-Aldrich, St. Louis, MO) in DI water, was added into the solution as well as 1µl of N,N,N',N'-Tetramethyl ethylenediamine (TEMED, Sigma-Aldrich, St. Louis, MO) to initiate the polymerization reaction. We then pipetted 3 µL of the pre-gel solution on top of the silanized coverslips, placed a round 12mm coverslip on top, and immediately inverted the mixture and let the gel polymerize for 30 min. During polymerization, the microspheres migrated to the bottom (i.e., the free surface of the gel). To activate the surface of the gels, 0.15 mg/mL Sulfo-SANPAH (Thermo Fisher Scientific, Waltham, MA) solution in DI water was used to cover the gels, followed by UV activation to facilitate the cross-linking of 125 µg/mL of rat tail Collagen Type I (Dow Corning Inc. Midland, MI). The gels were incubated for 1 hour at 37 °C and then equilibrated with medium for at least 3 hours. We measured the thickness of the substrates by locating the top and bottom planes of the gel and subtracting their vertical positions as previously described[20]. The Poisson's ratio of the gel was measured to be 0.46, following an elastographic traction force microscopy method previously developed[127].

3.2.3 Microscopy

Confocal microscopy

Three dimensional z-stack bright field and fluorescent images of samples were taken using an Olympus IX81 confocal microscope (Olympus Corp. Tokyo, Japan) with a cooled CCD camera (Hamamatsu Photonics, Shizuoka, Japan), using Metamorph software (Molecular Devices LLC. San Jose, CA) and a 40× N.A. 1.35 oil-immersion objective. Following the acquisition, the sequences of z-stack images were analyzed using the software suite Volocity (PerkinElmer, Waltham, MA), which rendered some of the optical sections into 3D models.

Airy scan imaging and confocal data preprocessing

The higher resolution imaging for single beads study was performed on an enclosed Zeiss LSM 880 Confocal microscope (Carl Zeiss AG, Oberkochen, Germany) with superresolution capabilities under the fast Airyscan mode. A 40x water lens was used. For experiments solely related to characterizing PAAm microbeads shapes, a 200 µm stack with either 1.21 µm or 2.21 µm spacing was acquired. The in-plane calibration factors were 0.0824 µm/px and 0.123 µm/px, respectively. For every experiment, 4 different fluorescent channels were acquired: DAPI, FITC, TRITC and CY5. The duration of timelapse experiments varied.

Scanning Electron Microscopy

To prevent the presence of any organic contaminants inside the Scanning Electron Microscope (SEM), we fixed the samples using a fixative buffer composed of 4% Paraformaldehyde (PFA, Biotium, Freemont, CA) supplemented with 2.5% of Glutaraldehyde (Sigma-Aldrich, St. Louis, MO) in Phosphate Buffered Saline (PBS). We first aspirated the medium in our samples, covered them completely with the fixative buffer and incubate overnight at 4 °C. The, the buffer was replaced with the a sequence of increased concentration ethanol solutions (50,60,75,85,90 and 100%) and left for 15-20 minutes.

The samples were then dehydrated and ready for drying. To prevent collapse of biological samples due to surface tension, Critical Point Drying (CPD) was performed on all samples following dehydration using a Tousimis AutoSamdri 815A critical point dryer (Tousimis, Rockville, MD). After CPD, the sample was ready for sputter coating performed on a Emitech K575X Iridium Sputter Coater. Imaging was thereafter performed using a FEI Quanta FEG 250 SEM with environmental capabilities. Images were acquired at 1kV and with magnifications ranging from 441X to 16.77kX.

Image Processing

Image processing was performed using Fiji and ImageJ [128] as well as in-house developed Matlab scripts. Initially images were imported to the workstation through Fiji's Bioformat plug-in, converted into separate 16-bit tiff images and stored back as individual tiff images for each channel and z level. These separate files were then imported into Matlab for further processing. Images were normalized, cleaned up applying median and gaussian filters and contrast was equalized when needed through Contrast Limited Adaptive Histogram Equalization (CLAHE), for visualization purposes only[129].

For the quantification of nanobeads spatial density maps, segmentation on twodimensional images was performed by statistical separation of the region of interest from the background through a Gaussian Mixture Model [130] aimed at fitting two distinct distributions of pixel intensities. Once the background region was identified and ruled out, specific positions of individual nanobeads were computed using local maxima and weighted centroid approaches. Further refinement of the (x,y) position was achieved by using a radial symmetry based particle localization approach with subpixelar capabilities [131].

Atomic Force Microscopy quantification of mechanical properties of hydrogels

Hydrogels of different stiffness were prepared by mixing 40% Acrylamide (Millipore-Sigma,Burlington, MA), 2% Bis-Acrylamide (MilliporeSigma,Burlington, MA), 20mM stock solutions of Lithium phenyl-2,4,6-trimethylbenzoylphosphinate (LAP, Sigma-Aldrich, St. Louis, MO) and water in the appropriate concentration. Three different concentrations were tested based on the stiffnesses reported previously[126] using Ammonium Persulfate (APS, Sigma-Aldrich, St. Louis, MO) and Tetramethylethylenediamine (TEMED, Thermo Fisher Scientific, Waltham, MA) as initiators and accelerator of the polymerization reaction. Flat gels were prepared by filling a

cylindrical cavity formed by two previously treated coverslips (20x20 mm2, Sigma Aldrich) and a circular stainless steel washer. This setup allowed us to have flat gels with an approximate thickness of 5mm hence preventing possible interference of the bottom substrate when performing nanoindentations. All samples were polymerized by exposing them to UV (302nm) with a benchtop transilluminator (UVP, Analytik Jena US LLC, Upland CA) for 10 minute. After this step, hydrogels were soaked in deionized water and kept at 4°C to prevent evaporation. All the measurements were carried out during the following couple of days to prevent aging of the hydrogels.

The elasticity of polyacrylamyde hydrogels was measured using a Scanning Probe Microscope (Veeco Instruments Inc. Plainview, NY) with a Nanoscope IV controller. Nanoindentation curves were obtained using a standard pyramidal tip cantilever (k=0.24N/m, DNP-10, Bruker Nano Surfaces, Goleta, CA). Due to the rather large error on the nominal spring constant value provided by the manufacturer of the probe, the Sader method was employed to try and narrow this value[132]. This method relies on the measurement of the resonant frequency, a quality factor of the cantilever, its dimensions and the properties of the fluid used.

In order to reduce the effect of adhesion forces and prevent evaporation, all experiments were conducted using a fluid cell, where the tip and the sample were covered by deionized water at room temperature. A topographical image of 5x5 μm^2 was captured for each gel and a minimum of 15 nanoindentations were performed. Curves were obtained by specifying the total movement of the piezo stage (750nm) and a maximum deflection threshold relative to the baseline of 35nm. Forward and reverse velocities were fixed at 50nm/s and the scan rate was set to 0.1Hz. After each sample was characterized, the deflection sensitivity of the cantilever was corrected by performing a nanoindentation curve on a silicon surface where no indentation was possible and consequently

piezo movement of the stage and cantilever deflection must be equal. Young's modulus for the different samples was obtained using the NanoScope Analysis software (Version 1.5, Bruker Nano Surfaces, Goleta, CA). Tip half angle was set to 20º as specified by the manufacturer. A linearized Sneddon[133] model and its correction for pyramidal tips [134] was used to fit our data.

3.2.4 Cell culture and staining

Cell culture

Human vascular umbilical endothelial vein cells (VECs) (purchased from Cell Application, San Diego, CA) were cultured in medium M199 supplemented with 10% (vol/vol) endothelial cell growth medium (Cell Application , San Diego, CA), 10% (vol/vol) FBS (Lonza, Basel, Switzerland), 1% sodium pyruvate, 1% L-glutamine, and 1% penicillin– streptomycin (Gibco, Waltham, MA) until they formed a confluent monolayer on top of 10cm cell culture plates (Thermo Fisher Scientific, Waltham, MA).

After culturing the cells and prior to seeding them in the desired substrate, we aspirated the supernatant medium and washed 3 times gently with PBS. We then aspirate the supernatant completely and incubate the monolayer 2mL of Trypsin-EDTA Solution 1X for 5 minutes at 37°C until the cells completely detach from the plate. We aspirated and collected the 2mL of suspended cells in Trypsin-EDTA and supplemented the solution with 3mL of medium, to neutralize peptide cleavage. After this step, we centrifuged the sample inside a 15mL conical tube at 1000 rpms for 5 min to generate a pellet of cells. The supernatant was then aspirated and the cells were resuspended in 5 mL of fresh medium. After this step, the cells were ready to be seeded on the substrate. We used a hemocytometer to count cells and seed for confluency (~1E-7 cells/cm^2) on top of the collagen or fibronectin coated substrates.

Staining cytoplasm of adherent cells with fluorescent dye

Before proceeding to stain the cells, a working dye solution of the dye was prepared by dissolving the lyophilized product (CellTracker™, Thermo Fisher Scientific, Waltham, MA) in high-quality Dimethyl Sulfoxide (DMSO, Sigma-Aldrich, St. Louis, MO) to a final concentration of 1 mM (1000X) solution. Next, we diluted the stock solution to a final working concentration of 10 μM in serum-free medium. The working solution was then warmed up to 37 °C.

Once the working solution was sufficiently warmed up, we removed the medium from the culture and gently added the pre-warmed CellTracker™ working solution. We then incubated the plate for 30 minutes inside the incubator. After that, we removed the working solution from the culture, washed very gently with PBS and gently added 10mL of warm medium to the tissue culture plate. The sample was then ready for imaging.

3.3 Results

3.3.1 Generation of gel precursor microdroplets

Emulsification offers an effective approach for the high-throughput generation of gel precursor microdroplets. Traditional emulsification techniques have exploited spatially dependent extensional and shear flows to rupture droplets[25,121,135]. These flows can be created easily using standard equipment in a typical wet laboratory (e.g., a vortex mixer). However, this approach typically results in polydisperse emulsions with wide distributions of droplet sizes[25]. In this study, we used microfluidics to produce monodisperse droplet suspensions containing acrylamide precursor. We designed a microfluidic device that can be fabricated using simple and standard photolithography methods (Figure 3.1).

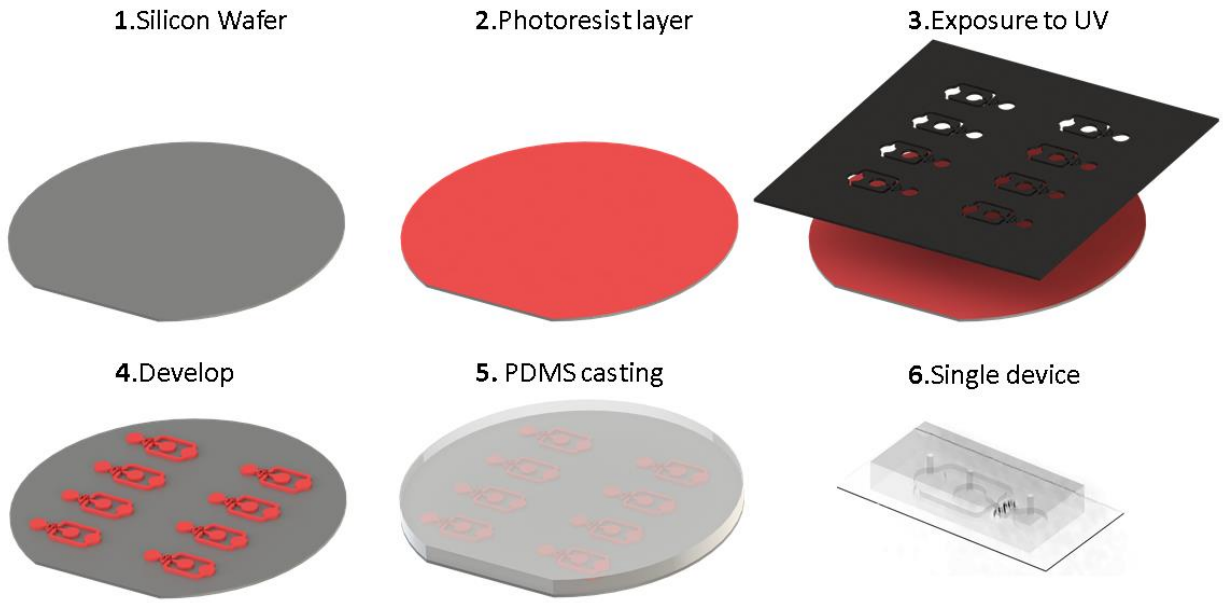

Figure 3.1: Fabrication steps of a PDMS microfluidic device for high-throughput production of monodisperse gel precursor microspheres. The device was fabricated using standard photolithography techniques. First, a silicon wafer was coated with photoresist, then a mask-less aligner was used to expose certain regions to UV light. Afterwards, the wafer was developed and the non-exposed photoresist was washed away. Finally, PDMS was used to cast the molt and single devices were cut and bonded to coverslips.

The microfluidic circuit (Figure 3.2 A) has a first stage where flow focusing emulsification[120,121,136] produces initial droplets and directs them to a collecting channel (Figure 3.2 A, first inset). The microdroplet suspension flows through the collecting channel toward a series of consecutive T junctions (Figure 3.2 A, second inset, and Figure 3.2 B) that provoke geometrically mediated droplet breakup28, considerably reducing droplet size. The final droplet size can be easily tuned by adjusting the geometry of the junction, the number of T junctions, and the ratio between the flow rates of the oil and aqueous solutions. Of note, the latter can be tuned while continuously operating the device. A high-frame-rate camera was used to

visually inspect the process of droplet breakup and collection. The resulting microdroplets suspended in oil were collected downstream and polymerized using UV light as described below (see Materials and methods). Afterwards, centrifugation was used to isolate the polymerized hydrogel microspheres from the oil phase.

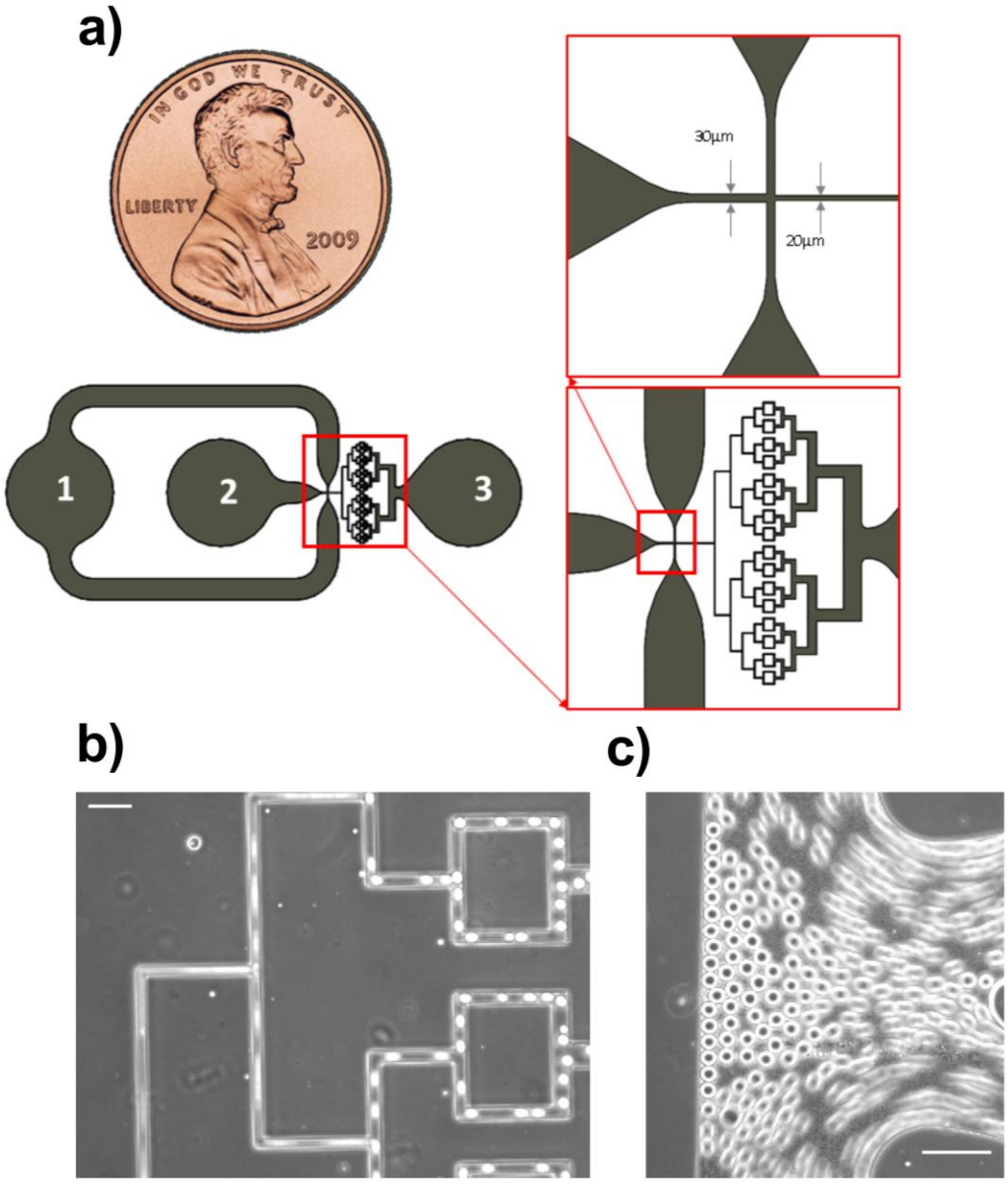

Figure 3.2: Microfluidic device for high-throughput production of monodisperse gel precursor microspheres via emulsification of water-oil solutions. a) Schematic of the microfluidic device depicting: 1) Oil phase inlet; 2) Aqueous phase inlet; 3) Outlet of the device from where pre-gel microdroplets are collected for further processing. The first (top right) inset shows the flow focusing stage where the water and oil phases merge and emulsification occurs. The second (bottom right) inset shows a detailed view of the consecutive T-shaped junctions for geometric droplet breakup.

3.3.2 Size distribution of generated microdroplets inside the flow focusing microfluidic device

We characterized the size distribution of the gel precursor microdroplets generated in a microfluidic device with 30-μm-wide channels for the oil and precursor solutions, a 20-μm-wide collecting channel and flowrates of 60/30 (oil/precursor) μL/h. Droplet size was assessed using their diameter observed using a bright field microscope (Figure 3.3A). The diameter of the microdroplets produced by the same device was varied in the range 18.6 ± 0.9 – 34.7 ± 1.3 (in mm, mean ± std) by decreasing the oil flowrate from 120 μl/h to 40 μl/h while maintaining the precursor phase flowrate constant at 30 μl/h (Figure 3.3 B). We also generated microdroplets of the same gel precursor aqueous solution in oil using a recently developed process based on inverse emulsification via vortex mixing, which is rapid and uses standard equipment (Figure 3.3 C)[25]. Vortexing at different rotation speeds allowed for some control over microdroplet size but produced significantly wider diameter distributions (Figure 3.3 D, see also Table 1). For instance, both operating the microfluidic device at 40 μl/h oil and 30 μl/h precursor and vortexing at 3,200 r.p.m. yielded microspheres with a mean diameter of approximately 35 μm; however, the diameter's standard deviation in the microfluidic device was an order of magnitude lower when compared to vortexing (3.7% of the mean vs. 36%, respectively).

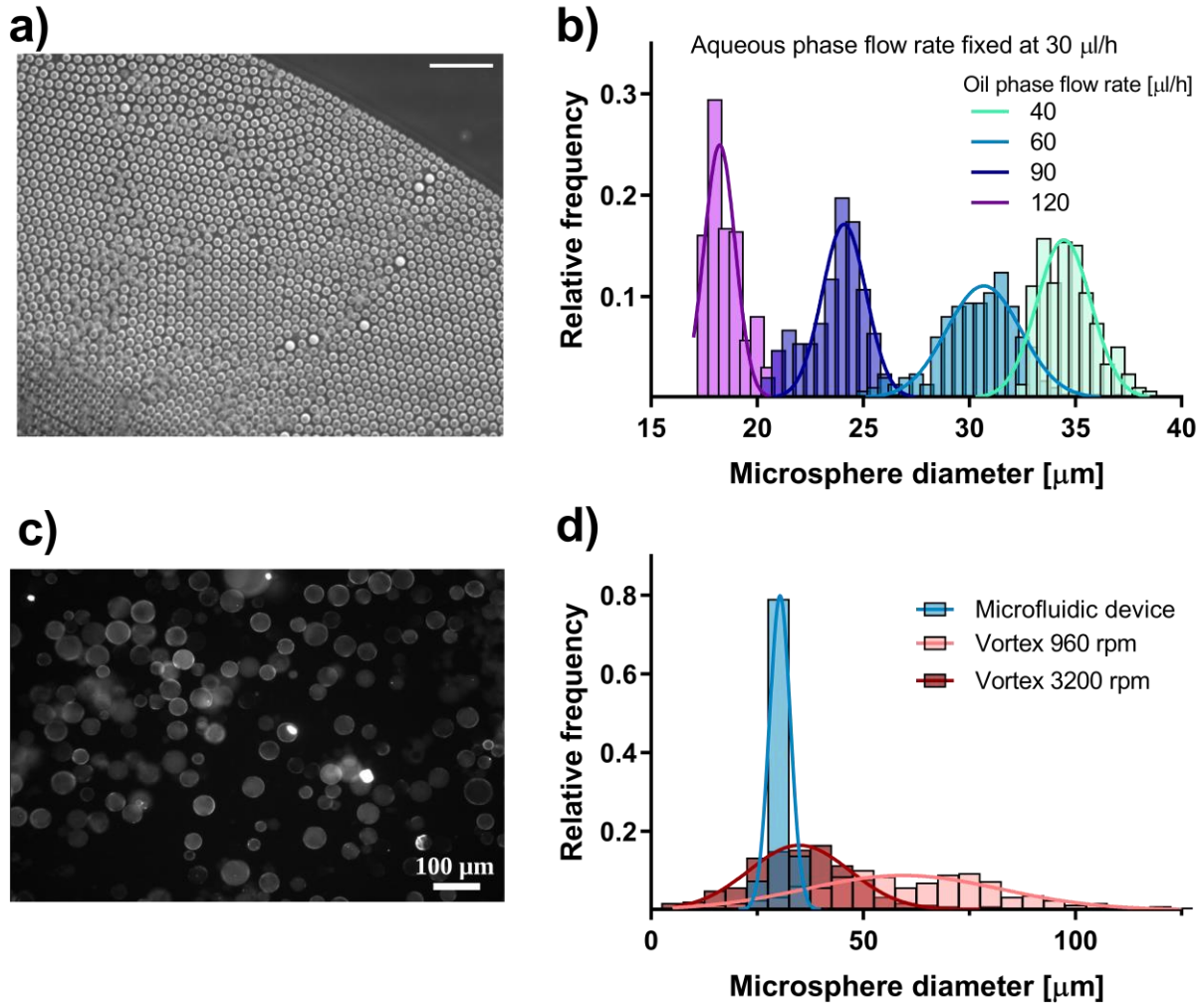

Figure 3.3: Size distribution of pre-gel droplets produced with a flow focusing microfluidic device. a) Bright field image of droplets produced by the flow-focusing microfluidic device coupled with T junctions shown in Figure 1. Scale bar: 100μm. b) Size (diameter, in microns) distributions of the liquid droplets produced for different oil flow rates and fixed water flow rate. Probability density functions were calculated for at least 100 microspheres in 3 different experiments. c) Microspheres produced by agitating the precursor and oil phases in a vortex mixer for 30 seconds. d) The microfluidic device (blue) produced microspheres with significant lower size variability than the vortex mixer (red).

Table 3.1: Summarized microdroplet sizes distributions obtained using the microfluidic device and the two-phase mixing technique using the vortex.

Droplet diameter	Flow focusing emulsification, Microfluidic Device (precursor flow rate fixed at 30μl/h)				Inverse emulsification, Vortex mixing	
	Oil flow rate (μl/h)				rotation (rpm)	
	40	60	90	120	960	3200
Mean	34.7	30.5	23.7	18.6	60.5	35.4
STD	1.3	1.9	1.3	0.9	22.8	12.9
Skewness	0.60	-0.26	-0.53	0.93	0.34	0.37
Kurtosis	-0.14	0.62	-0.48	-0.01	0.30	0.73

3.3.3 Photoinitiated polymerization of precursor acrylamide solution droplets

Once the microdroplets were produced inside the microfluidic device, the presence of surfactant stabilized the emulsion for a significant period, thus preventing droplet coalescence and allowing for droplet polymerization. To control the polymerization, we included the highly efficient, biocompatible, water-soluble photoinitiator lithium phenyl-2,4,6-trimethylbenzoylphosphinate (LAP) in the precursor acrylamide solution. The LAP compound released free radicals when exposed to UV light (302nm) in a benchtop transilluminator, triggering the polymerization reaction inside the droplets. Our rationale for using LAP over other commonly used initiators like ammonium persulfate (APS) or tetramethylethylenediamine (TEMED)[137] was hydrogel polymerization starts immediately after these initiators are mixed with the pre-gel solution, making it harder to control the process.

We added carboxylated nanobeads were to the precursor solution, which served as microsphere deformation tracers for 3D traction force microscopy[69,107]. We took advantage of these nanobeads to verify the efficacy of the photoinitiated polymerization process. When pre-gel

solution droplets did not polymerize, the fluorescent nanobeads experienced appreciable, uncoordinated Brownian motion (Figure 3.4 A). In contrast, the fluorescent tracers had fixed locations in successfully polymerized microspheres, indicative of a solidified polymeric structure with the nanobeads attached to the polymer backbone (Figure 3.4 B).

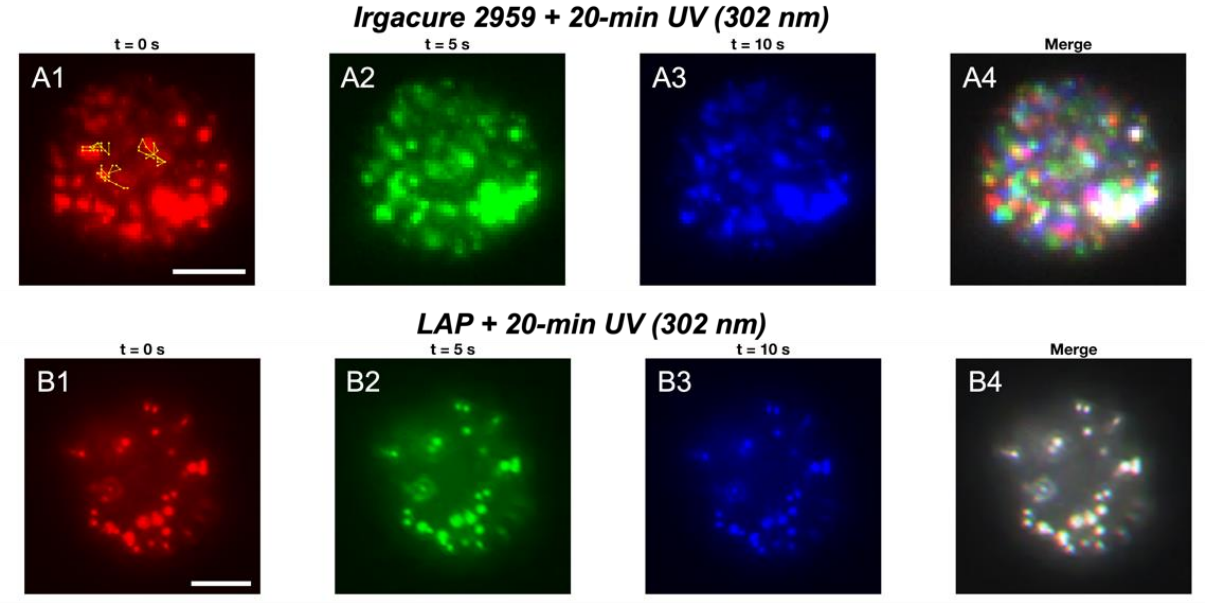

Figure 3.4**:** Photoinitiated polymerization of precursor acrylamide solution droplets containing LAP or Irgacure. A1-A3) Three snapshots of a microsphere photo-polymerized with Irgacure 2959 after a 20-min exposure to UV light (302nm), taken at 5-second intervals. The Brownian trajectories of three representative nanobeads tracked over 10 seconds are shown in panel A1. A4) Overlaying panels A1-A3 confirm that nanobeads inside the microsphere undergo Brownian motion due to incomplete polymerization. B1-B4) Three snapshots of a microsphere photo-polymerized with LAP after a 20-min exposure to UV light (302nm), taken at 5-second intervals. B4) Overlaying panels B1-B3 indicate complete microsphere polymerization and fixed nanobead positions. Scale bar: 10 microns.

Using this approach, we determined that LAP significantly overperformed one of the most widely used photoinitiators, *i.e.,* 1-[4-(2-hydroxyethoxy)-phenyl]-2-hydroxy-2-methyl-1-propanone, commonly known as Irgacure 2959. While we were able to polymerize microdroplets using concentrations of LAP as low as 0.2 mM, it was practically impossible to polymerize microspheres via UV initiation using Irgacure 2959. In the Discussion section, we argue that this issue is caused by a combination of factors causing this initiator to migrate from the aqueous pre-

gel phase to the oil phase due before it produces enough free radicals to significantly accelerate the polymerization reaction.

3.3.4 Mechanical characterization of LAP-photoinitiated polyacrylamide gels

The mechanical properties of PAAm gels polymerized using the traditional Ammonium Persulfate (APS) initiator have been described thoroughly[126]. However, the properties of LAP-photoinitiated PAAm gels are less well characterized. Given that the PAAm gel microspheres produced in our flow focusing microfluidic device were photo-initiated using LAP, we used atomic force microscopy (AFM) to measure the Young's Modulus of reference, planar, 12 mm-diameter, 20 μm-thick gel pads (see diagram in Figure 3.5 A) obtained with different ratios of acrylamide, bis-acrylamide and LAP. For reference, we also measured the Young's modulus of similar gels photo-initiated with APS. We used three acrylamide/bis-acrylamide ratios know to produce gels of low ($E \approx 3\ kPa$), intermediate ($E \approx 9\ kPa$), and high ($E \approx 40\ kPa$) stiffness (see Materials and Methods Section for details).

For gels with low or intermediate stiffness, we obtained statistically indistinguishable values of the Young's modulus using 2mM LAP or APS as initiators (Figure 3.5 B). On the other hand, for stiffer gels, there was a small albeit statistically significant difference, with LAP producing stiffer gels than APS (53.4 ± 7.8 vs. 38.3 ± 4.8, p-value <0.001, t-test with Welch correction). In the intermediate stiffness case, which corresponds with a Young's modulus value customarily used in traction force microscopy[20], we also evaluated the effect of LAP concentration on gel stiffness keeping constant the ratio of acrylamide to bis-acrylamide

concentrations (Figure 3.5 C). Our measurements showed that varying the LAP concentration between 0.2mM and 2 mM had no statistically significant effect on the stiffness of LAP-initiated gels, which also agreed with the reference, APS-initiated gel stiffness. Nonetheless, when LAP concentration was increased to 10 mM, the Young's modulus increased when compared with the nominal value. While this increase was moderate, it was statistically significant (10.2 ± 0.7 vs. 8.7 ± 1.1, p-value <0.001, t-test with Welch correction). Overall, these data suggest that there is a wide range of concentrations for which using LAP as photoinitiator does not significantly affect the well-documented mechanical properties of polymerized acrylamide/bis-acrylamide mixtures[126].

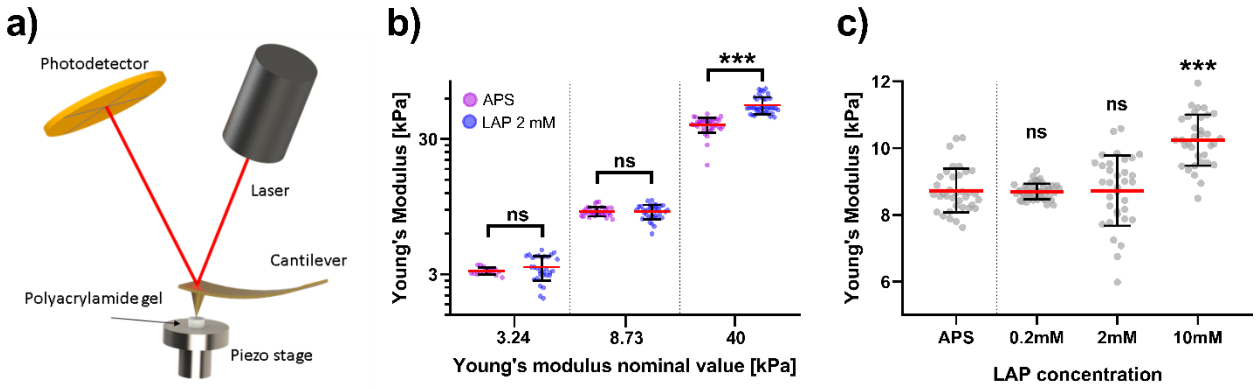

Figure 3.5: Polyacrylamide gel elasticity characterization by AFM indentation. a) A schematic of the AFM method used to measure the elasticity of the hydrogels. b) Comparison of LAP photo-initiator with a chosen concentration of 2mM with traditional APS 0.1% (w/v) formulation for three different stiffness values. Only for gel stiffness values as high as 40kPa significant differences were observed between the use of APS and LAP. b) Effect of increased concentrations of photoinitiator in the pre-gel solution. Only significant differences were observed when concentration values were increased up to 10 mM. Statistically significant differences were calculated for at least 20 gels in each condition and determined using an unpaired t test with Welch's correction (***, p< 0.001).

3.3.5 Spatial distribution of fluorescent nanobeads inside PAAm Hydrogels

Fluorescent carboxylated nanobeads of ~ 200 nm in diameter were embedded inside the PAAm microspheres through the precursor solution. Given that these nanobeads serve as fiduciary markers of microsphere deformations, achieving a homogeneous spatial distribution of nanobeads inside the final polymerized microspheres is crucial to ensure high-quality deformation measurements. To characterize this spatial distribution, we imaged the fluorescent nanobeads in our PAAm microspheres, and compared their spatial distribution with that obtained in larger (12 mm-diameter, 20 μm-thick) planer PAAm gel pads fabricated for traction force microscopy using well established methods [20,69,113]. Specifically, we took confocal image z-stacks and measured the density of nanobeads per unit area within each imaged x-y slice (e.g., Figure 3.6 A) vs. the position of the slice within the gel.

Our measurements showed that the concentration of nanobeads was almost uniform, averaging between 0.32 ± 0.12 μm^{-2} at the bottom of the spheres and 0.23 ± 0.09 μm^{-2} at their top (Figure 3.6 B). This nanobead density compares well with the density we found in large planar gel pads (Figure 3.6 C), which was fairly constant near 0.3 beads/μm^2, except near the bottom layer in contact with the coverslip and, especially, the top free surface. The increase in bead density at the top free surface increased dramatically to ≈ 1 μm^{-2}, a phenomenon that has been observed previously and is often sought after when performing traction force microscopy on flat surfaces. This concentration of nanobeads at the gel's free surface was also present in the microspheres and is observed, *e.g.*, by the sharp brightness increase at the microsphere's edge in Fig. 5A. However, it was not reflected in the density plot if Fig. 5B because, in contrast to flat substrates, no single

plane slice of the confocal z-stack captured the whole round surface of the microspheres.

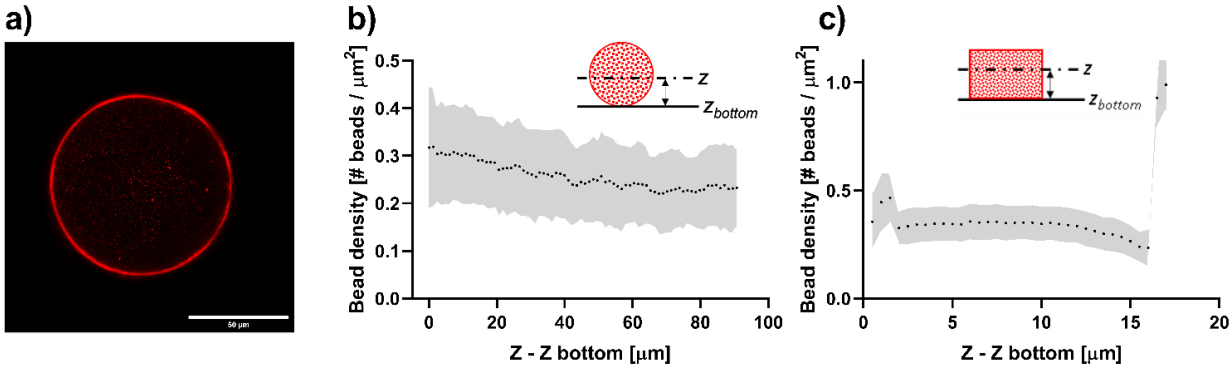

Figure 3.6: Comparison of fluorescent microbeads distribution between traditional employed 2D planar PA gels and spherical PAAm microbeads generated with our flow focusing device. In **a)** an image of the equatorial plane of a PAAm is shown. **b)** Density distribution of nanobeads density for the Z-planes imaged in the PAAm. **b)** Bead density distribution of nanobeads density for the entire 2D PA gel.

3.3.6 Microbeads surface functionalization and protein conjugation

Polyacrylamide resists the adsorption of proteins and adhesion of cells. Thus, in order to use PAAm microspheres for studying cellular interactions, it was necessary to treat the polymerized microspheres to make them capable of binding proteins. To this end, it was sufficient to follow standard procedures previously described for planar gel pads[126] (see Methods Section). Figure 3.7 a) and b) show the same microsphere with fluorescent nanotracers and functionalized with Intercellular Adhesion Molecule 1 (ICAM-1). Figure 3.7 c) shows a 3D reconstruction using confocal airyscan images from one of microsphere of the same batch as in Figure 3.7 a) and b) co-cultured with human umbilical chord vascular endothelial cells (HUVECs). The HUVECs were fluorescently stained with FITC phalloidin to label their F-actin. It can be

observed that endothelial cells are able to interact and partially engulf the microsphere. Moreover, PAAms were also functionalized with fibronectin and interacted with HUVECs (Figure 3.7 d and e). Both experiments show a homogeneous distribution of protein coating and confluent cell adhesion to the microsphere surface, demonstrating the efficacy of the protein conjugation protocol.

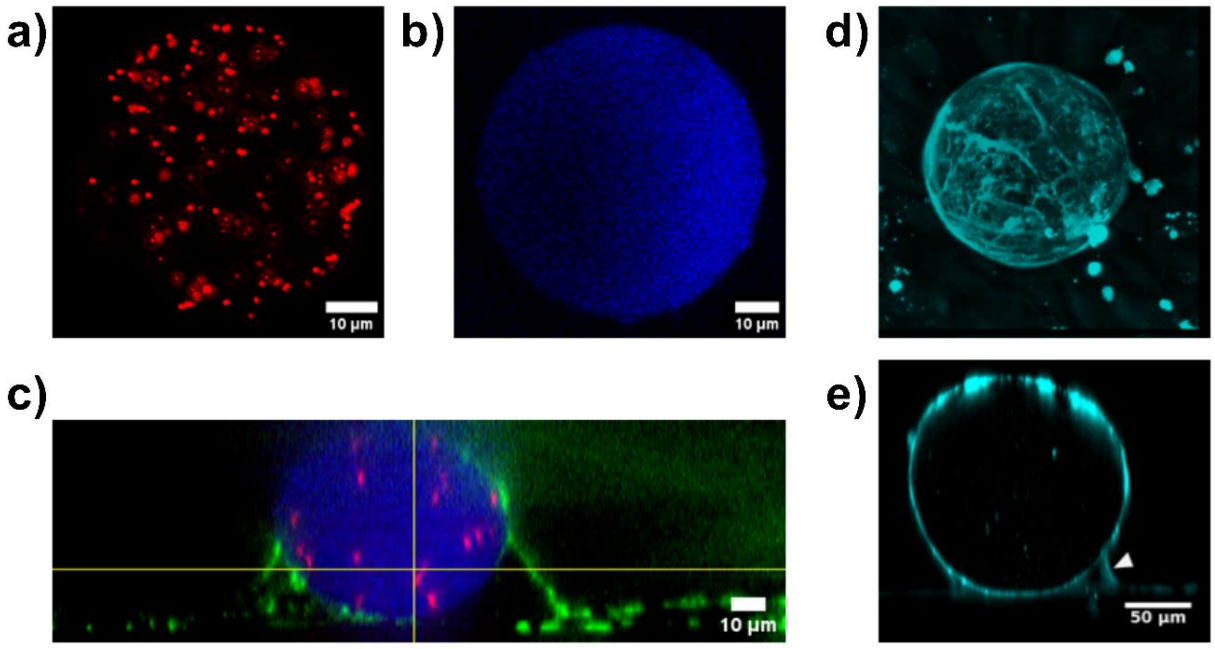

Figure 3.7: Surface activation and functionalization of polyacrylamide microbeads for cellular interaction. In **a)** the fluorescent nanotracer distribution in an image of the equatorial plane of a PAAm is shown. PAAms were later functionalized with ICAM-1, as shown in **b)**. Finally, these microbeads were interacted with HUVEC cells to ensure that the protein coating was correct. In **c)** the same PAAm as in a) and b) can be seen interacting with HUVEC, F-actin was fluorescently stained with FITC phalloidin (green). PAAm were also functionalized with fibronectin, interacted with HUVEC cells and stained with FITC phalloidin (cyan) (**d** and **e**).

.

3.3.7 Quantification of encapsulation mechanical forces exerted by vascular endothelial cells

One of the myriad of potential applications of our newly developed three-dimensional microbeads force quantification platform is the quantification of mechanical forces exerted by vascular endothelial cells during leukocyte transmigration[138]. In order to investigate this process, we performed in the past 3DTFM experiments of leukocytes on top of HUVEC cells attached to a flexible 2D PAAm substrate seeded with fluorescent nanobeads[139] and computed the intracellular tension inside the endothelial monolayer. From these experiments, we concluded that the exerted in-plane traction stresses under the endothelial cell monolayer increased significantly at the invasion site showing a vector pattern that was directed inward toward the junction and locally compressed the endothelium. We could not however quantify the actual three dimensional stresses that the leukocytes experiment and that could trigger the mechanically-induced secretion of cytokines. In order to investigate the process of vascular internalization of flexible inert particles, we generated flexible PAAm microbeads coated with 50 µg/mL of ICAM-1, a protein present in leukocytes extracellular membrane, and co-cultured them with vascular endothelial cells overnight. After 24 h, it was evident, from confocal microscopy images, that the vascular cells partially embedded the microbeads (Figure 3.8 a). Further SEM imaging of the sample (Figure 3.8 b) revealed actin rich filaments coming radially from the endothelial substrate and towards the center of the microsphere that were compatible with downward mechanical pushing forces. We then performed a experiments were the microsphere were returned to a relaxed state by treating the endothelial cells with 2mM of Cytochalassin D, a compound that inhibits actin polymerization. We compared the relaxed and compressed state and by using particle tracking we were able to characterize deformations exerted by endothelial cells (Figure 3.9).

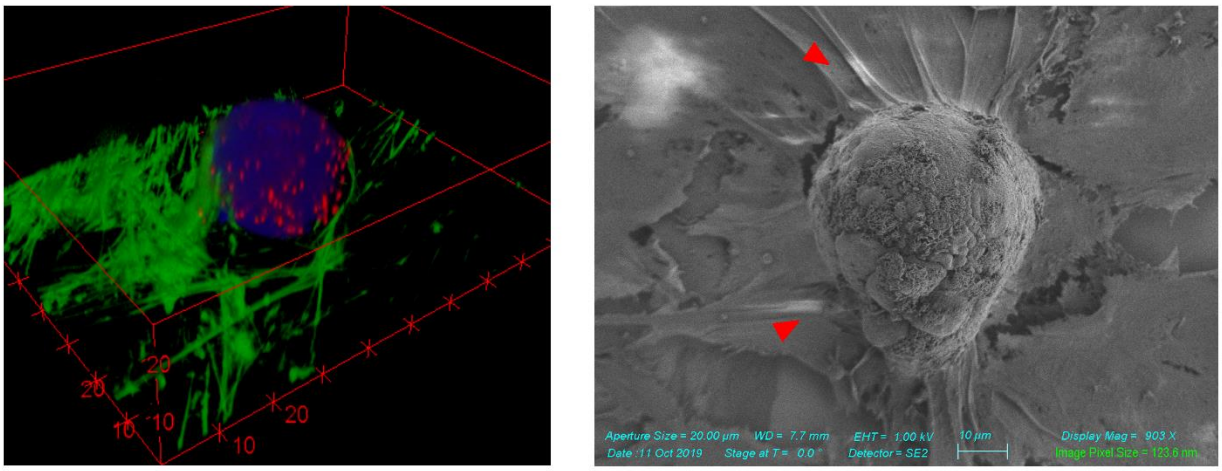

Figure 3.8: Three-dimensional view of a photoactivated polymerized PAAm microsphere functionalized with ICAM-1 and partially engulfed by vascular endothelial cells (HUVEC). In a) a 3D image reconstruction is shown. HUVEC F-actin is shown in green, microsphere ICAM-1 coating in blue and microbeads embedded in the microsphere in red, scale bar units correspond to µm. b) SEM image of a partially engulfed PAAm bead showing a perspective of the HUVEC's filopodia-like structures (red arrow) engulfing the bead, mechanically compatible with a vertical downwards pushing traction force distribution

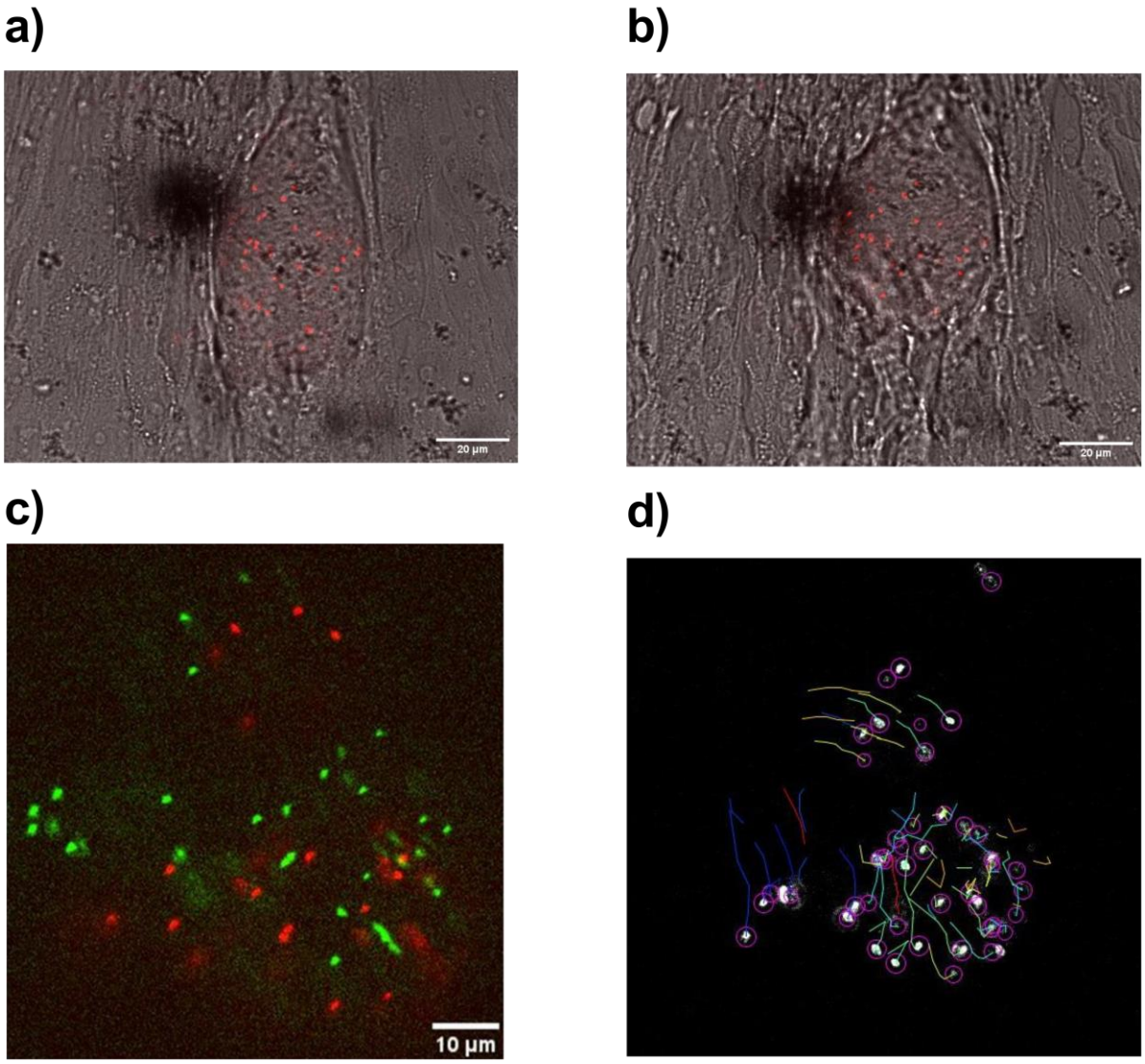

Figure 3.9: Measurement of deformations exerted by HUVECs on microbeads. ICAM-1 functionalized microbeads were co-cultured with HUVECs for 24h. Afterwards, microspheres were imaged and treated with Cytochalasin D, a potent actin polymerization inhibitor. In a) an of the equatorial plane of a microsphere before the CytoD treatment showing a compressed state. The relaxed state is shown in b) after the treatment with Cyto D. In c) the before (red) and after (green) position of the fluorescent nanotracers embedded in the microspheres. The deformations were quantified using particle tracking (d).

3.4 Discussion

Quantifying compressive stresses in living tissues has proven itself a rather hard task so far[17]. Up to this date, very few methods have achieved somehow reliable ways to quantify cell-generated mechanical forces in three dimensional assay[26,116,123,124,137,140-142]. Despite the wide range of existing techniques to explore cellular and tissue mechanics *in vitro* and in vivo, the quantitative mechanical characterization remains elusive in some physiological scenarios, especially the ones that comprise multiple time and length scales.

Some methods have used functionalized oil droplets capable of quantifying anisotropic normal stresses caused by the surrounding tissue[140]. However, they are mostly based in incompressible fluids and hence incapable of quantifying compressible forces or shear, due to the liquid nature of the force probe. Some other approaches have been more focused on the use of hydrogels to develop three dimensional elastic probes capable of quantifying anisotropic and isotropic compressive (or tensile) forces as well as shear stresses. Biocompatible alginate-based hydrogels have been proposed as linearly elastic force probes to be used for compressive stress quantification[123]. However, the process of fabricating and functionalizing the alginate beads is tedious and involves several reagents, purification steps and a careful pH control to ensure gel homogeneity and the presence of enough integrin-binding for cell adhesion available in the microbeads. Nonetheless, the major drawback these type of hydrogels poses is their limited range of linearity, making them suitable for only a few applications.

Some other authors have developed polyacrylamide-based spheres of micrometric dimensions typically generated from emulsifications of a water-oil mixture and have then typically used them to quantify three dimensional isotropic and anisotropic compressive forces[25,26,124,137,141,142]. A recent study[124] has developed highly uniform, deformable

and tunable hydrogel particles based on acrylamide-bisacrylamide solutions emulsified through a SPG emulsification technique. However, the need for specialized and expensive equipment to produce the microspheres (a microporous glass membrane), and the dependence on superresolution imaging techniques to reconstruct the three-dimensional shape of the spheres (required for force quantification), makes this method not available to laboratories without specialized resources. An easier but quite effective approach has also been recently introduced as a way to produce polyacrylamide microbeads by inverse emulsification of pre-gel solutions immersed in oil reservoirs[25,141,142], however, the introduction of high levels of mechanical energy during emulsification results in a widely disperse distribution of microbeads sizes that is not easily controllable.

Here we presented a relatively simple platform to produce elastic microbeads. We opted for Polyacrylamide (PAAm) based spherical hydrogels produced in an in-house developed flow focusing microfluidic device to produce monodisperse force probes that can be easily functionalized with ECM proteins and introduced into developing three-dimensional tissues. PAAm hydrogels were selected for their biocompatibility, non-degradability in culture conditions, compressibility and ease of surface functionalization, but most importantly, due to the fact that PAAm stiffness can be tuned over a large range by adjusting monomer and crosslinker concentrations[126]. Using our set up, we were able to produce droplets of sizes ranging from 20 to 100 μm (Fig. 2) and with a polidispersity index of ~6%. Our device is a successful combination of the flow-focusing strategy to generate the initial droplets and several downstream passive-breakup T junctions that further reduce the size of the liquid droplets initially generated in the device[143].

The polymerization of the PAAm gel inside the droplets is customarily triggered by introducing an initiator that accelerate the formation of free radicals in the precursor solution [118]. Initiators APS or TEMED, commonly used to fabricate PAAm for traction force microscopy [126], have been successfully employed to polymerize microspheres [125]. However, these initiators often generate inhomogeneous structural and mechanical properties at the micrometric scale [144] because generate free radicals immediately after mixing them with the precursor solution, causing microsphere variability within each production batch [25,137].

Photo-activatable initiators like Irgacure 2959 or LAP 3.14, which only generate free radicals when illuminated with wavelengths $\lesssim$ 400 nm [145], allow for better control of PAAm polymerization. Irgacure 2959 is one of the most widely used photo-initiators, but it has a moderate water solubility, reported to be < 2 wt% [146], and a weak light absorption and free radical production for wavelengths in the near-UV range [145]. In addition, it has a relatively high partition coefficient between aqueous and oil solvents [147], *i.e.*, $log\, P_{octanol/water} = log\big([IG2959]^{un-ionized}_{octanol}/[IG2959]^{un-ionized}_{water}\big) = 0.84$, and a relatively low molecular weight (224.3 g/mol) [148], implying that it migrates from the aqueous phase towards the fluorinated oil phase relatively fast. Despite its slow photo-initiator action and fast migration from the aqueous phase, we previously used Irgacure 2959 to control the polymerization of planar, thick ($\gtrsim$ 40 µm) PAAm substrates for cell culture and traction force microscopy [149]. However, these limitations become more critical when trying to polymerize emulsified water-based microdroplets, which have a significantly higher surface-to-volume ratio, resulting in practically impossible PAAm microsphere polymerization via Irgacure 2959 UV initiation.

Compared to Irgacure 2959, LAP's higher water solubility and near-UV range absorption and free radical cleavage makes LAP and order of magnitude faster in photopolymerizing

hydrogels [145]. In our experiments, LAP significantly overperformed Irgacure 2959 in droplet polymerization. Although we could not find reported values for LAP's partition coefficient in the literature, polymerization of PAAm microspheres was achieved with concentrations of LAP as low as 0.2mM.

We used AFM indentation to measure the mechanical properties in planar PAAm hydrogels photopolymerized with the recently introduced LAP photoinitiator with different concentrations of the initiator (Figure 3.5). The results showed a smooth linearly elastic behavior of the PAAm. Only the mechanical properties of very stiff gels or, gels with a high LAP concentration, differed from the ones polymerized with APS.

Finally, we were also able to efficiently and rapidly functionalized our microbeads with conjugated ECM proteins (FITC-FN, ICAM-1), that allowed for visualization of the homogenous coating in all spheres as well as permitting cell attachment and engulfment of the elastic microbeads by human endothelial cells.

Overall, our results demonstrate that our photopolymerized hydrogel microbeads are a powerful tool for the cross-comparison of results obtained from different cell mechanical characterization techniques, and for the validation of future novel techniques. This technology opens new perspectives for the analysis of stresses exerted not only at the cellular scale, but also inside organoids or developing tissues, where the non-perturbing characterization of mechanical stresses is pretty much nonexistent to date.

3.5 Acknowledgments

Chapter 3, in part is currently being prepared for publication. Garcia-Herreros, A., Yeh, Y.T., del Alamo, JC., Criado-Hidalgo, E. Tunable photoinitiated hydrogel microspheres for cellular force quantification in complex three-dimensional environments. The dissertation author was the primary investigator and author of this material.

Chapter 4. Concluding remarks

A brief summary of the main conclusions achieved in this dissertation is presented in this chapter; a more detailed discussion can be found at the end of each chapter.

Cardiovascular diseases (CVDs) have become the most urgent diseases globally and are responsible for an estimated 18 million deaths each year, according to the World Health Organization (WHO) [150,151]. CVDs are a group englobing multiple cardiovascular system disorders, including stroke, hypercholesterolemia, diabetes, coronary heart disease, chronic kidney disease, peripheral arterial disease. Most of these diseases target one of the three components that conform the cardiovascular system: the heart, blood and vasculature. Each of these components contain multiple functional elements. The heart is composed by cardiomyocytes, a fibrous skeleton and an electrical conductance pathway formed by highly specialized cells. On the other hand, blood contains erythrocytes, immune cells, platelets and plasma, where multiple important proteins are dissolved. Finally, the vasculature plays a key role in the control and transport of active biomolecules that can regulates inflammation, blood pressure and immune cell trafficking[152].

Dysfunction of some of these elements, it leads to cardiovascular system disorders. Due to its severe global morbidity and mortality, investigations of CVDs have attracted scientific interest, and many achievements have been obtained in the recent years [153]. Research on CVDs can be divided into three major aspects: the study of pathogenetic mechanisms, the development of accurate diagnostic methods and the creation of therapeutic treatments. Among these three aspects, pathogenesis studies of CVDs play a center role, since they can provide physiological information and can also be used as the research basis for diagnosis and treatments. Therefore, to treat CVDs, it requires initially a comprehensive investigation of the pathophysiology that can be later

translated into the two remaining aspects.

It is in this first pillar where microfluidics become of significant relevance. The use of microfluidics has recently been recognized as having inherent characteristics particularly well suited for modeling the cardiovascular system and can therefore be used as a versatile primary strategy in achieving CVD research. With cell-based microfluidic devices, artificial 3D tissue-like cardiovascular architectures can be obtained, where the conditions in the vasculature and heart can be mimicked to study the complex interactions between organs [154]. Microfabrication techniques allow for the creation of microfluidic devices with versatile geometric designs that can simulate the complex structural architectures of microvascular networks. Furthermore, they can offer precise control over flow conditions of small amounts of fluids in microchannels, comparable to the physiology of the hemodynamics of cardiovascular blood flow.

In the second chapter, we designed and fabricated a microfluidic device to model the passage of RBCs through inter-endothelial slits in the spleen. Red blood cells (RBCs) are remarkably deformable and can flow through vessels narrower than their own size. Their deformability is most dramatically challenged when they cross through micrometer-wide slits in the spleen. In several inherited or acquired RBC disorders, blockade of capillaries by stiff RBCs can trigger organ damage, but a functional spleen is expected to clear these abnormal RBCs from the circulation before they induce such complications. The spleen is in not only in charge of removing the defective or damaged RBCs but also the old ones, that have been in the circulation for an average of 120 days. By using our microfluidic device, we analyzed the flow behavior of RBCs when crossing micro-constrictions and worked on the hypothesis that mechanical fatigue triggers an accelerated senescence in RBCs.

We first studied the transition of RBCs through sub-micron constrictions to model the

passage through inter-endothelial slits in vivo. Using high frame rate videos, two motions were clearly distinguished. In the most common one, as cells approached the constriction they folded through the middle axis. Similar RBCs behaviors have been seen before in capillaries [65]. In the second motion, that although faster is less common, RBCs reoriented in the direction of less constrain. These results could be potentially useful to verify and improve a wide range of numerical models of RBCs deformation in small constrictions [36,50].

To investigate the effect of successive deformation on RBCs aging, we recirculated the RBCs through the device micro-constrictions multiple times. It became rapidly apparent that as the number of passages increase, there was a decrease in cell deformability. This was accompanied by an increase in oxidation that resulted in a higher methemoglobin content, a non-functional form of Hb, as well as a decrease in intracellular ATP. Overall, these resulted pointed towards a decrease in the stability and efficiency of RBCs as the number of constriction crossings increased.

These changes were also accompanied by morphological transformations, as RBCs lose volume and became more spheric. These changes were observed to be caused by the release of membrane-rich vesicles. As hypothesized by previous numerical simulations, the release of vesicles could be caused due to the pitching of the RBCs trailing edge during the transition through constrictions [36]. Finally, a vesiculation model was proposed and verified using high resolution STED microscopy. This model showed that the density of the membrane-cytoskeleton anchoring points increased as RBCs vesiculate, making it harder and harder for the membrane to separate from the cortex.

However, the passage through multiple constrictions not only affected the physiology of RBCs, but also promoted changes at the protein level. The release of vesicles and the increase in oxidation caused a concentration decrease in multiple RBCs proteins. By doing a proteomics study

and gene clustering analysis, these protein changes were found to be mostly related to gas transport, prevention of oxidation and structural functions. RBC aging and vesiculation have been linked to cellular oxidation, which has been long known to impair RBC deformability[100,101]. From our data we concluded that, mechanical loading and RBC antioxidant defenses are related by a positive amplification loop. When not neutralized by the RBC antioxidant system, these ROS alter the RBC bilayer-cytoskeleton complex to increase cell stiffness that at the same time it promotes vesiculation and the loss of a significant amount of antioxidant enzymes (e.g., catalase, peroxiredoxin-1, and peroxiredoxin-2).

Finally, a functional assay was performed to verify that RBCs that had crossed a large number of constrictions were easily recognized and phagocytized by macrophages. Multiple “eat me” and “don’t eat me” signals that have been proposed before were explored [45,47,87,102]. However, the increase in the phagocytosis of mechanically aged RBCs was caused by an increase in erythrocyte stiffness coupled by a higher recognition of autoimmune antibodies. Target stiffness has been shown before to induce, in macrophages, a higher phagocytosis activity[85]. On the other hand, although it is still unclear which protein is being opsonized, the recognition of large transmembrane proteins by autoimmune antibodies have been proposed as a possible pathway to explain RBCs senescence[43,155,156]. Most of these studies rely on the recognition of Band3 by autologous antibodies associating it with conformational changes caused by oxidation. Although from our results this could be also linked to an increase in the density of Band3 at the membrane.

As a second approach to study CVDs, a new technology to analyze mechanical forces exerted by cells is presented in chapter 3. Cardiovascular cells are constantly exposed to a variety of mechanical stimuli ranging from compression to strain and flow shear stresses. These cells can sense subtle changes in biophysical characteristics of the surrounding matrix, such as the stiffness,

and translate it into intracellular activation cascades often related with pro-inflammatory/pro-fibrotic phenotypes. The exposure of cells to mechanically altered conditions may have similar consequences to those of metabolic dysfunctions or chronic inflammation, resulting in the appearance of CVDs. Some of the cardiovascular processes where mechanical forces are involved include leukocytes undergoing endothelial transmigration [20], myofibroblast activation [157] and cardiac fibrosis [158]. However, there has been a lack of suitable methods to measure accurately forces in three-dimensional, developing living tissues with high spatial and temporal resolution.

Thus, in chapter 3 we developed a novel methodology to fully characterize and properly quantify three dimensional stresses in living tissues, in an easy and reproducible manner and with a wide range of applications. Spherical elastic hydrogels with tunable mechanical properties were generated using a flow focusing microfluidic device. We introduced the design of a simple, but effective, microfluidic device that allowed us to generated high throughput pre-gel droplets in oil. By effortless modifying the flowrate ratio between the pre-gel and the oil phases we tuned the diameter of the droplets produced.

We then collected and polymerized the still liquid pre-gel solution beads by means of the incorporation of a photoinitator in the initial pre-gel solution. The use of the photoinitiator Lithium phenyl-2,4,6-trimethylbenzoylphosphinate (LAP), helped us to overcome all the problems previously encountered with other standard photoinitiator, such as Irgacure 2959. The improved water solubility and partition coefficient of LAP permitted adequate solution in the water-based pre-gel solution and, more importantly, retention in the dispersed phase (water) during emulsification. Furthermore, LAP has a great advantage over other UV-photoinitiators as it can also start polymerization when exposed to larger wavelengths. Thus, LAP allows for in situ polymerization in *in vivo* experiments.

Finally, we showed that the polyacrylamide microspheres can be coated with different surface proteins for a myriad of applications. Moreover, by the introduction of fluorescent nanotracers inside the pre-gel solution, cellular deformations can be captured and 3D mechanical forces can be recomputed.

With the increasingly growing interest in exploring the roles of tissue mechanics in physiology and pathology, significant advances are arising aimed at developing new technologies that can serve as force probes to quantify 3D tissue mechanical properties. Particular interest is being dedicated to increasing the throughput and accuracy of the 3D mapping of tissue mechanics and to developing new biocompatible materials that can efficiently integrate with the surrounding tissue or even play active roles in tissue repair or engineering. We believe our developed platform along with our previously reported 3D TFM methodologies will constitute an important contribution to the field of three-dimensional quantification of tissue mechanics and will contribute to expand the current knowledge of cellular mechanotranduction in physiologically relevant settings.

Bibliography

1 Shao Y, Saredy J, Yang WY, Sun Y, et al. 2020. Vascular Endothelial Cells and Innate Immunity. *Arterioscler Thromb Vasc Biol* 40: e138-e52.

2 Krüger-Genge A, Blocki A, Franke RP, Jung F. 2019. Vascular Endothelial Cell Biology: An Update. *Int J Mol Sci* 20.

3 Basatemur GL, Jørgensen HF, Clarke MCH, Bennett MR, et al. 2019. Vascular smooth muscle cells in atherosclerosis. *Nat Rev Cardiol* 16: 727-44.

4 Pittman RN. 2011. Regulation of Tissue Oxygenation.

5 Turgeon ML. 2004. Clinical hematology : theory and procedures Philadelphia.

6 Diez-Silva M, Dao M, Han J, Lim CT, et al. 2010. Shape and Biomechanical Characteristics of Human Red Blood Cells in Health and Disease. *MRS Bull* 35: 382-8.

7 Gregory TR. 2001. The bigger the C-value, the larger the cell: genome size and red blood cell size in vertebrates. *Blood Cells Mol Dis* 27: 830-43.

8 Moras M, Lefevre SD, Ostuni MA. 2017. From Erythroblasts to Mature Red Blood Cells: Organelle Clearance in Mammals. *Front Physiol* 8: 1076.

9 Klei TR, Meinderts SM, van den Berg TK, van Bruggen R. 2017. From the Cradle to the Grave: The Role of Macrophages in Erythropoiesis and Erythrophagocytosis. *Front Immunol* 8: 73.

10 Shelby JP, White J, Ganesan K, Rathod PK, et al. 2003. A microfluidic model for single-cell capillary obstruction by Plasmodium falciparum-infected erythrocytes. *Proc Natl Acad Sci U S A* 100: 14618-22.

11 Wu T, Feng JJ. 2013. Simulation of malaria-infected red blood cells in microfluidic channels: Passage and blockage. *Biomicrofluidics* 7: 44115.

12 Du E, Diez-Silva M, Kato GJ, Dao M, et al. 2015. Kinetics of sickle cell biorheology and implications for painful vasoocclusive crisis. *Proc Natl Acad Sci U S A* 112: 1422-7.

13 Alapan Y, Fraiwan A, Kucukal E, Hasan MN, et al. 2016. Emerging point-of-care technologies for sickle cell disease screening and monitoring. *Expert Rev Med Devices* 13: 1073-93.

14 Mannino RG, Qiu Y, Lam WA. 2018. Endothelial cell culture in microfluidic devices for investigating microvascular processes. *Biomicrofluidics* 12: 042203.

15 Schwartz AB, Campos OA, Criado-Hidalgo E, Chien S, et al. 2021. Elucidating the Biomechanics of Leukocyte Transendothelial Migration by Quantitative Imaging. *Front Cell Dev Biol* 9: 635263.

16 Han S, Yan JJ, Shin Y, Jeon JJ, et al. 2012. A versatile assay for monitoring in vivo-like transendothelial migration of neutrophils. *Lab Chip* 12: 3861-5.

17 Au SH, Edd J, Stoddard AE, Wong KHK, et al. 2017. Microfluidic Isolation of Circulating Tumor Cell Clusters by Size and Asymmetry. *Sci Rep* 7: 2433.

18 Adams AA, Okagbare PI, Feng J, Hupert ML, et al. 2008. Highly efficient circulating tumor cell isolation from whole blood and label-free enumeration using polymer-based microfluidics with an integrated conductivity sensor. *J Am Chem Soc* 130: 8633-41.

19 Martino F, Perestrelo AR, Vinarský V, Pagliari S, et al. 2018. Cellular Mechanotransduction: From Tension to Function. *Front Physiol* 9: 824.

20 Yeh YT, Serrano R, François J, Chiu JJ, et al. 2018. Three-dimensional forces exerted by leukocytes and vascular endothelial cells dynamically facilitate diapedesis. *Proc Natl Acad Sci U S A* 115: 133-8.

21 Schoen I, Hu W, Klotzsch E, Vogel V. 2010. Probing cellular traction forces by micropillar arrays: contribution of substrate warping to pillar deflection. *Nano Lett* 10: 1823-30.

22 Yang MT, Fu J, Wang YK, Desai RA, et al. 2011. Assaying stem cell mechanobiology on microfabricated elastomeric substrates with geometrically modulated rigidity. *Nat Protoc* 6: 187-213.

23 Steinwachs J, Metzner C, Skodzek K, Lang N, et al. 2016. Three-dimensional force microscopy of cells in biopolymer networks. *Nat Methods* 13: 171-6.

24 Esposito E, Cortesi R, Nastruzzi C. 1996. Gelatin microspheres: influence of preparation parameters and thermal treatment on chemico-physical and biopharmaceutical properties. *Biomaterials* 17: 2009-20.

25 Labriola NR, Mathiowitz E, Darling EM. 2016. Fabricating polyacrylamide microbeads by inverse emulsification to mimic the size and elasticity of living cells. *Biomater Sci* 5: 41-5.

26 Träber N, Uhlmann K, Girardo S, Kesavan G, et al. 2019. Polyacrylamide Bead Sensors for in vivo Quantification of Cell-Scale Stress in Zebrafish Development. *Sci Rep* 9: 17031.

27 Popel AS, Johnson PC. 2005. Microcirculation and Hemorheology. *Annu Rev Fluid Mech* 37: 43-69.

28 Mebius RE, Kraal G. 2005. Structure and function of the spleen. *Nat Rev Immunol* 5: 606-16.

29 Deplaine G, Safeukui I, Jeddi F, Lacoste F, et al. 2011. The sensing of poorly deformable red blood cells by the human spleen can be mimicked in vitro. *Blood* 117: e88-95.

30 Hosseini SM, Feng JJ. 2012. How malaria parasites reduce the deformability of infected red blood cells. *Biophys J* 103: 1-10.

31 Huisjes R, Bogdanova A, van Solinge WW, Schiffelers RM, et al. 2018. Squeezing for Life - Properties of Red Blood Cell Deformability. *Front Physiol* 9: 656.

32 Taner T, Nagorney DM, Tefferi A, Habermann TM, et al. 2013. Splenectomy for massive splenomegaly: long-term results and risks for mortality. *Ann Surg* 258: 1034-9.

33 Weiss L. 1983. The red pulp of the spleen: structural basis of blood flow. *Clin Haematol* 12: 375-93.

34 Buffet PA, Milon G, Brousse V, Correas JM, et al. 2006. Ex vivo perfusion of human spleens maintains clearing and processing functions. *Blood* 107: 3745-52.

35 Badior KE, Casey JR. 2018. Molecular mechanism for the red blood cell senescence clock. *IUBMB Life* 70: 32-40.

36 Lu H, Peng Z. 2019. Boundary integral simulations of a red blood cell squeezing through a submicron slit under prescribed inlet and outlet pressures. *Phys Fluids* 31: 031902.

37 Park H, Lee S, Ji M, Kim K, et al. 2016. Measuring cell surface area and deformability of individual human red blood cells over blood storage using quantitative phase imaging. *Sci Rep* 6: 34257.

38 Piomelli S, Seaman C. 1993. Mechanism of red blood cell aging: relationship of cell density and cell age. *Am J Hematol* 42: 46-52.

39 Bennett-Guerrero E, Veldman TH, Doctor A, Telen MJ, et al. 2007. Evolution of adverse changes in stored RBCs. *Proc Natl Acad Sci U S A* 104: 17063-8.

40 Lutz HU, Liu SC, Palek J. 1977. Release of spectrin-free vesicles from human erythrocytes during ATP depletion. I. Characterization of spectrin-free vesicles. *J Cell Biol* 73: 548-60.

41 Wagner GM, Chiu DT, Qju JH, Heath RH, et al. 1987. Spectrin oxidation correlates with membrane vesiculation in stored RBCs. *Blood* 69: 1777-81.

42 Karon BS, Hoyer JD, Stubbs JR, Thomas DD. 2009. Changes in Band 3 oligomeric state precede cell membrane phospholipid loss during blood bank storage of red blood cells. *Transfusion* 49: 1435-42.

43 Low PS, Waugh SM, Zinke K, Drenckhahn D. 1985. The role of hemoglobin denaturation and band 3 clustering in red blood cell aging. *Science* 227: 531-3.

44 Arashiki N, Kimata N, Manno S, Mohandas N, et al. 2013. Membrane peroxidation and

methemoglobin formation are both necessary for band 3 clustering: mechanistic insights into human erythrocyte senescence. *Biochemistry* 52: 5760-9.

45 Connor J, Pak CC, Schroit AJ. 1994. Exposure of phosphatidylserine in the outer leaflet of human red blood cells. Relationship to cell density, cell age, and clearance by mononuclear cells. *J Biol Chem* 269: 2399-404.

46 Schroit AJ, Madsen JW, Tanaka Y. 1985. In vivo recognition and clearance of red blood cells containing phosphatidylserine in their plasma membranes. *J Biol Chem* 260: 5131-8.

47 Khandelwal S, van Rooijen N, Saxena RK. 2007. Reduced expression of CD47 during murine red blood cell (RBC) senescence and its role in RBC clearance from the circulation. *Transfusion* 47: 1725-32.

48 Qiang Y, Liu J, Dao M, Suresh S, et al. 2019. Mechanical fatigue of human red blood cells. *Proc Natl Acad Sci U S A* 116: 19828-34.

49 Sakuma S, Kuroda K, Tsai CH, Fukui W, et al. 2014. Red blood cell fatigue evaluation based on the close-encountering point between extensibility and recoverability. *Lab Chip* 14: 1135-41.

50 Pivkin IV, Peng Z, Karniadakis GE, Buffet PA, et al. 2016. Biomechanics of red blood cells in human spleen and consequences for physiology and disease. *Proc Natl Acad Sci U S A* 113: 7804-9.

51 English D, Andersen BR. 1974. Single-step separation of red blood cells. Granulocytes and mononuclear leukocytes on discontinuous density gradients of Ficoll-Hypaque. *J Immunol Methods* 5: 249-52.

52 D'Amici GM, Mirasole C, D'Alessandro A, Yoshida T, et al. 2012. Red blood cell storage in SAGM and AS3: a comparison through the membrane two-dimensional electrophoresis proteome. *Blood Transfus* 10 Suppl 2: s46-54.

53 Cruz-Landeira A, Bal MJ, Quintela, López-Rivadulla M. 2002. Determination of methemoglobin and total hemoglobin in toxicological studies by derivative spectrophotometry. *J Anal Toxicol* 26: 67-72.

54 Xu Z, Dou W, Wang C, Sun Y. 2019. Stiffness and ATP recovery of stored red blood cells in serum. *Microsyst Nanoeng* 5: 51.

55 Benjamini Y, Drai D, Elmer G, Kafkafi N, et al. 2001. Controlling the false discovery rate in behavior genetics research. *Behav Brain Res* 125: 279-84.

56 Zhou Y, Zhou B, Pache L, Chang M, et al. 2019. Metascape provides a biologist-oriented resource for the analysis of systems-level datasets. *Nat Commun* 10: 1523.

57 Baxter EW, Graham AE, Re NA, Carr IM, et al. 2020. Standardized protocols for differentiation of THP-1 cells to macrophages with distinct M(IFNγ+LPS), M(IL-4) and

M(IL-10) phenotypes. *J Immunol Methods* 478: 112721.

58 Roussel C, Monnier S, Dussiot M, Farcy E, et al. 2018. Fluorescence Exclusion: A Simple Method to Assess Projected Surface, Volume and Morphology of Red Blood Cells Stored in Blood Bank. *Front Med (Lausanne)* 5: 164.

59 Bottier C, Gabella C, Vianay B, Buscemi L, et al. 2011. Dynamic measurement of the height and volume of migrating cells by a novel fluorescence microscopy technique. *Lab Chip* 11: 3855-63.

60 Kariuki SN, Marin-Menendez A, Introini V, Ravenhill BJ, et al. 2020. Red blood cell tension protects against severe malaria in the Dantu blood group. *Nature* 585: 579-83.

61 Yoon YZ, Hong H, Brown A, Kim DC, et al. 2009. Flickering analysis of erythrocyte mechanical properties: dependence on oxygenation level, cell shape, and hydration level. *Biophys J* 97: 1606-15.

62 Pécréaux J, Döbereiner HG, Prost J, Joanny JF, et al. 2004. Refined contour analysis of giant unilamellar vesicles. *Eur Phys J E Soft Matter* 13: 277-90.

63 Gambhire P, Atwell S, Iss C, Bedu F, et al. 2017. High Aspect Ratio Sub-Micrometer Channels Using Wet Etching: Application to the Dynamics of Red Blood Cell Transiting through Biomimetic Splenic Slits. *Small* 13.

64 Guo Q, Duffy SP, Matthews K, Santoso AT, et al. 2014. Microfluidic analysis of red blood cell deformability. *J Biomech* 47: 1767-76.

65 Reinhart WH, Huang C, Vayo M, Norwich G, et al. 1991. Folding of red blood cells in capillaries and narrow pores. *Biorheology* 28: 537-49.

66 MacDonald IC, Ragan DM, Schmidt EE, Groom AC. 1987. Kinetics of red blood cell passage through interendothelial slits into venous sinuses in rat spleen, analyzed by in vivo microscopy. *Microvasc Res* 33: 118-34.

67 Smith AS, Nowak RB, Zhou S, Giannetto M, et al. 2018. Myosin IIA interacts with the spectrin-actin membrane skeleton to control red blood cell membrane curvature and deformability. *Proc Natl Acad Sci U S A* 115: E4377-E85.

68 Atkinson M, Sherlock S. 1954. Intrasplenic pressure as index of portal venous pressure. *Lancet* 266: 1325-7.

69 del Álamo JC, Meili R, Álvarez-González B, Alonso-Latorre B, et al. 2013. Three-dimensional quantification of cellular traction forces and mechanosensing of thin substrata by fourier traction force microscopy. *PLoS One* 8: e69850.

70 Blendis LM, Banks DC, Ramboer C, Williams R. 1970. Spleen blood flow and splanchnic haemodynamics in blood dyscrasia and other splenomegalies. *Clin Sci* 38: 73-84.

71 Weiss JN. 1997. The Hill equation revisited: uses and misuses. *FASEB J* 11: 835-41.

72 DeLean A, Munson PJ, Rodbard D. 1978. Simultaneous analysis of families of sigmoidal curves: application to bioassay, radioligand assay, and physiological dose-response curves. *Am J Physiol* 235: E97-102.

73 Luten M, Roerdinkholder-Stoelwinder B, Schaap NP, de Grip WJ, et al. 2008. Survival of red blood cells after transfusion: a comparison between red cells concentrates of different storage periods. *Transfusion* 48: 1478-85.

74 Cadart C, Zlotek-Zlotkiewicz E, Venkova L, Thouvenin O, et al. 2017. Fluorescence eXclusion Measurement of volume in live cells. *Methods Cell Biol* 139: 103-20.

75 Mohandas N, Kim YR, Tycko DH, Orlik J, et al. 1986. Accurate and independent measurement of volume and hemoglobin concentration of individual red cells by laser light scattering. *Blood* 68: 506-13.

76 Jaferzadeh K, Moon I. 2015. Quantitative investigation of red blood cell three-dimensional geometric and chemical changes in the storage lesion using digital holographic microscopy. *J Biomed Opt* 20: 111218.

77 Tomaiuolo G. 2014. Biomechanical properties of red blood cells in health and disease towards microfluidics. *Biomicrofluidics* 8: 051501.

78 Popescu G, Ikeda T, Goda K, Best-Popescu CA, et al. 2006. Optical measurement of cell membrane tension. *Phys Rev Lett* 97: 218101.

79 Betz T, Lenz M, Joanny JF, Sykes C. 2009. ATP-dependent mechanics of red blood cells. *Proc Natl Acad Sci U S A* 106: 15320-5.

80 Guo Q, Reiling SJ, Rohrbach P, Ma H. 2012. Microfluidic biomechanical assay for red blood cells parasitized by Plasmodium falciparum. *Lab Chip* 12: 1143-50.

81 Wagner GM, Chiu DT, Yee MC, Lubin BH. 1986. Red cell vesiculation--a common membrane physiologic event. *J Lab Clin Med* 108: 315-24.

82 Nowak RB, Alimohamadi, H., Pestonjamasp, K., Rangamani, P., & Fowler, V. M. 2021. Nanoscale organization of Actin Filaments in the Red Blood Cell Membrane Skeleton. *BioRxiv*

83 Gokhin DS, Nowak RB, Khoory JA, Piedra AeL, et al. 2015. Dynamic actin filaments control the mechanical behavior of the human red blood cell membrane. *Mol Biol Cell* 26: 1699-710.

84 Mohanty JG, Nagababu E, Rifkind JM. 2014. Red blood cell oxidative stress impairs oxygen delivery and induces red blood cell aging. *Front Physiol* 5: 84.

85 Beningo KA, Wang YL. 2002. Fc-receptor-mediated phagocytosis is regulated by

mechanical properties of the target. *J Cell Sci* 115: 849-56.

86 Sosale NG, Rouhiparkouhi T, Bradshaw AM, Dimova R, et al. 2015. Cell rigidity and shape override CD47's "self"-signaling in phagocytosis by hyperactivating myosin-II. *Blood* 125: 542-52.

87 Burger P, de Korte D, van den Berg TK, van Bruggen R. 2012. CD47 in Erythrocyte Ageing and Clearance - the Dutch Point of View. *Transfus Med Hemother* 39: 348-52.

88 Nagelkerke SQ, Bruggeman CW, den Haan JMM, Mul EPJ, et al. 2018. Red pulp macrophages in the human spleen are a distinct cell population with a unique expression of Fc-γ receptors. *Blood Adv* 2: 941-53.

89 Buerck JP, Burke DK, Schmidtke DW, Snyder TA, et al. 2019. A Flow Induced Autoimmune Response and Accelerated Senescence of Red Blood Cells in Cardiovascular Devices. *Sci Rep* 9: 19443.

90 Picot J, Ndour PA, Lefevre SD, El Nemer W, et al. 2015. A biomimetic microfluidic chip to study the circulation and mechanical retention of red blood cells in the spleen. *Am J Hematol* 90: 339-45.

91 Pretini V, Koenen MH, Kaestner L, Fens MHAM, et al. 2019. Red Blood Cells: Chasing Interactions. *Frontiers in Physiology* 10.

92 Bogdanova A, Lutz H. 2013. Mechanisms tagging senescent red blood cells for clearance in healthy humans. *Frontiers in Physiology* 4.

93 Lominadze D, Dean WL. 2002. Involvement of fibrinogen specific binding in erythrocyte aggregation. *FEBS Letters* 517: 41-4.

94 Rumsby MG, Trotter J, Allan D, Michell RH. 1977. Recovery of membrane micro-vesicles from human erythrocytes stored for transfusion: a mechanism for the erythrocyte discocyte-to-spherocyte shape transformation. *Biochem Soc Trans* 5: 126-8.

95 Lu H, Peng Z. 2019. Boundary integral simulations of a red blood cell squeezing through a submicron slit under prescribed inlet and outlet pressures. *Phys Fluids* 31.

96 Asaro RJ, Zhu Q, Cabrales P. 2018. Erythrocyte Aging, Protection via Vesiculation: An Analysis Methodology via Oscillatory Flow. *Front Physiol* 9: 1607.

97 Danielczok JG, Terriac E, Hertz L, Petkova-Kirova P, et al. 2017. Red Blood Cell Passage of Small Capillaries Is Associated with Transient Ca. *Front Physiol* 8: 979.

98 Tissot J-D, Canellini G, Rubin O, Angelillo-Scherrer A, et al. 2013. Blood microvesicles: From proteomics to physiology. *Transl Proteom* 1: 14.

99 Walensky L, Mohandas N, Lux SE. 2003. Disorders of the red blood cell membrane. Philadelphia, PA.

100 Sinha A, Chu TT, Dao M, Chandramohanadas R. 2015. Single-cell evaluation of red blood cell bio-mechanical and nano-structural alterations upon chemically induced oxidative stress. *Sci Rep* 5: 9768.

101 Şekeroğlu MR, Huyut Z, Him A. 2012. The susceptibility of erythrocytes to oxidation during storage of blood: effects of melatonin and propofol. *Clin Biochem* 45: 315-9.

102 Wesseling MC, Wagner-Britz L, Huppert H, Hanf B, et al. 2016. Phosphatidylserine Exposure in Human Red Blood Cells Depending on Cell Age. *Cell Physiol Biochem* 38: 1376-90.

103 Willekens FL, Werre JM, Groenen-Döpp YA, Roerdinkholder-Stoelwinder B, et al. 2008. Erythrocyte vesiculation: a self-protective mechanism? *Br J Haematol* 141: 549-56.

104 Mammoto T, Ingber DE. 2010. Mechanical control of tissue and organ development. *Development* 137: 1407-20.

105 Paszek MJ, Zahir N, Johnson KR, Lakins JN, et al. 2005. Tensional homeostasis and the malignant phenotype. *Cancer Cell* 8: 241-54.

106 Engler AJ, Sen S, Sweeney HL, Discher DE. 2006. Matrix elasticity directs stem cell lineage specification. *Cell* 126: 677-89.

107 Wang N, Tytell JD, Ingber DE. 2009. Mechanotransduction at a distance: mechanically coupling the extracellular matrix with the nucleus. *Nat Rev Mol Cell Biol* 10: 75-82.

108 Dembo M, Wang YL. 1999. Stresses at the cell-to-substrate interface during locomotion of fibroblasts. *Biophys J* 76: 2307-16.

109 Butler JP, Tolić-Nørrelykke IM, Fabry B, Fredberg JJ. 2002. Traction fields, moments, and strain energy that cells exert on their surroundings. *Am J Physiol Cell Physiol* 282: C595-605.

110 Sabass B, Gardel ML, Waterman CM, Schwarz US. 2008. High resolution traction force microscopy based on experimental and computational advances. *Biophys J* 94: 207-20.

111 Del Alamo JC, Meili R, Alonso-Latorre B, Rodríguez-Rodríguez J, et al. 2007. Spatio-temporal analysis of eukaryotic cell motility by improved force cytometry. *Proc Natl Acad Sci U S A* 104: 13343-8.

112 Tan JL, Tien J, Pirone DM, Gray DS, et al. 2003. Cells lying on a bed of microneedles: an approach to isolate mechanical force. *Proc Natl Acad Sci U S A* 100: 1484-9.

113 Serrano R, Aung A, Yeh YT, Varghese S, et al. 2019. Three-Dimensional Monolayer Stress Microscopy. *Biophys J* 117: 111-28.

114 Tambe DT, Croutelle U, Trepat X, Park CY, et al. 2013. Monolayer stress microscopy: limitations, artifacts, and accuracy of recovered intercellular stresses. *PLoS One* 8: e55172.

115 Campàs O, Mammoto T, Hasso S, Sperling RA, et al. 2014. Quantifying cell-generated mechanical forces within living embryonic tissues. *Nat Methods* 11: 183-9.

116 Serwane F, Mongera A, Rowghanian P, Kealhofer DA, et al. 2017. In vivo quantification of spatially varying mechanical properties in developing tissues. *Nat Methods* 14: 181-6.

117 Elbert DL. 2011. Liquid-liquid two-phase systems for the production of porous hydrogels and hydrogel microspheres for biomedical applications: A tutorial review. *Acta Biomater* 7: 31-56.

118 Shao C, Chi J, Shang L, Fan Q, et al. 2022. Droplet microfluidics-based biomedical microcarriers. *Acta Biomater* 138: 21-33.

119 Graf M, Ziegler CE, Gregoritza M, Goepferich AM. 2019. Hydrogel microspheres evading alveolar macrophages for sustained pulmonary protein delivery. *Int J Pharm* 566: 652-61.

120 Garstecki P, Fuerstman MJ, Stone HA, Whitesides GM. 2006. Formation of droplets and bubbles in a microfluidic T-junction-scaling and mechanism of break-up. *Lab Chip* 6: 437-46.

121 Gañán-Calvo AM. 2004. Perfectly monodisperse microbubbling by capillary flow focusing: an alternate physical description and universal scaling. *Phys Rev E Stat Nonlin Soft Matter Phys* 69: 027301.

122 Xu JH, Luo GS, Li SW, Chen GG. 2006. Shear force induced monodisperse droplet formation in a microfluidic device by controlling wetting properties. *Lab Chip* 6: 131-6.

123 Mohagheghian E, Luo J, Chen J, Chaudhary G, et al. 2018. Quantifying compressive forces between living cell layers and within tissues using elastic round microgels. *Nat Commun* 9: 1878.

124 Vorselen D, Wang Y, de Jesus MM, Shah PK, et al. 2020. Microparticle traction force microscopy reveals subcellular force exertion patterns in immune cell-target interactions. *Nat Commun* 11: 20.

125 Girardo S, Träber N, Wagner K, Cojoc G, et al. 2018. Standardized microgel beads as elastic cell mechanical probes. *J Mater Chem B* 6: 6245-61.

126 Tse JR, Engler AJ. 2010. Preparation of hydrogel substrates with tunable mechanical properties. *Curr Protoc Cell Biol* Chapter 10: Unit 10.6.

127 Álvarez-González B, Zhang S, Gómez-González M, Meili R, et al. 2017. Two-Layer Elastographic 3-D Traction Force Microscopy. *Sci Rep* 7: 39315.

128 Rueden CT, Schindelin J, Hiner MC, DeZonia BE, et al. 2017. ImageJ2: ImageJ for the next generation of scientific image data. *BMC Bioinformatics* 18: 529.

129 Reza AM. 2004. Realization of the Contrast Limited Adaptive Histogram Equalization

(CLAHE) for Real-Time Image Enhancement. *<i data-test="journal-title" style="box-sizing: inherit;">Journal of VLSI signal processing systems for signal, image and video technology* 38: 35–44.

130 Lee DS. 2005. Effective gaussian mixture learning for video background subtraction. *IEEE Trans Pattern Anal Mach Intell* 27: 827-32.

131 Parthasarathy R. 2012. Rapid, accurate particle tracking by calculation of radial symmetry centers. *Nat Methods* 9: 724-6.

132 Sader JE, Sanelli JA, Adamson BD, Monty JP, et al. 2012. Spring constant calibration of atomic force microscope cantilevers of arbitrary shape. *Rev Sci Instrum* 83: 103705.

133 Sneddon IN. 1965. The relation between load and penetration in the axisymmetric boussinesq problem for a punch of arbitrary profile. *International journal of engineering science* 3: 47–57.

134 Bilodeau GG. 1992. Regular Pyramid Punch Problem. *Journal of Applied Mechanics* 59: 519-23.

135 Martín-Banderas L, Flores-Mosquera M, Riesco-Chueca P, Rodríguez-Gil A, et al. 2005. Flow Focusing: a versatile technology to produce size-controlled and specific-morphology microparticles. *Small* 1: 688-92.

136 Anna *SL*, Bontoux N, Stone HA. 2003. Formation of dispersions using "flow focusing" in microchannels. *Applied Physics Letters* 82: 5929-31.

137 Girardo S, Traber N, Wagner K, Cojoc G, et al. 2018. Standardized microgel beads as elastic cell mechanical probes. *J Mater Chem B* 6: 6245-61.

138 Schwartz AB, Campos OA, Criado-Hidalgo E, Chien S, et al. 2021. Elucidating the Biomechanics of Leukocyte Transendothelial Migration by Quantitative Imaging. *Front Cell Dev Biol* 9: 635263.

139 Yeh YT, Serrano R, Francois J, Chiu JJ, et al. 2018. Three-dimensional forces exerted by leukocytes and vascular endothelial cells dynamically facilitate diapedesis. *Proc Natl Acad Sci U S A* 115: 133-8.

140 Campas O, Mammoto T, Hasso S, Sperling RA, et al. 2014. Quantifying cell-generated mechanical forces within living embryonic tissues. *Nat Methods* 11: 183-9.

141 Dolega ME, Delarue M, Ingremeau F, Prost J, et al. 2017. Cell-like pressure sensors reveal increase of mechanical stress towards the core of multicellular spheroids under compression. *Nat Commun* 8: 14056.

142 Lee W, Kalashnikov N, Mok S, Halaoui R, et al. 2019. Dispersible hydrogel force sensors reveal patterns of solid mechanical stress in multicellular spheroid cultures. *Nat Commun* 10: 144.

143 Link DR, Anna SL, Weitz DA, Stone HA. 2004. Geometrically mediated breakup of drops in microfluidic devices. *Phys Rev Lett* 92: 054503.

144 Nagashima S, Ando S, Makino K, Tsukamoto T, et al. 1998. Size Dependence of Polymer Composition in the Surface Layer of Poly(acrylamide-co-acrylic acid) Hydrogel Microspheres. *J Colloid Interface Sci* 197: 377-82.

145 Fairbanks BD, Schwartz MP, Bowman CN, Anseth KS. 2009. Photoinitiated polymerization of PEG-diacrylate with lithium phenyl-2,4,6-trimethylbenzoylphosphinate: polymerization rate and cytocompatibility. *Biomaterials* 30: 6702-7.

146 Fouassier J-P, Burr D, Wieder F. 1991. Water-soluble photoinitiators: Primary processes in hydroxy alkyl phenyl ketones. *Journal of Polymer Science Part A: Polymer Chemistry* 29: 1319-27.

147 Sangster JM. 1997. Octanol-Water Partition Coefficients: Fundamentals and Physical Chemistry.

148 Eren TN, Kariksiz N, Demirci G, Tuncel D, et al. 2021. Irgacure 2959-functionalized poly(ethyleneimine)s as improved photoinitiators: enhanced water solubility, migration stability and visible-light operation. *Polymer Chemistry* 12: 2772-85.

149 Del Álamo JC, Lemons D, Serrano R, Savchenko A, et al. 2016. High throughput physiological screening of iPSC-derived cardiomyocytes for drug development. *Biochim Biophys Acta* 1863: 1717-27.

150 Group WCRCW. 2019. World Health Organization cardiovascular disease risk charts: revised models to estimate risk in 21 global regions. *Lancet Glob Health* 7: e1332-e45.

151 Fuster V, Kelly BB. 2010. Promoting Cardiovascular Health in the Developing World: A Critical Challenge to Achieve Global Health.

152 Piera-Velazquez S, Jimenez SA. 2019. Endothelial to Mesenchymal Transition: Role in Physiology and in the Pathogenesis of Human Diseases. *Physiol Rev* 99: 1281-324.

153 Celermajer DS, Chow CK, Marijon E, Anstey NM, et al. 2012. Cardiovascular disease in the developing world: prevalences, patterns, and the potential of early disease detection. *J Am Coll Cardiol* 60: 1207-16.

154 Jain A, van der Meer AD, Papa AL, Barrile R, et al. 2016. Assessment of whole blood thrombosis in a microfluidic device lined by fixed human endothelium. *Biomed Microdevices* 18: 73.

155 Lutz HU, Bussolino F, Flepp R, Fasler S, et al. 1987. Naturally occurring anti-band-3 antibodies and complement together mediate phagocytosis of oxidatively stressed human erythrocytes. *Proc Natl Acad Sci U S A* 84: 7368-72.

156 Lutz HU, Bogdanova A. 2013. Mechanisms tagging senescent red blood cells for clearance

in healthy humans. *Front Physiol* 4: 387.

157 Berk BC, Fujiwara K, Lehoux S. 2007. ECM remodeling in hypertensive heart disease. *J Clin Invest* 117: 568-75.

158 de Boer RA, De Keulenaer G, Bauersachs J, Brutsaert D, et al. 2019. Towards better definition, quantification and treatment of fibrosis in heart failure. A scientific roadmap by the Committee of Translational Research of the Heart Failure Association (HFA) of the European Society of Cardiology. *Eur J Heart Fail* 21: 272-85.